THE HONG KONG
POLYTECHNIC UNIVERSITY
香港理工大學
Pao Yue-kong Library
包玉剛圖書館

Copyright Undertaking

This thesis is protected by copyright, with all rights reserved.

By reading and using the thesis, the reader understands and agrees to the following terms:

1. The reader will abide by the rules and legal ordinances governing copyright regarding the use of the thesis.
2. The reader will use the thesis for the purpose of research or private study only and not for distribution or further reproduction or any other purpose.
3. The reader agrees to indemnify and hold the University harmless from and against any loss, damage, cost, liability or expenses arising from copyright infringement or unauthorized usage.

IMPORTANT

If you have reasons to believe that any materials in this thesis are deemed not suitable to be distributed in this form, or a copyright owner having difficulty with the material being included in our database, please contact lbsys@polyu.edu.hk providing details. The Library will look into your claim and consider taking remedial action upon receipt of the written requests.

Pao Yue-kong Library, The Hong Kong Polytechnic University, Hung Hom, Kowloon, Hong Kong

http://www.lib.polyu.edu.hk

MOISTURE-RESPONSIVE BEHAVIOR OF HYGROSCOPIC MEMBRANES: FROM MECHANISTIC UNDERSTANDING TO RATIONAL REGULATION

ZIJING ZHANG

PhD

The Hong Kong Polytechnic University

2026

The Hong Kong Polytechnic University

Department of Mechanical Engineering

Moisture-responsive Behavior of Hygroscopic Membranes: From Mechanistic Understanding to Rational Regulation

Zijing Zhang

A thesis submitted in partial fulfilment of the requirements for the degree of

Doctor of Philosophy

August 2025

CERTIFICATE OF ORIGINALITY

I hereby declare that this thesis is my own work and that, to the best of my knowledge and belief, it reproduces no material previously published or written, nor material that has been accepted for the award of any other degree or diploma, except where due acknowledgement has been made in the text.

_____ (Signed)

ZIJING ZHANG (Name of Student)

Abstract

Moisture-responsive membranes have attracted increasing attention in the fields of actuators and energy harvesting due to their lightweight and high flexibility. For instance, bilayer membranes are often employed in humidity sensors because of their rapid and precise hygroscopic deformation. However, the underlying mechanical mechanisms and regulation strategies governing hygroscopic deformation remain largely unexplored, and this lack of fundamental understanding limits further development of such materials. To address these challenges, this thesis systematically investigates the mechanics of hygroscopic membrane deformation under humidity stimuli, aiming to establish a comprehensive theoretical framework and propose rational regulation strategies.

This thesis is organized into three core research chapters (Chapters 4–6), focusing on two distinct types of membrane system and their corresponding mechanical insights. In Chapter 4, the deformation of bilayer membranes under different humidity fields was systematically investigated by extending a classical thin-film mechanics model to derive analytical solutions for the curvature–humidity relationship. Bilayer systems composed of MXene/NP as the active layer and PVC as the inert layer were fabricated, and the theoretical predictions were validated through both finite element simulations and experiments. The results demonstrate that our model not only predicts the deformation configuration but also assesses the stability of free-standing membranes under arbitrary humidity fields, while clarifying their dependence on the physical

properties of each layer. These findings provide a robust mechanical foundation for predicting bilayer hygroscopic deformation and hold great potential for their applications in sensors and actuators.

In Chapter 5, monolayer stacked nanoflake assemblies (SNA) membranes were found to exhibit more complex hygroscopic responses. Unlike the static bending observed in bilayers, SNA membranes placed in humidity fields above a hot water bath exhibited autonomous oscillatory behavior. Comparative experiments revealed that this oscillation originates from the coupling between humidity gradients along the height and the reversible hygroscopic expansion of the membrane. Theoretical analysis, integrating water diffusion with beam vibration theory, uncovered the fundamental mechanics of this phenomenon. Furthermore, dimensional analysis established quantitative relations between oscillation characteristics, intrinsic material properties, and external humidity fields. These results provide valuable insights for understanding and predicting the oscillatory behavior of SNA membranes, which is crucial for their application in actuators and energy harvesting.

In Chapter 6, the practical implications of such autonomous oscillations are explored. Inspired by biological propulsion, a fluke-inspired propulsion system driven by SNA membranes was demonstrated, along with a hand-moisture-powered nanogenerator based on electromagnetic induction. These proof-of-concept demonstrations further confirm the functional importance of our findings. Additionally, systematic experiments revealed the failure mechanisms of SNA membranes under

prolonged humid operation, including oxidation in MXene/NP membranes and hygroscopic saturation in GO/SA membranes. Importantly, the theoretical framework also successfully explains the disappearance of oscillatory behavior after decay, providing guidelines for improving the durability and performance of SNA membranes.

Overall, this thesis establishes a systematic and in-depth framework for understanding and regulating the hygroscopic deformation of membranes. By bridging theoretical modeling, finite element simulations, and experimental validation, it not only develops a solid mechanical foundation for both bilayer and monolayer systems but also proposes strategies to achieve controlled, predictable, and durable deformation responses. The results provide valuable guidance for the structural design and optimization of hygroscopic membranes, with broad application prospects in soft actuators and energy harvesting devices. Ultimately, the framework developed herein is expected to accelerate the development of multifunctional hygroscopic membrane systems and their integration into next-generation smart devices.

Publications arising from the thesis

1. **Zijing Zhang**, Jimin Fu, Zhihua Liang, Boxun Zhang, Gesa Zhang, Haimin Yao. Rational Tuning of Hygroscopic Oscillation of Stacked Nanoflake Assemblies for Continuous Ambient Energy Harvesting. *PNAS.* Under revision.
2. **Zjing Zhang**, Haimin Yao, Deformative response of bilayer thin-film actuators to gradient stimuli, In preparation.
3. **Zijing Zhang**, Zhihua Liang, Haimin Yao. Thin-film actuators (TFAs): A review. *npj Robotics*. 2025;3(1):23.
4. Baoping Zhang†, Yaxuan Wang†, Jian Jiang†, **Zijing Zhang**†, Yifei Yang, Wanghuai Xu, Jingyi Lu, Yuxin Song, Mingyu Li, Weihong Li, Jimin Fu. Steven Wang, Haimin Yao, Xiaocheng Zeng, Zuankai Wang. Drinking bird-like swing motion in MXene membrane via thermal-elastocapillary effect. († Co-first authors). In progress.

Acknowledgements

As my PhD journey comes to an end, looking back over the past five years, I realize it has been a profoundly meaningful period of growth. I would like to express my sincerest gratitude to all those who have supported me during this time.

First and foremost, I wish to express my deepest thanks to my esteemed supervisor, Prof. Haimin Yao, for his invaluable guidance, support, and mentorship throughout my PhD. From him, I have not only gained insights into the vast ocean of scientific research but also learned the rigor, focus, and diligence of a researcher. More importantly, I have learned valuable life lessons from his example. Whenever I felt lost or uncertain, his guidance always pointed me in the right direction. I consider myself extremely fortunate to be his student, and this experience will remain a lifelong treasure.

I would also like to thank my collaborator, Dr. Jimin Fu, with whom I conducted research on the oscillatory behavior of SNA. His work in molecular dynamics has been an inspiring example for me to follow.

I feel very fortunate to have worked with the members of the Bio-inspired Mechanics and Structures (BiMS) group, including Dr. Andre Eccel Vellwock, Dr. Yan Yi, Dr. Xuyang Chu, Dr. Xuchao Wang, Dr. Boonho Cho, Dr. Zhenbin Guo, Mr. Zhihua Liang, Mr. Boxun Zhang, Mr. Lintao Mi, Mr. Gesa Zhang, Ms. Yujie Xie, Mr. Like Jiang, Mr. Peng Ouyang, and Ms. Yanzhuang Xuan. Thank you for your support and for the countless shared moments that have added color and joy to my doctoral life.

I would also like to thank all the administrative staff in the Department of Mechanical Engineering for their assistance, including but not limited to Ms. Lily Tam, Ms. Michelle Lai, Ms. Merlin Wong, and Ms. Yan Wong, as well as Mr. Curtis Ng. My thanks also go to the technical staff, including but not limited to Mr. Hardy Lui, Mr. Benny Leung, Mr. Terrence Wong, and Mr. Ka-on Yuen, for their invaluable help.

Last but certainly not least, I owe my deepest gratitude and respect to my parents and grandfather for their unwavering support throughout my PhD journey. You have shown me that no matter where I am, home is always the warmest harbor and the strongest support. Your selfless love and encouragement have carried me to this point; without you, I could not have completed my PhD. You are my lifelong role models, and I will always respect and cherish you.

I will forever treasure my time at The Hong Kong Polytechnic University and will always remember every person who has been part of this journey.

Table of Contents

List of figures

Chapter 1. Introduction

Hygroscopic deformation is a widespread natural phenomenon, exemplified by plants that adjust their morphology in response to humidity variations for environmental adaptation. Inspired by such behavior, numerous humidity-responsive actuators have been developed to harness water—one of the most abundant and sustainable resources in nature. Among them, hygroscopic membranes have garnered particular attention due to their lightweight structure, high flexibility, and design programmability. Despite these advantages, significant challenges remain. First, the fundamental mechanical mechanisms of hygroscopic deformation are still not fully understood. Second, the sustained cyclic response of most hygroscopic membranes typically relies on externally controlled humidity sources, reducing efficiency in the application of energy harvesting. Finally, prediction and rational control of the autonomous oscillation of monolayer SNA membrane in humidity field remain difficult. Overcoming these challenges is essential for advancing the practical deployment of hygroscopic membranes in energy harvesting and actuation technologies.

1.1 Moisture-responsive materials in nature

Due to the substantial day–night humidity variation in nature, many plants have evolved to exploit these changes for functional deformation [1, 2]. For example, pinecones scale open in dry conditions to release seeds and close in humid conditions to conserve moisture, as shown in **Figure 1.1 (a)** [3]. Similarly, wheat seeds expand

during dry daytime conditions to drill in the soil and contract at night when it is more humid, allowing them to dig deeper into the soil and absorb moisture, as shown in **Figure 1.1 (b)** [2]. In both cases, the bending deformation results from a hygroscopic mismatch between layers, which induces a strain gradient under humid conditions. This deformation disappears under dry conditions, allowing the structure to return to its original state [4].

Another example of natural hygroscopic deformation involves the generation of helical motions [5-7]. In *Pelargonium* (geranium) seeds, the fibers at the seed tips are inclined arranged. Under humid conditions, they uncoil, while in dry conditions, uneven hygroscopic expansion induces a bending deformation that evolves into a helical twist, enabling the seed to coil and drill into the soil, as shown in **Figure 1.1 (c)** [8]. An even more complex mechanism is observed in oat (*Avena*) seeds. Their two awns undergo rotation in response to humidity changes. When the awns interlock, increasing humidity is stored as elastic energy. Upon release, this energy causes the awns to entangle, allowing the seed to 'snap' and escape unsuitable soil environments, as shown in **Figure 1.1 (d)** [9].

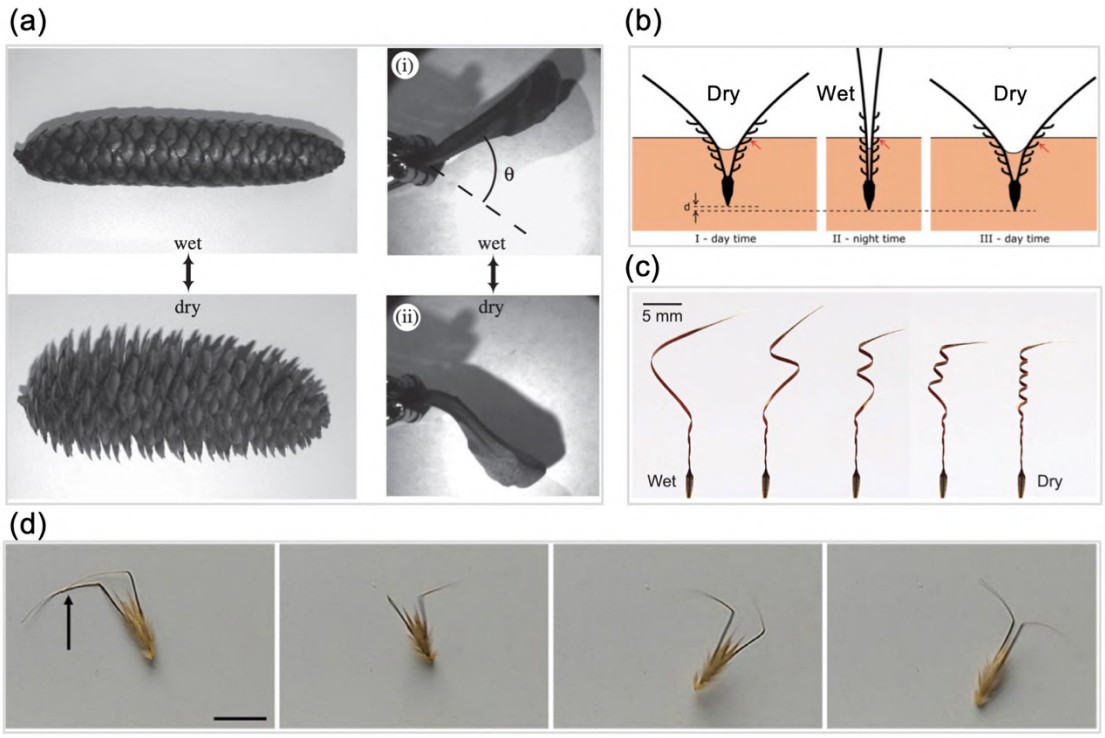

Figure 1.1 Moisture-induced deformation of plants. (a) Pine cones open in dry environment to release seeds (adapted from [3]). (b) Wheat awns open-close cycle to drill the seeds into soil (adapted from [2]). (c) Coiling-uncoiling cycle of *Pelargonium* in different humidity (adapted from). (d) Entanglement of awns and realization of jumping motion of oat (adapted from [9]).

The hygroscopic deformations observed in nature primarily originate from gradient swelling caused by differential moisture absorption in plant tissues, which is largely governed by the microstructure of plant fiber cells [10, 11]. A common structure of a plant is the bilayer configuration composed of an active and an inactive layer [12-14]. When relative humidity changes, the active layer undergoes swelling or shrinkage, inducing a bending deformation [15]. The awns of *Pelargonium* seeds represent a classic bilayer structure: their active layer contains more hemicellulose and lignin compared to the passive layer, resulting in a higher degree of hygroscopic swelling upon

water absorption, as shown in **Figures 1.2 (a-c)** [8, 14]. Similar bilayer mechanisms are also found in wheat awns and pinecones.

Interestingly, when the fiber orientation angles differ between the active and passive layers, more complex deformations such as twisting or coiling can arise [2, 4, 16]. This phenomenon is common in leguminous plants. For instance, in the seed pods of *Bauhinia* species, the outer cellulose layers exhibit a ~45° inclined arrangement. When relative humidity fluctuates, differential shrinkage occurs in opposing directions, generating helical deformation that opens the pod to release seeds, as shown in **Figures 1.2 (d-f)**.

Moreover, the awns of oat (*Avena*) seeds exhibit an advanced version of the bilayer concept by forming a radial bilayer structure along the cylindrical body [17, 18]. As relative humidity decreases, the knee region bends while the main body twists due to obliquely aligned fibers. This coordinated deformation drives the oat seeds to move forward or even jump, enhancing their ability to disperse and colonize suitable soil environments, as shown in **Figure 1.2 (g-i)**.

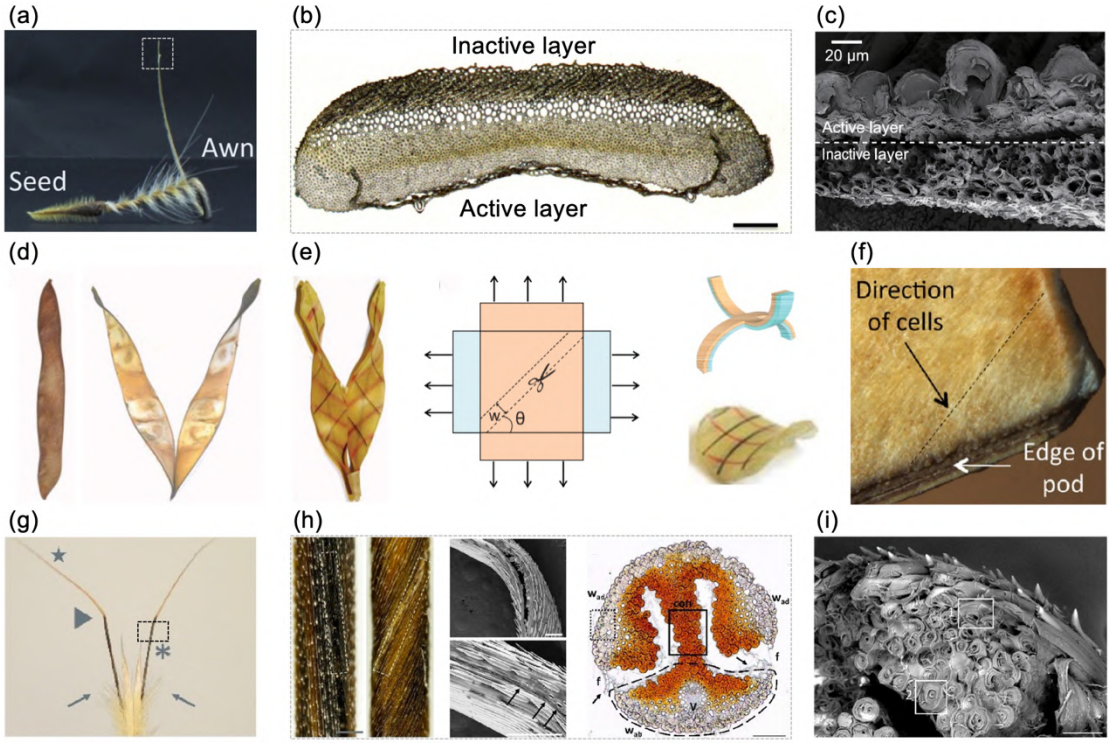

Figure 1.2 (a) The *Erodium gruinum* awn. (b) Optical image of the cross-section in the middle of the *Erodium gruinum* awn, demonstrating a bilayer structure: inactive and active layer (adapted from [14]). (c) SEM images showing the difference in microstructure of the active and inactive layer (adapted from [8]). (d) The seeds pods of *Bauhinia* species generate a hygroscopic twisting deformation to open the pods. (e) Schematic illustration of the inclined alignment of the active and inactive layers within seeds pods. (f) An optical image of the direction of fiber cells in the seeds pods (adapted from [4]). (g) An optical image shows the structure of an oat. (h) Microstructural characterization of the fiber alignment and cross-section of the oat awn. (i) SEM images showing the inclined alignment and the coiled microstructure of a single oat awn (adapted from [9]).

1.2 Moisture-responsive materials in engineering

Moisture-responsive materials rely on the hygroscopic swelling behavior to produce mechanical deformation [19]. Based on this, the responsive materials must be

hydrophilic and with high hygroscopic swelling coefficient. In addition, they should also possess high flexibility to induce large deformation, appropriate water diffusivity to enable suitable response speed, and high hygroscopic stability to prevent degradation [20-22]. Organic polymers are one of the ideal candidates for moisture-responsive materials, as there usually are abundant hydroxyl groups on their polymer chains, which endow them with good hydrophilicity [23-25]. The absorbed water molecules will change the chemical formation of the polymer chain, as well as the reconstruction of their chemical structures [26-28]. For instance, Poly (vinyl alcohol) (PVA) [29], Poly (ethylene glycol) diacrylate (PEG-DA) [30], and Sodium Alginate (SA) [31] are commonly used as moisture-responsive materials. However, for some applications such as flexible sensors and soft robotics, the moisture-responsive materials are required to exhibit high mechanical strength, good electrical conductivity, and high specific surface. In this case, 2D materials are worth studying as they exhibit excellent mechanical properties, abundant hydrophilic functional groups, and controllable water diffusivity [32-34]. Prevailing 2D materials for humidity-driven thin-film materials include MXene [35-37], CNTs [38], and graphene oxide (GO) [39-41], as shown in **Figure 1.3**. Two-dimensional materials can absorb water vapor, which leads to structural changes. Their layered structure, as well as the hydroxyl functional groups, provide abundant surface area and channels for water molecules to enter. When water is adsorbed, it changes the spacing between layers and creates internal stress, resulting in nonuniform strain that causes bending or twisting deformation. Hot pressing [42, 43], chemical

cross-linking [39, 44], and vacuum filtration [45, 46] are manufacturing methods often adopted to fabricate these actuators.

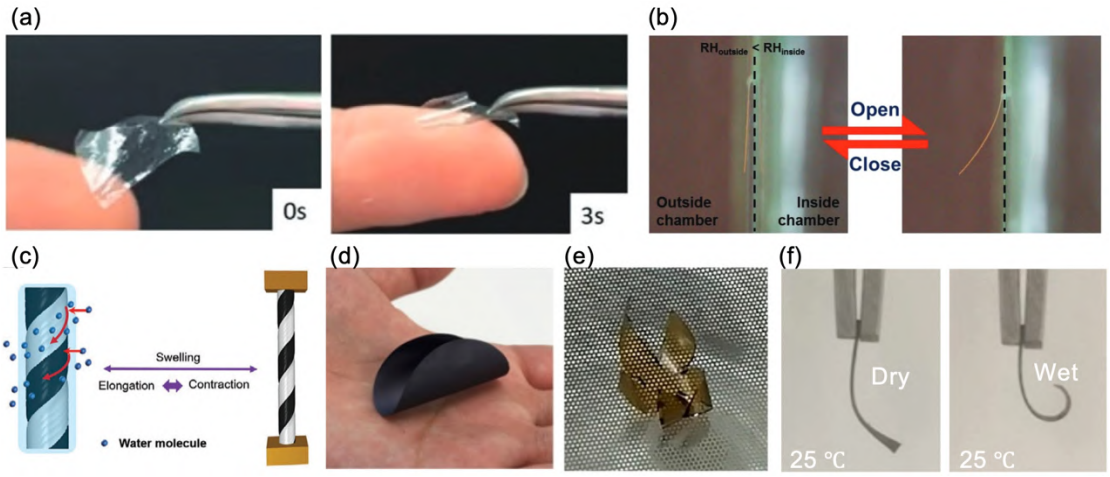

Figure 1.3 Moisture-responsive materials. (a) PVA membrane bends in response to palm humidity (adapted from [29]). (b) PEG-DA membrane bends in response to relative humidity difference (adapted from [30]). (c) Hygroscopic swelling of the SA actuator when exposed to moisture (adapted from [31]). (d) MXene membrane bends in response to palm humidity (adapted from [35]). (e) CNT/PDMS membrane bends in response to water vapor (adapted from [38]). (f) GO/SA membrane bends in response to relative humidity change (adapted from [39]).

To generate a macroscopic deformation in response to moisture, a hygroscopic strain mismatch within the membrane is required. Similar to natural plants, most moisture-responsive materials are bilayer structures consisting of an active layer and an inert layer [47-49]. Upon stimulation, the active layer experiences a pronounced volumetric change, whereas the inert layer remains comparatively unresponsive, generating mismatch strain that induces macroscopic bending of the structure, as shown in **Figure 1.4**. Generally, bilayer membranes are manufactured through depositions (PVD or CVD) [50, 51], spin-coating [52, 53], and electro-spraying [54, 55]. The

interfacial integrity between the active and inert layers is critical for ensuring the long-term durability of membranes [56]. To achieve high durability, methods such as chemical modification of the active and inert layer to make them more compatible [57, 58], roughening the surface of the inert layer to promote the mechanical interlocking are adopted [59, 60]. Beyond multilayer configurations, membranes with a monolayer structure represent a feasible alternative, in which macroscopic deformation originates from in-plane strain gradients across the thickness [39]. These gradients can be engineered via material heterogeneity [61] or imposed through thickness-dependent stimulation [62]. For monolayer structures, the mechanisms underlying hygroscopic responses are often more complex and highly sensitive to the distribution of external stimuli [63]. However, whether in single-layer or bilayer configurations, most existing designs are limited to responding to a single type of stimulus. To realize multi-responsive functions, multilayer membranes (>2 layers) have been engineered by combining layers that respond selectively to different stimuli [64-66]. While such designs enable more complex deformation behaviors and broadened functionalities, the increased number of heterogeneous interfaces also introduces drawbacks, including a higher risk of interfacial delamination and void formation. Moreover, the complex fabrication process may introduce cracks within the structure. These issues not only substantially reduce the service life of multilayer structures but also compromise the electrical conductivity and mechanical performance of the membranes, while simultaneously increasing manufacturing costs. Consequently, multilayer moisture-

responsive membranes have not been widely adopted in practical applications.

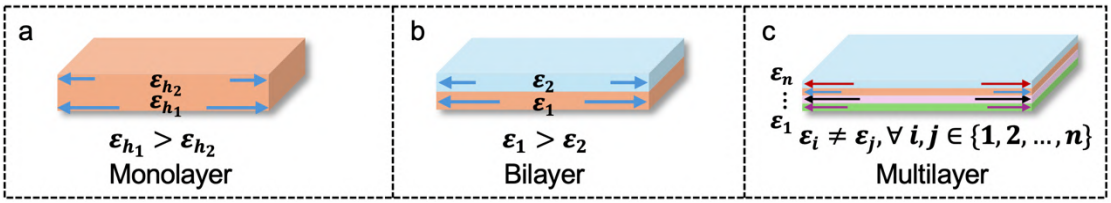

Figure 1.4 Typical structures of thin-film materials (TFMs), (a) monolayer, (b) bilayer, and (c) multilayer

Despite the extensive studies on moisture-responsive materials, two major challenges remain unresolved. First, there is a lack of systematic investigation into the underlying mechanics that govern the deformation of bilayer hygroscopic membranes under arbitrary humidity stimuli. Addressing this issue would significantly enhance the programmability of such materials and promote their application in soft robotics. Second, recent studies have shown that single-layer hygroscopic membranes can exhibit sustained oscillations under humidity gradients [62], indicating great potential for energy harvesting and soft actuation. However, the mechanics of this oscillatory behavior remain poorly understood, hindering further performance optimization. Therefore, resolving these two challenges is crucial for advancing the development of hygroscopic membranes.

1.3 Aims and objectives

This thesis aims to provide a comprehensive mechanical investigation of the deformative responses of hygroscopic membranes, focusing on two main structural types: bilayer and monolayer membranes. The first objective is to establish a

mechanical model capable of predicting the deformation configurations of bilayer membranes under moisture stimuli. The second objective is to elucidate the mechanism underlying the oscillatory behavior of monolayer membranes, with the goal of leveraging this phenomenon for applications in energy harvesting and propulsion.

The subsequent chapters of this thesis are organized as follows. Chapter 2 reviews the research background, with a focus on the current development of hygroscopic membranes. It begins by introducing the fundamental mechanics of thin-film materials, applicable to various stimuli including humidity, heat, light, and electricity. This is followed by a comprehensive review of existing structural design in hygroscopic membranes and their applications in soft actuators and related devices. Chapter 3 presents the fabrication and experimental characterization of plain MXene, MXene/NP, and GO/SA membranes. This includes mechanical testing, microstructural analysis, and diffusion coefficient measurements. The measurement of moisture distribution—serving as the environmental stimulus—is also detailed. Chapter 4 investigates the deformative responses of bilayer hygroscopic membranes under arbitrary moisture stimuli. Theoretical modeling is developed to predict the deformation of both cantilevered and free-standing membranes. Chapter 5 provides a systematic study of the moisture-driven autonomous oscillation observed in monolayer stacked nanoflakes assembly (SNA) membranes. Experimental observations are used to identify the origin of the oscillation, followed by theoretical analysis to uncover the underlying mechanics. Methods for rationally controlling the oscillatory behavior are also demonstrated. In

Chapter 6, SNA membranes are applied in energy harvesting and biomimetic propulsion. The theoretical insights from Chapter 5 serve as a foundation for application design. Additionally, the mechanical mechanisms behind performance degradation are investigated. Finally, Chapter 7 summarizes and discusses the findings of the thesis and provides an outlook on future research directions.

Chapter 2. Research background and literature review

Due to the abundance of water resources on Earth, hygroscopic membranes hold great application potential, particularly in areas such as energy harvesting, wearable electronics, soft robotics, and the Internet of Things. Therefore, a mechanical investigation of their deformation response under humidity stimuli is of critical importance for enabling precise prediction and control. Moreover, since the deformation of hygroscopic membranes is fundamentally driven by strain mismatch, the underlying thin-film mechanics are also applicable to other stimuli, such as thermal or optical inputs. In addition, this chapter will discuss the current mainstream strategies for regulating the deformation of hygroscopic membranes, along with their relevant applications.

2.1 Structural design of thin-film materials

To induce strain mismatch, hygroscopic membranes are typically designed in either bilayer or monolayer configurations. In bilayer structures, the mismatch arises from differences in the hygroscopic expansion coefficients between two distinct materials. In contrast, monolayer membranes rely on non-uniform humidity stimuli or heterogeneous structural design to generate internal strain gradients. Furthermore, to achieve programmable deformation, the structural design of hygroscopic membranes is often made more complex.

2.1.1 Monolayer thin-film materials

For uniform monolayer membranes, the most common approach to inducing a through-thickness strain gradient is to impose a non-uniform humidity stimulus—for example, exposure to the surface of evaporating water at a constant temperature [67, 68]. Due to the intrinsic humidity gradient in such environments, different regions within the membrane are subjected to varying vapor concentrations during deformation, thereby generating a strain gradient (**Figure 2.1 (a)**) [45]. Another strategy involves reducing the diffusivity of water within the monolayer membrane [69, 70]. When exposed to a humidity source, this leads to the formation of a thin, swelling layer, while the opposite side remains relatively dry. The mismatch in swelling between the hydrated and less-hydrated layers produces a strain mismatch, resulting in bending deformation (**Figure 2.1 (b)**) [71].

In the case of non-uniform monolayer membranes, variations in hygroscopic swelling properties along the thickness direction enable deformation even under uniform humidity stimuli [72-74]. One approach is to modify the surface morphology on each side of the membrane, resulting in asymmetric hygroscopic swelling strains in identical humid environments [75, 76]. For instance, increasing the surface roughness on one side enhances the specific surface area [75], allowing greater water absorption and thus inducing a larger hygroscopic strain on that side (**Figure 2.1 (c)**). Another strategy involves chemical modification—such as anodic electrical writing—to create an ion concentration gradient within the membrane [77]. When exposed to humidity, the absorbed water molecules induce directional ion migration, altering the

intermolecular spacing and generating hygroscopic expansion. The ion concentration gradient leads to an internal strain gradient, which in turn drives membrane deformation (**Figure 2.1 (d)**) [78].

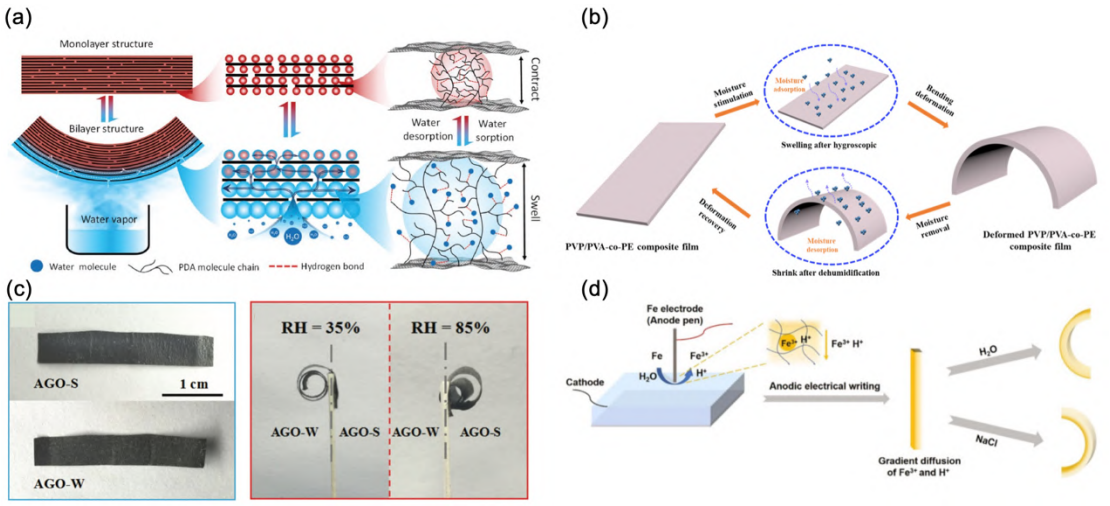

Figure 2.1 Structural design strategies of monolayer hygroscopic membranes. (a) Introduction of an uneven humidity stimulus for a uniform monolayer (adapted from [45]). (b) Uniform monolayer structure with low water diffusivity (adapted from [71]). (c) Non-uniform GO monolayer membrane with smooth side (AGO-S) and wavy side (AGO-W) producing a curling deformation under humidity stimuli (adapted from [75]). (d) Non-uniform liquid crystal monolayer membrane producing a bending deformation under humidity stimuli by directional ion transport (adapted from [78]).

2.1.2 Bilayer thin-film materials

For bilayer hygroscopic membranes, the most common fabrication strategy involves using a non-hygroscopic material (inert layer) as a substrate, onto which a hygroscopic material (active layer) is attached. One of the most straightforward methods is to directly adhere the hygroscopic material onto the substrate, which is why polymer-based adhesive tapes are often employed as inert layers [79-81]. For instance,

a hygroscopic polyvinylpyrrolidone and Poly(acrylic acid) (PVP/PAA) layer can be directly adhered to a PI tape to form a hygroscopic membrane (**Figure 2.2 (a)**) [82]; a hygroscopic MXene-coated paper (MCP) can be adhered to a PE tape to form a bilayer structure (**Figure 2.2 (b)**) [83]. Another approach relies on van der Waals forces to bind the hygroscopic and non-hygroscopic layers together [84-86]. For instance, the hygroscopic reduced graphene oxide (rGO) layer can be directly deposited on the polydimethylsiloxane (PDMS) layer through simple spin coating, and the thin rGO layer was bonded to the PDMS substrate through van der Waals forces (**Figure 2.2 (c)**) [87]. Similarly, a conductive ink (CNTs-GO) made by polyhydric polyurethane (PU), carbon nanotubes (CNTs), and graphene oxide (GO) was directly deposited on the polyethylene terephthalate (PET), and it was able to bend upon thermal and humidity stimulus (**Figure 2.2 (d)**) [84]. However, both methods suffer from a significant drawback: the interface between the two dissimilar layers is mechanically fragile, resulting in poor structural stability and limited lifespan of the bilayer membrane. To address these limitations, a bilayer structure with homogeneous materials is adopted.

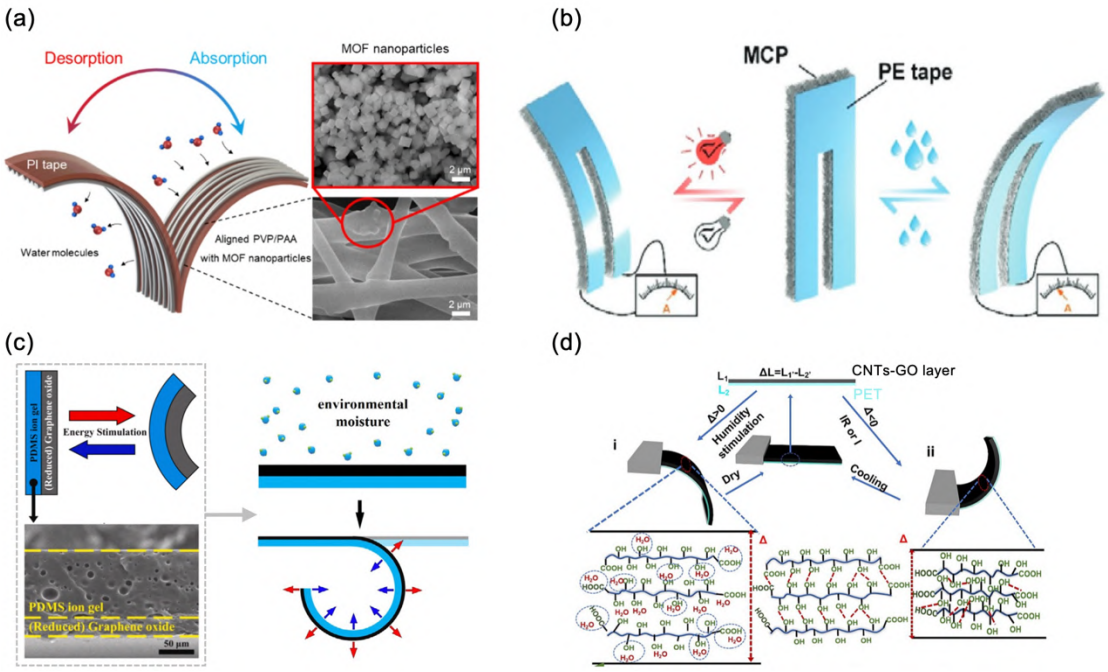

Figure 2.2 Typical bilayer structure of hygroscopic membranes, composed of two heterogeneous materials. (a) Direct adhesion of the hygroscopic PVP/PAA layer to the PI tape. (b) Direct adhesion of the hygroscopic MCP layer to the PE tape. (c) The binding of the hygroscopic rGO layer to the PDMS layer through van der Waals forces. (d) The binding of the hygroscopic CNTs-GO layer to the PET layer through van der Waals forces.

To improve interfacial stability, two chemically similar materials can be bonded via chemical interactions, forming a more robust interface [88]. This approach involves chemical modification of the same type of materials to endow different hygroscopic properties, enabling them to function as active and inert layers, respectively. For example, mixing PEO (polyethylene oxide) with MOF (metal–organic framework) increases its hygroscopic expansion coefficient. When this composite (MP) is used as the active layer in a bilayer membrane with another hygroscopic PEO layer (HP), the interfacial strength is significantly enhanced, along with a pronounced hygroscopic

deformation response (**Figure 2.3 (a)**) [79]. Similarly, graphene oxide (GO) and reduced graphene oxide (rGO) share comparable chemical compositions but exhibit distinct hygroscopic expansion behaviors. A bilayer membrane composed of GO and rGO demonstrates both high interfacial strength and excellent hygroscopic responsiveness (**Figure 2.3 (b)**) [89]. Another strategy is to introduce an interfacial reinforcement material to enhance adhesion. For instance, incorporating cellulose between MXene and polycarbonate (PC) layers can effectively strengthen the interface (**Figure 2.3 (c)**) [90]. Moreover, enhancing interfacial strength involves increasing the surface roughness of the inert layer to enlarge the contact area with the active layer. For example, uncoated natural latex sheets (*cis*-1,4-polyisoprene) exhibit inherently rough surfaces, which enable strong bio-adhesion with hygroscopic bacterial layers (*Escherichia coli* cells) (**Figure 2.3 (d)**). The increased surface area promotes greater interfacial bonding strength. In this system, the hygroscopic bacterial layer generates shrinkage stress upon dehydration, driving the bending deformation of the bilayer hygroscopic membrane [91].

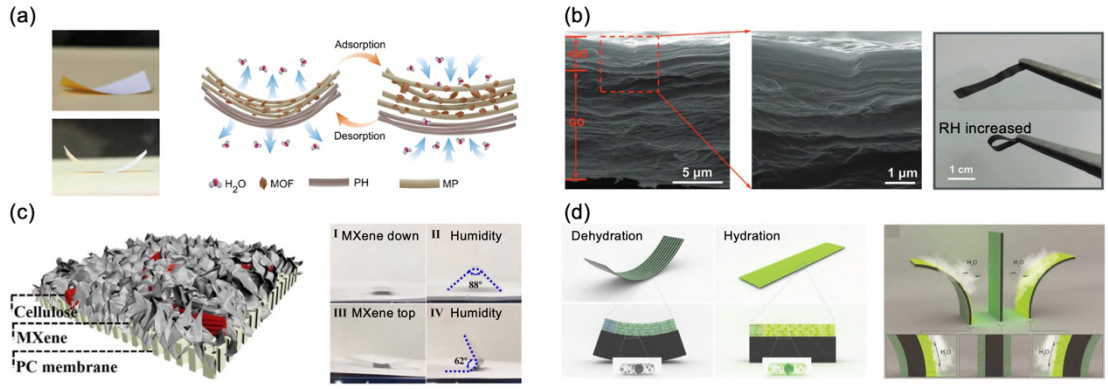

Figure 2.3 Typical structural designs of bilayer hygroscopic membranes. (a) PH/MP bilayer hygroscopic membrane (adapted from [79]). (b) rGO/GO bilayer hygroscopic

membrane (adapted from [89]). (c) MXene/PC bilayer hygroscopic membrane (interface strengthened by cellulose) (adapted from [90]). (d) Latex sheet/hygroscopic cell bilayer hygroscopic membrane (adapted from [91]).

2.1.3 Programmed thin-film materials

Monolayer and bilayer structures represent the most fundamental structures of hygroscopic membranes, typically producing simple bending deformations. To enable more complex and controllable configurations, programmable structures have emerged as a key strategy in the structural design of hygroscopic membranes.

Among these structures, the most straightforward approach is to directly assemble two hygroscopic membranes, with the assembly configuration tailored to achieve the designed deformation mode [92-94]. For example, connecting the active layers of two identical hygroscopic membranes in a head-to-tail manner can transform a simple bending deformation into an S-shaped motion. Moreover, a wavy configuration can be realized if multiple hygroscopic membranes are connected accordingly (**Figure 2.4 (a)**) [95]. Similarly, linking the ends of a single hygroscopic membrane to form a closed elliptical loop enables rolling locomotion under humidity stimulation, driven by curvature changes at different locations (**Figure 2.4 (b)**) [96]. However, such a method introduces additional interfacial vulnerabilities, significantly reducing the operational lifespan of the hygroscopic membranes.

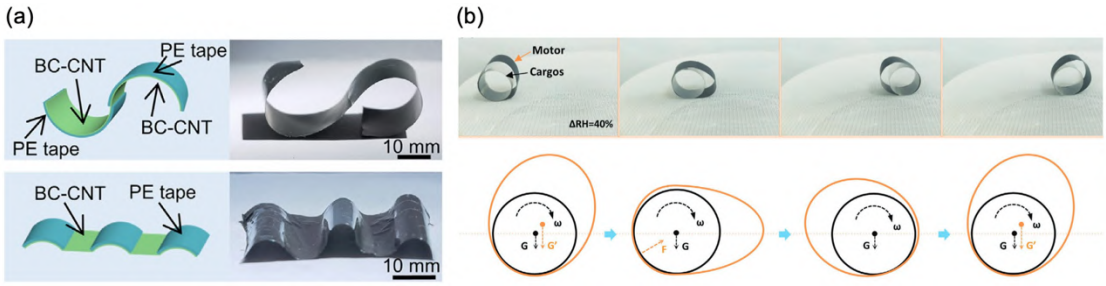

Figure 2.4 Direct assembly of hygroscopic membranes. (a) Hygroscopic membranes connecting head to tail to realize an S-shape and a wavy shape deformed configuration (adapted from [95]). (b) Single hygroscopic membrane forming a closed elliptical loop to realize rolling locomotion (adapted from [96]).

Another approach to achieving programmable structures is to design the spatial pattern of the active layer [97, 98]. In bilayer hygroscopic membranes, the active layer can be selectively distributed on the inert layer. For instance, by locally transferring GO films onto a PE substrate, deformation occurs only in the GO-coated regions upon humidity stimulation, enabling programmed deformation profiles. This method can produce various deformed configurations, such as V-shaped, helical, and wavy deformations (**Figure 2.5 (a)**) [42]. Similarly, patterned masks can be used to locally introduce ionic solutions into polymer membranes, allowing for spatially controlled active regions that respond to humidity with helixing and rolling configurations **Figure 2.5 (b)**) [99]. For single-layer films, the straightforward strategy is to apply surface microstructures asymmetrically on one side of the film. For example, by introducing asymmetric surface designs on both sides of a monolayer GO hygroscopic film, twisting deformation can be achieved under humidity stimulation (**Figure 2.5 (c)**) [100].

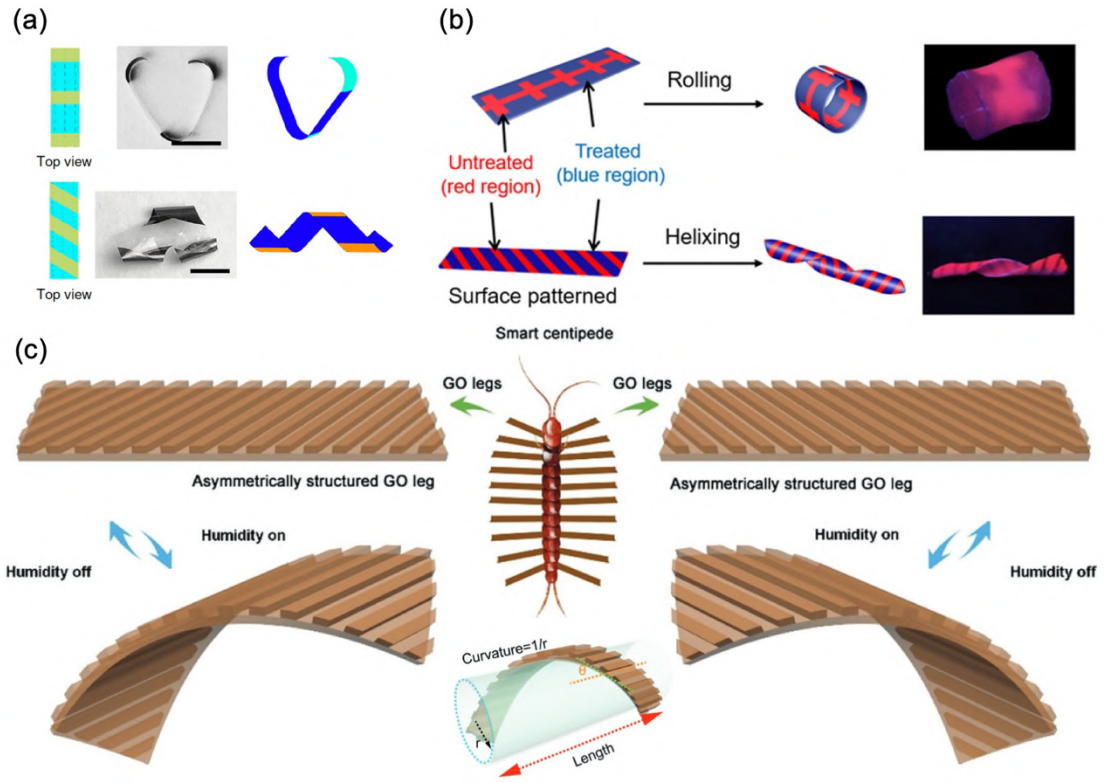

Figure 2.5 Patterned design of hygroscopic membranes. (a) Partial deposition of active layer on inert layer of bilayer hygroscopic membrane (adapted from [42]). (b) Local diffusion of ionic solution in the inert layer of the bilayer hygroscopic membrane (adapted from [99]). (c) Introduction of asymmetric microstructures on different sides of a monolayer hygroscopic membrane (adapted from [100]).

A less common method is the origami technique [101, 102]. In this approach, the hygroscopic membrane is folded into a predetermined shape and remains in this configuration before stimulation. Upon exposure to humidity, the film unfolds and deforms along the predesigned folding directions. The underlying mechanism is that internal stress is introduced during the folding process; when the film absorbs moisture and undergoes hygroscopic expansion, this internal stress is released, driving the programmed deformation. One strategy to achieve this is to assemble the active layer onto the passive layer following a predesigned origami pattern, forming a bilayer

hygroscopic membrane (**Figure 2.6 (a)**) [103]. Another approach is to directly fold a single-layer hygroscopic membrane, which is free of the interfacial weakness (**Figure 2.6 (b)**) [104].

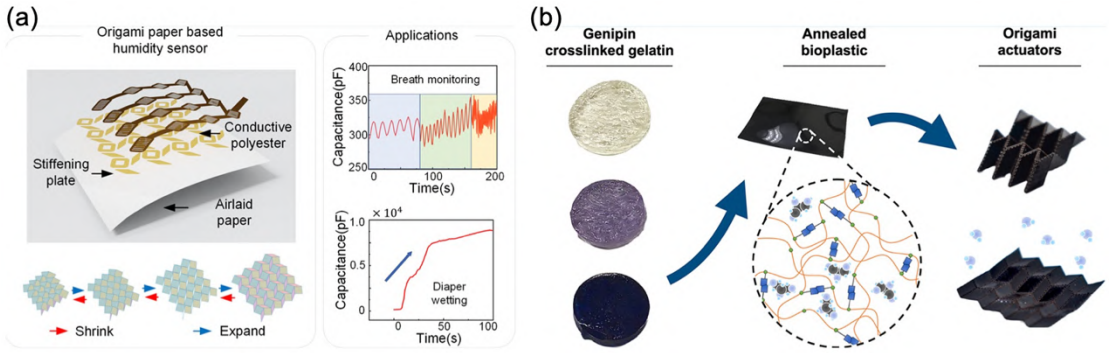

Figure 2.6 Origami structure of hygroscopic membranes. (a) Origami-designed active layer attached to an inert layer of hygroscopic membrane (adapted from [103]). (b) Origami-designed folding process of monolayer hygroscopic membrane (adapted from [104]).

2.2 Fundamental mechanics of thin-film materials

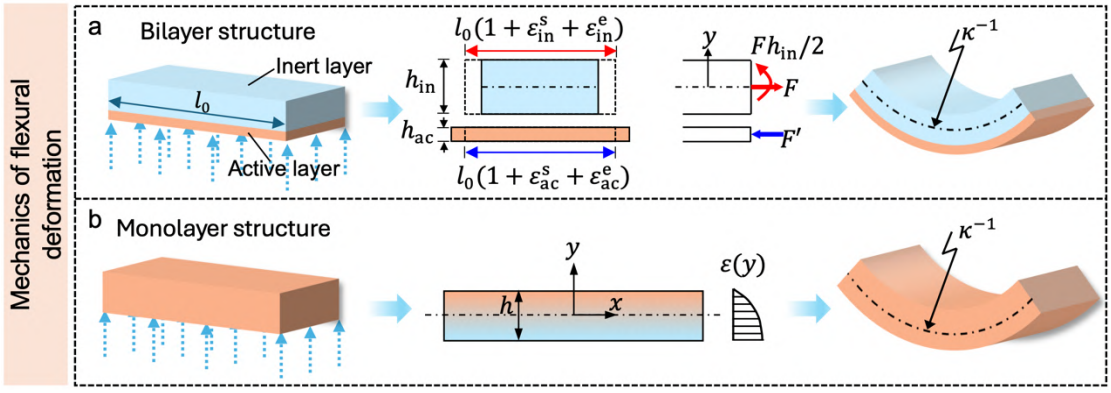

Figure 2.7 Schematic illustration showing the mechanics of flexural deformation of thin-film materials

Bending represents the most fundamental deformation mode of membrane

materials, even though more complex morphologies can be achieved through topological design. Gaining a thorough understanding of the mechanics governing bending deformation is therefore crucial for the rational design and precise control of such membranes. Meanwhile, although different stimulus-responsive materials rely on distinct response mechanisms, the fundamental mechanics underlying their deformation are universal. As a representative case, the bilayer-type membrane can be modeled as a Euler–Bernoulli beam under plane stress, composed of an inert substrate and a much thinner active layer (**Figure 2.7 (a)**, with $h_{\mathrm{ac}} \ll h_{\mathrm{in}}$). When subjected to external stimuli, the two layers undergo different expansion, giving rise to a mismatch strain defined as $\varepsilon_{\mathrm{mis}} = \varepsilon_{\mathrm{in}}^{\mathrm{s}} - \varepsilon_{\mathrm{ac}}^{\mathrm{s}}$, where $\varepsilon_{\mathrm{in}}^{\mathrm{s}}$ and $\varepsilon_{\mathrm{ac}}^{\mathrm{s}}$ denote the stimulus-induced strains of the inert and active layers, respectively. For example, under a change in moisture concentration ΔC, the mismatch strain can be expressed as $\varepsilon_{\mathrm{mis}} = (\beta_{\mathrm{ac}} - \beta_{\mathrm{in}})\Delta C$, where β_{ac} and β_{in} representing the hygroscopic expansion coefficients of the active and inert layers. To accommodate this interfacial mismatch, non-uniform yet self-equilibrated stresses arise within the cross-section, ultimately inducing flexural deformation of the membrane. The bending curvature κ, according to the Stoney relation for thin-film and substrate systems [105], can be written as

$$\kappa = \frac{6\sigma_{\mathrm{ac}} h_{\mathrm{ac}}}{E_{\mathrm{in}} h_{\mathrm{in}}^2} \tag{2.1}$$

where E_{in} is plane-strain modulus of the inert layer and σ_{ac} is the mean stress in the active layer. Accommodation of the mismatch strain between the two layers across the interface requires

$$\varepsilon_{\mathrm{ac}}^{\mathrm{e}} - \varepsilon_{\mathrm{in}}^{\mathrm{e}} = \varepsilon_{\mathrm{mis}}$$

here, $\varepsilon_{\mathrm{in}}^{\mathrm{e}}$, $\varepsilon_{\mathrm{ac}}^{\mathrm{e}}$ denote the elastic strains of the inert and active layers adjacent to the interface. According to the Euler–Bernoulli beam theory, these strains can be expressed as $\varepsilon_{\mathrm{ac}}^{\mathrm{e}} = \frac{\sigma_{\mathrm{ac}}}{E_{\mathrm{ac}}}$ and $\varepsilon_{\mathrm{in}}^{\mathrm{e}} = -\frac{4\sigma_{\mathrm{ac}}h_{\mathrm{ac}}}{E_{\mathrm{in}}h_{\mathrm{in}}}$. By combining the above relations, the mismatch strain can thus be directly related to the mean stress in the active layer through

$$\varepsilon_{\mathrm{mis}} = \left[\frac{1}{E_{\mathrm{in}}} \cdot \frac{4h_{\mathrm{ac}}}{h_{\mathrm{in}}} + \frac{1}{E_{\mathrm{ac}}}\right] \sigma_{\mathrm{ac}} \tag{2.2}$$

Combining Eq. (2.1) and Eq. (2.2) to eliminate σ_{ac} yields the bending curvature as a function of the mismatch strain

$$\kappa = \frac{6h_{\mathrm{ac}}}{h_{\mathrm{in}}} \left[\frac{E_{\mathrm{ac}}}{4E_{\mathrm{ac}}h_{\mathrm{ac}} + h_{\mathrm{in}}E_{\mathrm{in}}}\right] \varepsilon_{\mathrm{mis}} \tag{2.3}$$

Eq. (2.3) shows the proportionality between the bending curvature (κ) and the mismatch strain ($\varepsilon_{\mathrm{mis}}$), which also applies to bilayer membranes with active layer and inert layer of comparable thicknesses [105].

For a monolayer membrane (**Figure 2.7(b)**) exhibiting homogeneous properties—namely, Young's modulus *E*, and Poisson's ratio ν, and coefficient of stimulus-induced expansion β—a fundamental mechanical analysis based on the Euler-Bernoulli beam theory under the plane stress assumption reveals that the axial stress induced by a non-uniform stimulus $\Delta S(y)$ can be expressed as

$$\sigma_x(y) = -E\varepsilon^{\mathrm{s}}(y) + \frac{E}{h}\int_{-\frac{h}{2}}^{\frac{h}{2}} \varepsilon^{\mathrm{s}}(y)dy + \frac{12yE}{h^3}\int_{-\frac{h}{2}}^{\frac{h}{2}} \varepsilon^{\mathrm{s}}(y)ydy$$

where h is the thickness of the membrane and $\varepsilon^{\mathrm{s}}(y) = \beta\Delta S(y)$. The variation of

stimulation along the longitudinal direction (x-direction) is neglected. It can be verified that $\sigma_x(y)$ is self-balanced as $\int_{-\frac{h}{2}}^{\frac{h}{2}} \sigma_x(y)dy = 0$ and $\int_{-\frac{h}{2}}^{\frac{h}{2}} y\sigma_x(y)dy = 0$. The elastic strain induced by this self-balanced stress is given by

$$\varepsilon^{\mathrm{e}}(y) = \frac{\sigma_x(y)}{E} = -\varepsilon^{\mathrm{s}}(y) + \frac{1}{h}\int_{-\frac{h}{2}}^{\frac{h}{2}} \varepsilon^{\mathrm{s}}(y)dy + \frac{12y}{h^3}\int_{-\frac{h}{2}}^{\frac{h}{2}} \varepsilon^{\mathrm{s}}(y)ydy$$

The total strain (ε^{t}), which is equal to the summation of the elastic strain and the stimulus-induced strain, is given by

$$\varepsilon^{\mathrm{t}}(y) = \varepsilon^{\mathrm{e}}(y) + \varepsilon^{\mathrm{s}}(y) = \frac{1}{h}\int_{-\frac{h}{2}}^{\frac{h}{2}} \varepsilon^{\mathrm{s}}(y)dy + \frac{12y}{h^3}\int_{-\frac{h}{2}}^{\frac{h}{2}} \varepsilon^{\mathrm{s}}(y)ydy$$

The first term on the right-hand side of the above expression is independent of y and therefore leads to no bending deformation, while the second term is a linear function of y, which leads to a flexural configuration with curvature κ given by

$$\kappa = \frac{12}{h^3}\int_{-\frac{h}{2}}^{\frac{h}{2}} \varepsilon^{\mathrm{s}}(y)ydy \tag{2.4}$$

2.2.1 Deformation mechanism of hygroscopic membranes

According to the theoretical analysis of the thin-film materials above, the deformation of hygroscopic membranes relies on the physical or chemical processes that generate hygroscopic strain in the active materials. A thorough understanding of the deformation mechanisms of hygroscopic membranes is essential for identifying suitable application scenarios and overcoming limitations to enable their further development.

Hygroscopic membranes exploit materials rich in polar molecules or functional groups to absorb water molecules from the surrounding environment, leading to volumetric expansion [106, 107]. The dominant deformation mechanism of such membranes is water-induced swelling of the constituent materials [106, 108, 109]. For example, stacked assemblies of 2D material flakes, such as MXene and graphene oxide (GO), are frequently used as hygroscopic components in these membranes [107] because of their abundant hydroxyl groups that strongly attract water. The uptake of water molecules increases the interlayer spacing (d-spacing) between the nanoflakes in the stacked assemblies, resulting in hygroscopic expansion. MXene itself can be utilized to develop a monolayer hygroscopic membrane [62] (**Figure 2.8 (a)**). The actuator, when placed above hot water (40°C), can flip over back and forth. If clamped at one end, it will swing up and down automatically [62] (**Figure 2.8 (b)**). Similar flapping motion under steady humidity stimulation can also be achieved by GO-based hygroscopic membranes (**Figures 2.8 (c-d)**) [39], implying the presence of a common governing mechanism which remains obscure so far.

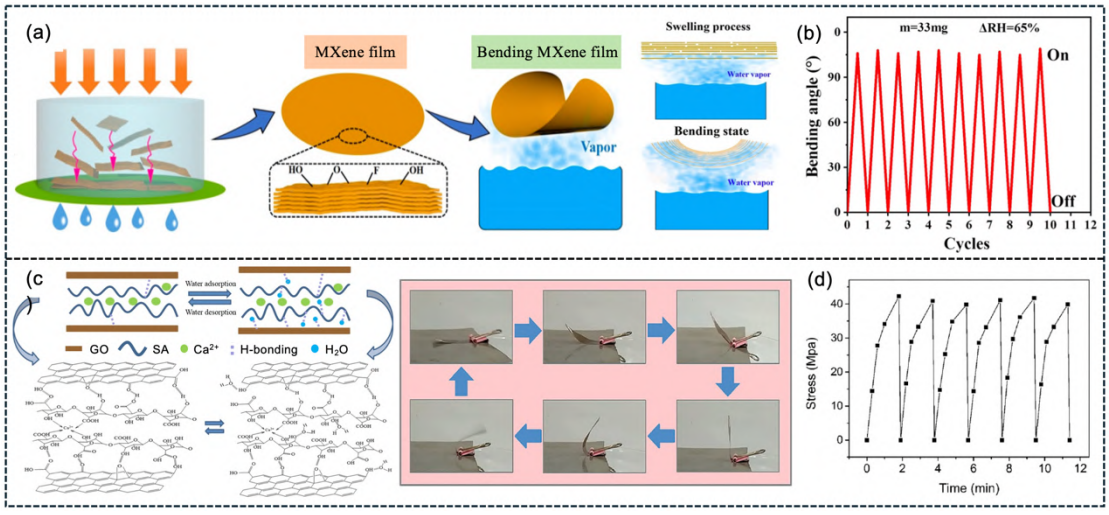

Figure 2.8 (a) Schematic illustration showing the fabrication process and deformation mechanism of MXene-based hygroscopic membranes. (b) Swinging motion of MXene-based hygroscopic membranes. (adapted from [62]) (c) Deformation mechanism of GO/SA-based hygroscopic membrane and its flapping response in steady moisture stimuli. (d) Stress variation of the GO/SA membrane in absorption/desorption cycles. (adapted from [39])

Another deformation mechanism in hygroscopic membranes involves the disruption of chemical bonds within hygroscopic materials, such as polyimide (PI) [82], and sodium alginate (SA) [54, 110, 111]. For example, SA swells upon water absorption as water molecules infiltrate its polymer network, breaking intermolecular hydrogen bonds and converting the polymer chains into a hydrated structure [31, 112]. SA is composed of β-D-mannuronic acid (M-blocks) and α-L-guluronic acid (G-blocks), both of which contain abundant carboxyl groups. These groups can form hydrogen bonds and electrostatic interactions with water molecules, further enhancing hygroscopic swelling [113, 114]. For instance, SA was applied as the active material and PDMS as the inert material to develop a bilayer Hygroscopic membrane [54] (**Figures 2.9 (a-b)**). Upon water absorption, the active SA layer undergoes expansion, inducing bending of the actuator. However, this mechanism is limited by a prolonged recovery time due to the slow relaxation of polymer chains during desorption, as well as reduced mechanical performance caused by SA degradation under humid conditions. To overcome these limitations, carbon nanofibers (CNFs) are incorporated into the SA matrix as reinforcement [115] (**Figures 2.9 (c-d)**). The abundant hydroxyl groups on CNFs

impart high humidity responsiveness to the hygroscopic membrane. Moreover, the large specific surface area of CNFs promotes water desorption, thereby facilitating faster recovery of the membrane in low-humidity environments.

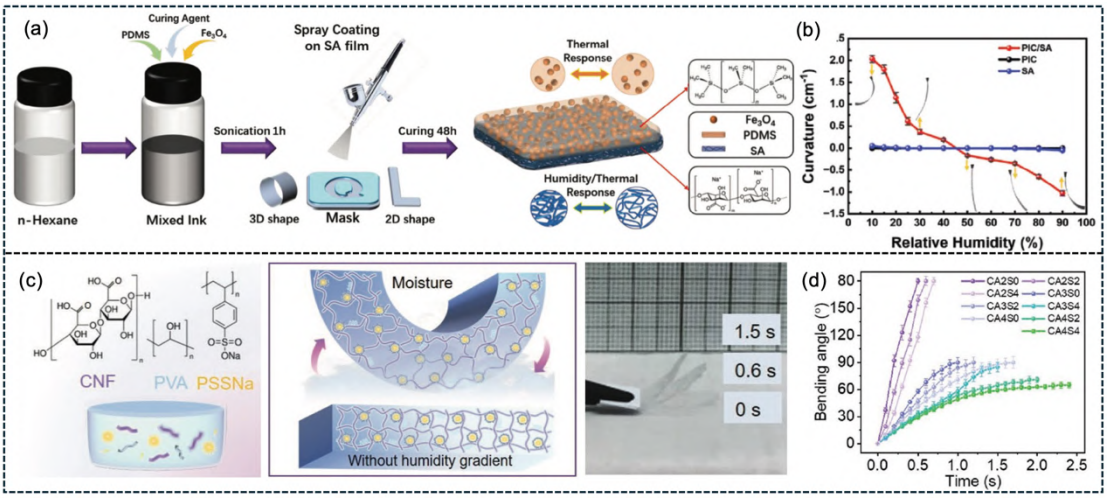

Figure 2.9 (a) Schematic illustration showing the fabrication process and deformation mechanisms of the SA-based hygroscopic membrane. (b) Curvature variation of the SA-based hygroscopic membrane under different relative humidity. (adapted from [54]) (c) Deformation mechanism of CNF/PVA/PSSNa-based hygroscopic membranes. (d) Bending angle of CNF/PVA/PSSNa-based hygroscopic membranes under humidity stimuli. (adapted from [115])

In natural materials, the deformation mechanism originates from the hygroscopic swelling of cellulose or biological cells. For example, wood is a commonly used natural material for fabricating hygroscopic membranes due to its excellent mechanical properties and relatively high hygroscopic expansion coefficient. The porous structure of wood enables substantial water absorption, and the cellulose fibers within it swell upon hydration, leading to macroscopic hygroscopic deformation (**Figure 2.10 (a)**) [116]. Similarly, certain bacterial spores possess finer microporous structures that allow

them to absorb moisture and undergo volumetric expansion. These spores can be deposited onto a non-active substrate to form bilayer hygroscopic films (**Figure 2.10 (b)**) [117].

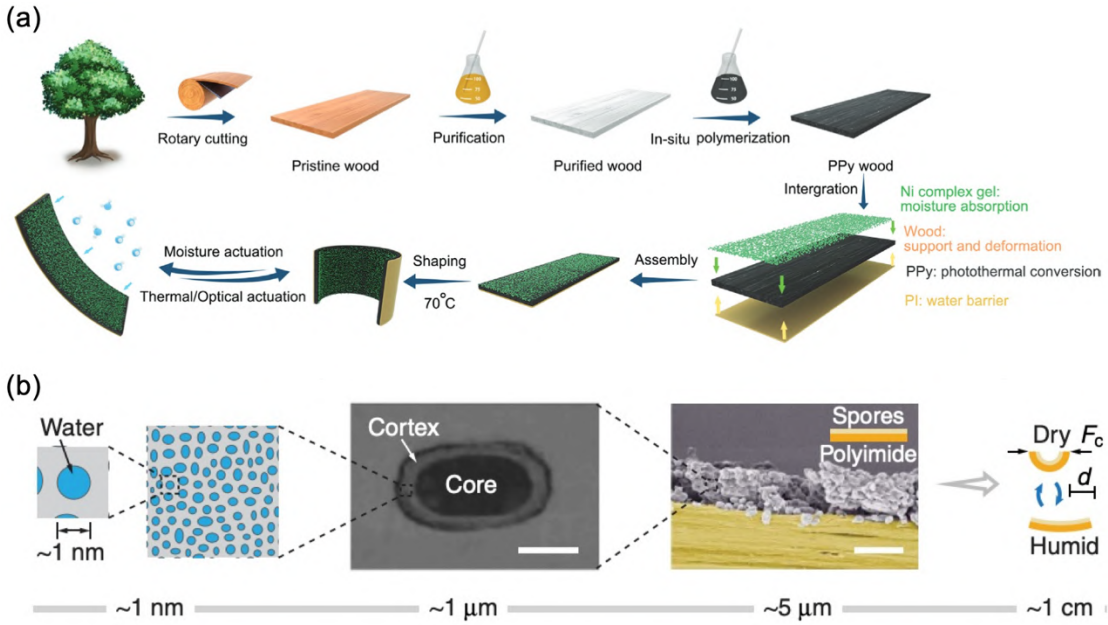

Figure 2.10 Deformation mechanism of hygroscopic membranes made by (a) Wood materials (adapted from [116]) and (b) Living spores (adapted from [117]).

Despite these advances in hygroscopic membranes, several issues remain unresolved. First, although the interlayer spacing (d-spacing) between nanoflakes in 2D material-based films increases upon water absorption, it does not necessarily induce in-plane expansion, which is essential for bending deformation. The underlying mechanism responsible for in-plane expansion in such films remains unclear. Furthermore, the autonomous flapping behavior of hygroscopic membranes under steady stimulation suggests a reversible water absorption–desorption process coupled with dynamic water transport across the film thickness. Elucidating this mechanism is

critical for optimizing the practical applications of hygroscopic membranes.

2.3 Existing moisture-driven actuators and devices

The deformation mechanisms of various TFAs provide insights into how external stimuli trigger the mechanical motion of TFAs. Owing to their lightweight nature, high flexibility, remarkable sensitivity, and programmability, TFAs show great potential for a wide range of applications, particularly in biomimetic soft robotics, energy-harvesting devices, and intelligent wearable devices.

2.3.1 Biomimetic soft actuators

Due to their low stiffness, rapid responsiveness, and ease of processing, hygroscopic membranes are highly suitable for application in bioinspired actuators [118-120]. For example, by directly assembling hygroscopic membranes into a cross-shaped configuration, the membranes can bend in different directions under humidity stimulation, mimicking the contraction of lotus petals or the closure of peony buds (**Figure 2.11 (a)**) [121]. Beyond these simple shape-mimicking demonstrations, hygroscopic membranes can also be employed in bioinspired functional actuators. In a crab-inspired actuator, for instance, the crab's legs are made from hygroscopic membranes, and their coordinated bending under humidity enables a crab-like lateral movement (**Figure 2.11 (b)**) [119]. Alternatively, to achieve directional locomotion, the surface beneath the actuator can be designed into a ratchet-like structure, creating lower resistance in the forward direction than in the reverse [122, 123]. Based on this

mechanism, a single hygroscopic membrane can be engineered into a crawling bioinspired actuator inspired by caterpillars (**Figure 2.11 (c)**) [124]. Moreover, hygroscopic membranes can also be used to fabricate biomimetic grippers [58, 125]. By assembling the membrane into shapes similar to a human hand or an eagle's claw, it becomes possible to grasp objects through humidity-controlled actuation (**Figures 2.11 (d-f)**) [61, 116]. A further example is a biomimetic *Erodium gruinum* awn fabricated from a hygroscopic membrane, which undergoes spiral deformation to coil around objects upon humidity stimulation (**Figure 2.11 (f)**) [61]. Additionally, inspiration from frogs has led to designs where hygroscopic deformation stores significant strain energy under humid conditions. When the stimulus is removed, the rapid release of this strain causes the film to jump, converting stored strain energy into kinetic energy (**Figure 2.11 (g)**) [126].

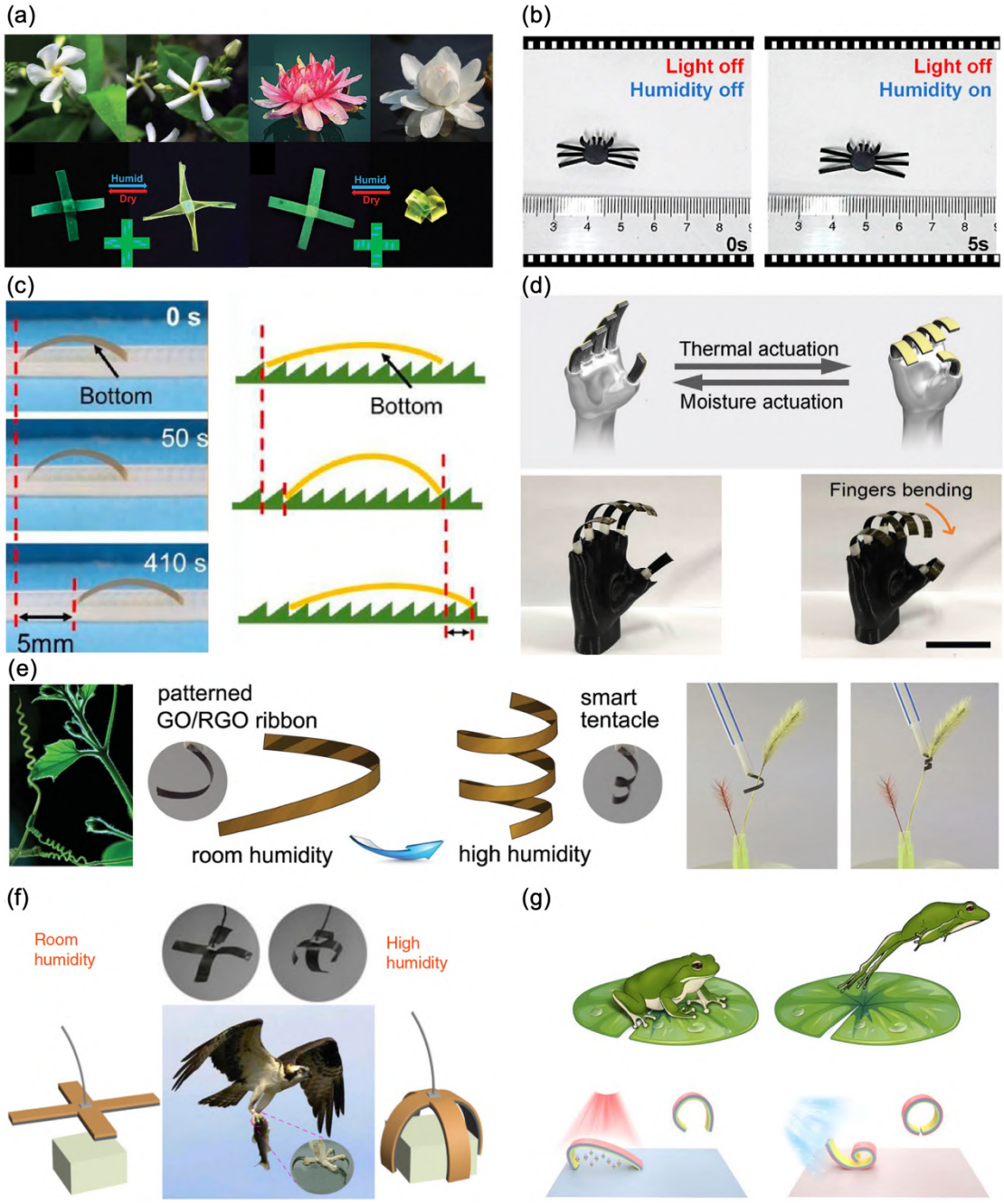

Figure 2.11 Hygroscopic membranes applied in biomimetic actuators. (a) Moisture-driven artificial lotus and peony (adapted from [121]). (b) Moisture-driven biomimetic crab (adapted from [119]). (c) Moisture-driven caterpillar-inspired locomotion actuator (adapted from [124]). (d) Moisture-driven human hand-inspired soft gripper (adapted from [116]). (e) Moisture-driven *Erodium gruinum*-inspired soft gripper (adapted from [61]). (f) Moisture-driven hawk claw-inspired soft gripper (adapted from [61]). (g) Moisture-driven frog-inspired jumping actuator (adapted from [126]).

2.3.2 Energy harvesting devices

Hygroscopic membranes can also be utilized to transfer external stimuli into electrical energy through various mechanisms [127, 128]. One direct strategy for energy conversion is to exploit electromagnetic induction to transform the dynamic motion of hygroscopic membranes into electrical energy [117]. For instance, a hygroscopic membrane placed within a magnetic field can generate electricity when stimulated by humid airflow [129] (**Figure 2.12 (a), (b)**). Another method utilizes the piezoelectric effect, whereby electricity is produced through enhanced directional proton diffusion under applied pressure [130, 131]. As an example, a hygroscopic membrane combining MXene, cellulose, and a piezoelectric component based on polystyrene sulfonic acid (PSSA) was developed. Under humidity stimulation, this generator achieved a high power density of 81.2 μW/cm³ and an open-circuit voltage of 0.3 V [132] (**Figure 2.12 (c), (d)**). In addition, hygroscopic membranes can also generate electricity via the triboelectric effect, in which frictional contact between positively and negatively charged layers induces electrical charges [133-135]. In such designs, the frictional layers are typically sandwiched between inert layers. For instance, the active PVA film can generate wrinkle structures upon moisture absorption due to mismatch strain, which increases the surface roughness (**Figure 2.12 (e)**). Upon pressing, the friction between the PVA/LiCl layer and the PVDF layer can generate electricity (**Figure 2.12 (f)**) [136]. Moreover, ion migration has also been applied in energy harvesting systems driven by hygroscopic membranes [137, 138]. For instance, bending deformation of a

hygroscopic membrane facilitates directional migration of sodium ions within poly(sodium 4-styrenesulfonate) (PSS), generating a current of 32 μA [139] (**Figure 2.12 (g), (h)**).

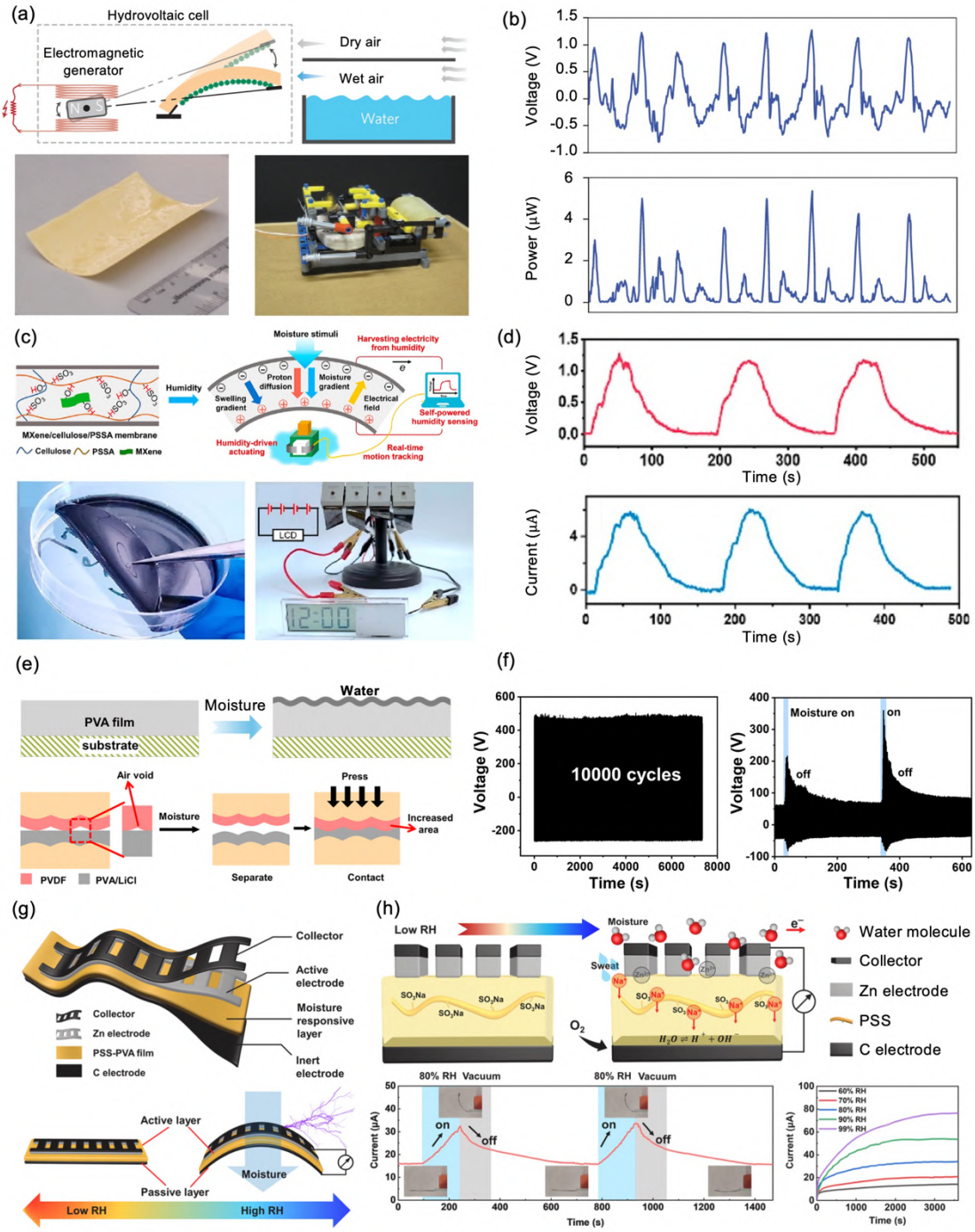

Figure 2.12 Hygroscopic membranes applied in energy harvesting. (a) Hygroscopic generator based on electromagnetic induction. (b) Induced voltage and power of such a

generator. ((a,b) adapted from [129]) (c) Hygroscopic generator based on the piezoelectric effect. (d) Induced voltage and current of such a generator. ((c,d) adapted from [132]) (e) Hygroscopic generator based on the triboelectric effect. (f) Output voltage of such a generator. ((e,f) adapted from [136]) (g) Hygroscopic generator based on ion migration. (h) Schematic illustration of such a generator and its output current. ((g,h) adapted from [139])

2.3.3 Wearable devices

In addition, hygroscopic membranes can be also applied in wearable devices. During physical activity, the human body releases a significant amount of perspiration in the form of water vapor, which can be used to trigger hygroscopic films [140, 141]. These membranes respond by unfolding, thereby enhancing heat dissipation to cool the body. Furthermore, smart textiles fabricated from hygroscopic yarns have been integrated into wearable systems (**Figures 2.13 (a-b)**) [91, 142]. For instance, sleeves made from such fabrics can automatically contract upon exposure to sweat, revealing more skin to improve cooling. Once the moisture evaporates and the skin dries, the sleeves gradually return to their original length, helping to retain body heat (**Figure 2.13 (c)**) [143].

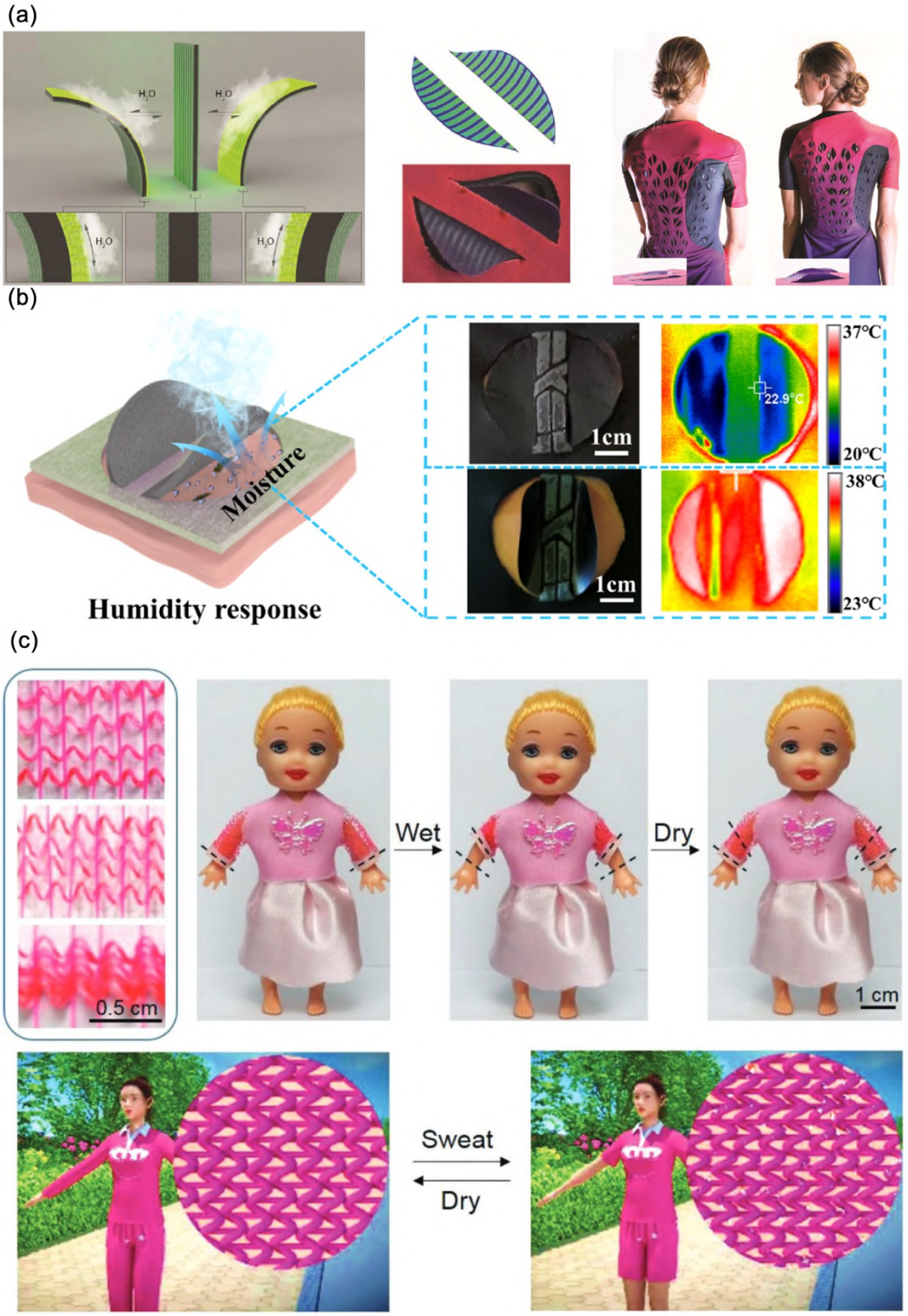

Figure 2.13 Hygroscopic membranes applied in wearable devices. (a) Sportswear prototype with microorganism/latex winglets (adapted from [91]). (b) Concept of hygroscopic membrane-based smart garment (adapted from [142]). (c) Smart sleeves

made from hygroscopic textiles (adapted from [143]).

This chapter has reviewed the structural design, fundamental mechanical mechanisms, and current application landscape of hygroscopic membranes. Although the basic configurations of hygroscopic membranes are relatively simple—primarily monolayer and bilayer structures—existing studies offer limited analysis of their deformation configurations under humidity stimuli, particularly under different boundary conditions such as cantilevered or free-standing states. Current research merely attributes their deformation behavior to strain mismatch between active and inert layers, without further quantifying or predicting the resulting deformation configurations. To address this gap, this thesis will systematically investigate the humidity-induced deformation mechanisms of hygroscopic membranes under various humidity stimuli.

In addition, unlike bilayer systems, monolayer hygroscopic membranes have been widely reported to exhibit autonomous oscillations under humidity gradients [39, 144]. This phenomenon holds significant potential for applications in energy harvesting and soft actuators. However, the underlying mechanics and rational control of such behavior remain inadequately explored. Therefore, this thesis will conduct a systematic mechanical analysis of this oscillatory behavior and, based on the results, propose design strategies to optimize the performance of monolayer hygroscopic membranes in the aforementioned application domains.

Chapter 3. Research methods

3.1 Fabrication of hygroscopic materials

The single-layer MXene flakes are fabricated using the selective etching method by removing the Al atoms from Ti_3AlC_2 MAX phase [145, 146], as illustrated in **Figure 3.1 (a)**. First, 40 mL of hydrochloric acid (9 M) was mixed with 3.2 g of pure LiF powder. Then, 2 g MAX phase will be added into the solution slowly under continuous magnetic stirring at a temperature of 40 ℃. After 48 h, the dispersion will be washed with water with centrifugation at 3500 rpm for 3 minutes several times. When the pH value of the dispersion is near 6, a dispersion composed of single-layer MXene flakes is obtained. Plain MXene membranes are prepared by vacuum filtration of the single-layer MXene solution. To prepare the MXene/NP membranes, the prepared MXene flake suspension will first be ultrasonicated for 30 mins. During this process, Fe_3O_4 nanoparticles (with a size of 100 nm in diameter), which are synthesized using the Stöber method [147], are added to the solution. Afterwards, the membranes are fabricated by vacuum filtration of the corresponding dispersion and peeled off from the cellulose membrane after drying under ambient conditions for 6 hours.

The GO/SA membranes are made by directly mixing a single-layer GO flakes dispersion (5 mg/ml) with a sodium alginate solution (2 wt%), followed by 24 h of stirring for sufficient mixture. After that, the mixture is poured into a Perti dish for

evaporation at room temperature, resulting in a GO/SA composite membrane (**Figure 3.1 (b)**).

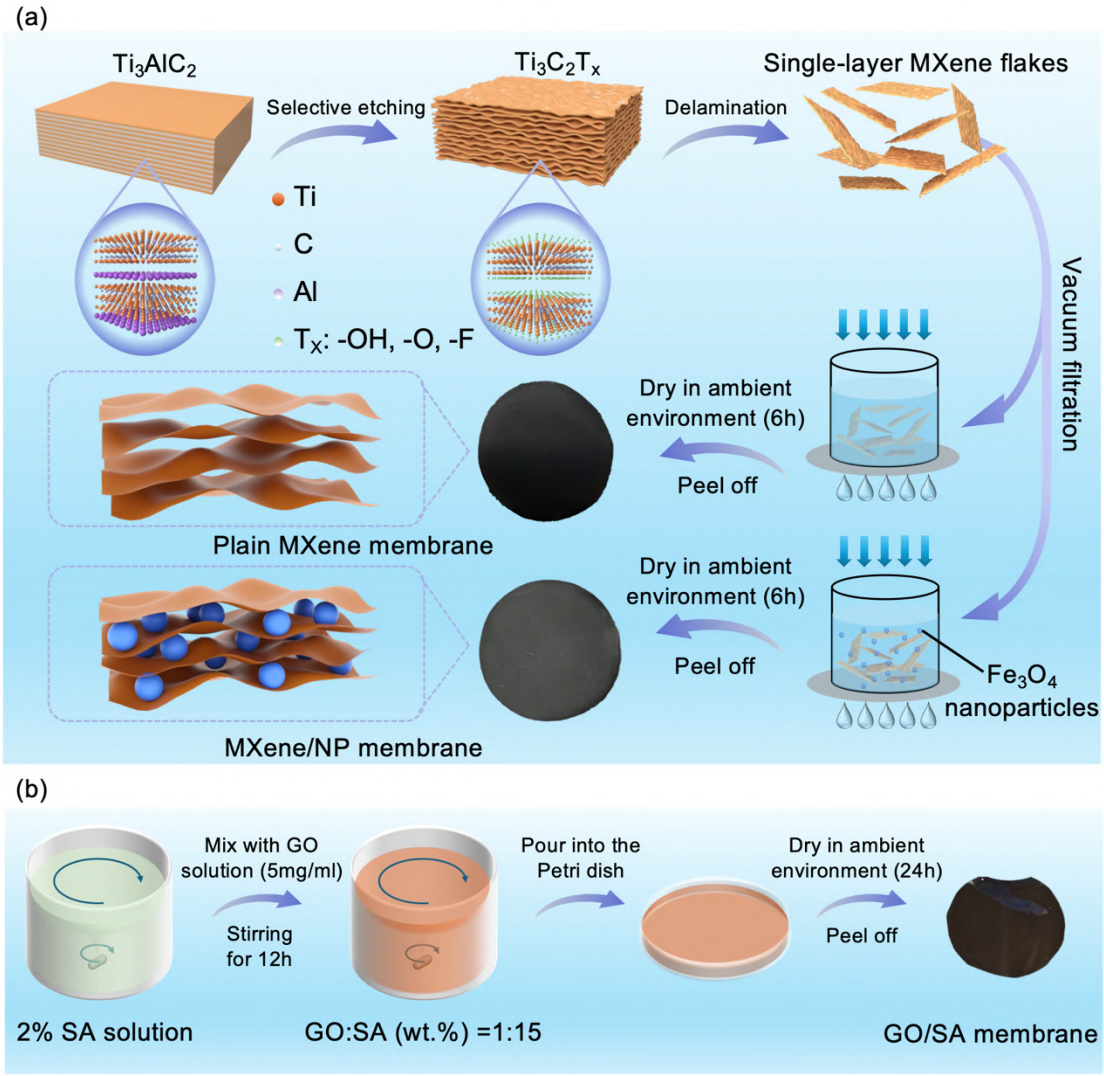

Figure 3.1 Schematic illustration of the fabrication process of (a) MXene/NP and plain MXene membranes, (b) GO/SA membranes.

3.2 Characterizations of hygroscopic materials

Thickness measurement of MXene/NP and GO/SA membranes

The cross-sectional images of MXene/NP and GO/SA membranes were obtained by Scanning Electron Microscopy and Optical Microscopy. The thickness of the

MXene/NP membrane is ~12 μm, and the thickness of GO/SA membrane is ~20 μm.

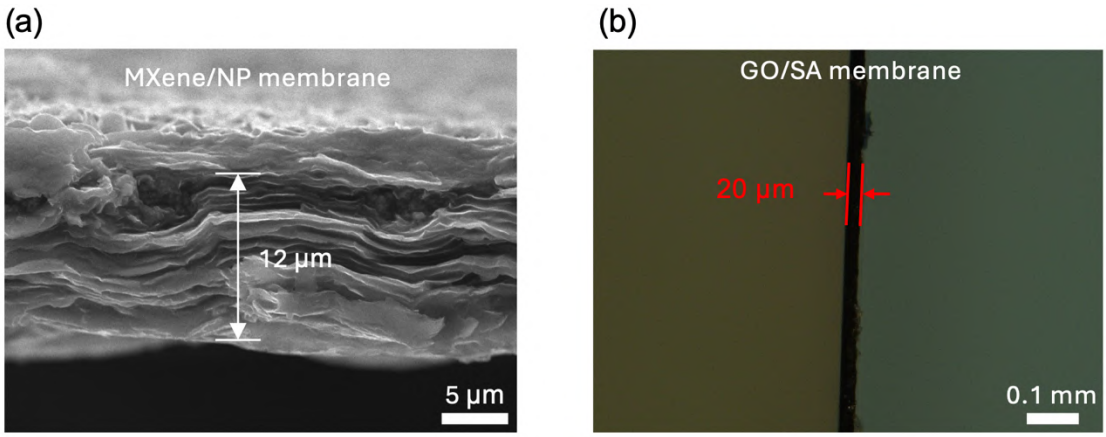

Figure 3.2 The cross-sectional image of (a) MXene/NP membrane, (b) GO/SA membrane.

Measurement of Young's modulus of SNA membranes

Uniaxial tensile tests were carried out for SNA membranes to determine their Young's modulus. The SNA membranes were tailored into a strip shape. The Dynamic Mechanical Analyzer (DMA 8000, Perkin Elmer) was used to perform uniaxial tension tests on SNA membranes with a loading speed of 0.1mm/min.

Measurement of the hygroscopic expansion coefficient of SNA membranes

The hygroscopic expansion coefficients (HEC) of the SNA membranes (β) were measured by using a homemade bilayer sensor (**Figure 3.3 (a)**) composed of the tested SNA membrane (plain MXene, MXene/NP, or GO/SA) deposited on a non-hygroscopic PVC substrate with zero HEC. When the sensor is subjected to a change of moisture concentration (ΔC), a mismatch strain will be developed between the two layers: $\varepsilon_{\text{mis}} = \beta \Delta C$, leading to the bending deformation of the sensor. The value of β thus

can be determined from ε_{mis}-ΔC curves, which can be attained as follows. By measuring the curvature (κ) of the deformed bilayer, the value of the mismatch strain (ε_{mis}) can be determined, according to Stoney's theory [105, 148], through $\varepsilon_{mis} = \kappa \frac{h_{PVC}}{6h_{SNA}} \left[\frac{E_{SNA}}{4E_{SNA}h_{SNA}+h_{PVC}E_{PVC}}\right]^{-1}$, where E_{SNA}, E_{PVC}, h_{SNA}, h_{PVC} are the Young's moduli and thicknesses of the SNA and PVC layers, respectively. They can all be measured beforehand. On the other hand, the change of moisture concentration can be derived from the change of the relative humidity ($\Delta\emptyset$) through $\Delta C = \frac{P_T \Delta\emptyset}{RT}$, where P_T is the saturation vapor pressure at 20℃ (2334.6 Pa), T the ambient temperature (293 K), and $R = 8.314\ \mathrm{J/mol \cdot K}$ the ideal gas constant, respectively. Having determined ε_{mis} at different ΔC (**Figure 3.3 (b)**), β can be obtained from the slopes of the ε_{mis}-ΔC curves, as shown in **Figure 3.3 (c)**.

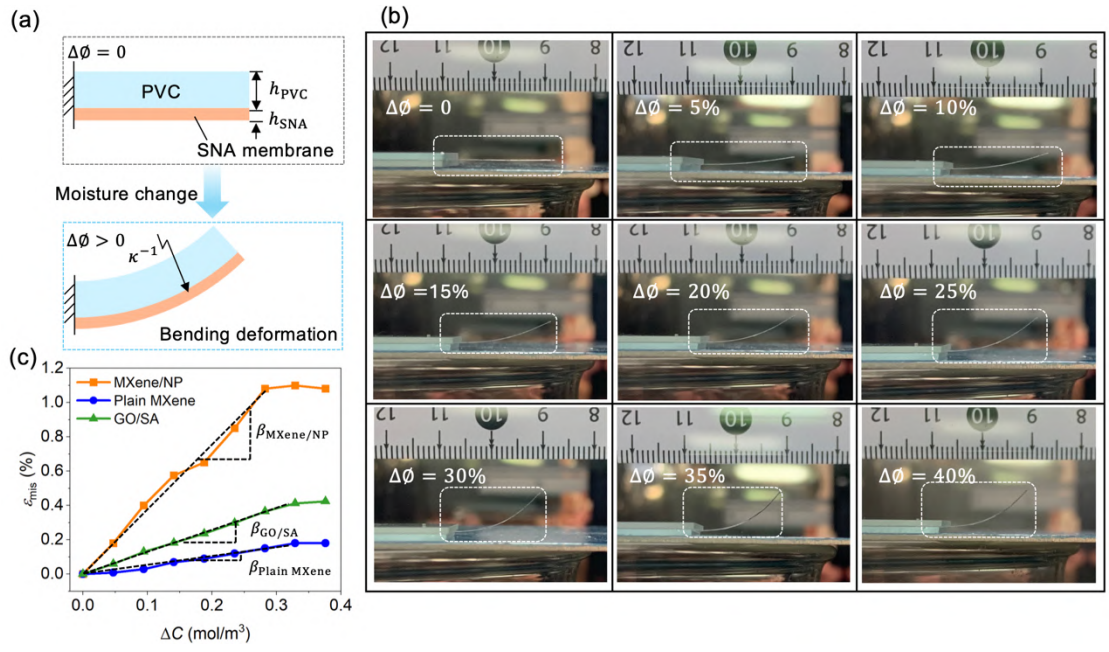

Figure 3.3 Hygroscopic expansion coefficient test of SNA membranes. (a) Schematic illustration of the bilayer sample composed of an SNA membrane and a PVC layer. (b) Snapshots of the curvature of a bilayer system of PVC and MXene/NP under different

relative humidity. (c) The relationship between hygroscopic expansion mismatch ($\varepsilon_{\mathrm{mis}}$) and moisture concentration change (ΔC) for different SNA membranes.

Effect of nanoparticle content on HEC of MXene/NP membrane

Firstly, Fe_3O_4 nanoparticles would undergo hydrophilization treatment by the Stöber method [149]. Different weight ratios of Fe_3O_4 nanoparticles were added to the single-layer MXene dispersion before vacuum filtration. The HECs of MXene/NP membranes with different nanoparticles were measured.

Measurement of diffusivity (D) within SNA membranes

According to Fick's law, the diffusivity of water in an SNA membrane can be determined from the measurable water vapor flux *J* caused by a given humidity gradient. To generate a humidity gradient, a bottle filled with water at 30 ℃ was sealed with a piece of tested membrane and placed in an environmental chamber with constant relative humidity 30% and constant temperature 30 ℃ (**Figure 3.4 (a)**), realizing a moisture gradient of $(C_{\mathrm{H}} - C_{\mathrm{L}})/h$, where C_{H} and C_{L} are the moisture concentrations on both sides of the tested membrane with thickness h. They can be determined from the saturation water vapor pressure at 30 ℃ ($P_{\mathrm{T}} = 4247.4$ Pa) and relative humidity (∅=30%) and temperature (*T*=303K) through $C_{\mathrm{L}} = \frac{P_{\mathrm{T}}\emptyset}{RT} = 0.505\ \mathrm{mol/m^3}$, $C_{\mathrm{H}} = \frac{P_{\mathrm{T}}}{RT} = 1.685\ \mathrm{mol/m^3}$, where $R = 8.314\ \mathrm{J/mol \cdot K}$ is the ideal gas constant. The water vapor flux *J* passing through the tested membrane was estimated from the mass loss in the bottle (m_{loss}) after a given period (*t*) through $J = \frac{m_{\mathrm{loss}}/t}{M_{\mathrm{r}} \cdot A_{\mathrm{out}}}$, where $M_{\mathrm{r}} = 18$ is the relative molecular mass of H_2O, A_{out} is the area of the outlet. According to Fick's law,

the diffusivity of water within the tested membrane was determined through $D = J \cdot h/(C_H - C_L)$ (**Figures 3.4 (b)**).

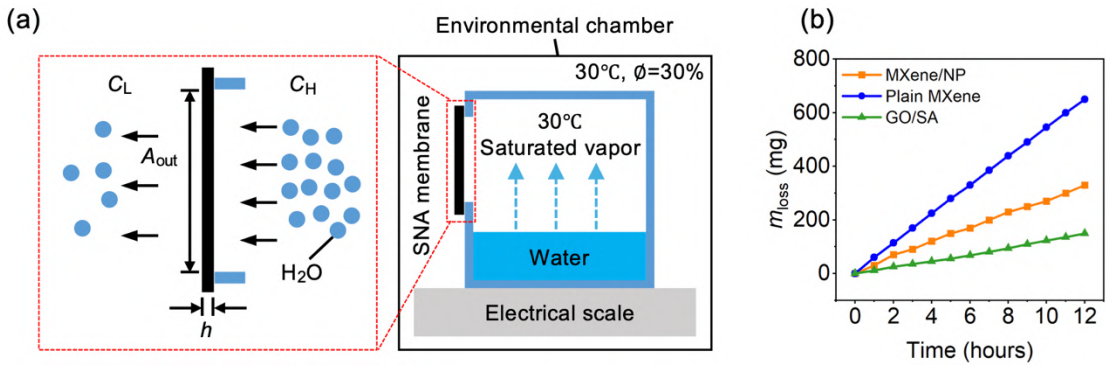

Figure 3.4 Measurement of diffusivity (D) of water within SNA membranes. (a) Schematic illustration of the experimental design. (b) The weight loss of water in the container as a function of time, from which the flux can be calculated.

Structural and characterization of SNA membranes

A field-emission scanning electron microscope (MIRA, Tescan) was used to investigate the surface and cross-sectional morphology of the MXene/NP membrane. The 2D X-ray diffraction (XRD) pattern of the MXene/NP membrane was recorded using Rigaku SmartLab 9 kW with Cu-Kα radiation ($\lambda = 1.5418$ Å). The resistance-humidity relationship of MXene samples was calibrated using a Digital Multimeter (DM3068, RIGOL) inside an environmental chamber (MC-80L, Mincee Instrument and Equipment CO., LTD.), where temperature (20-30℃) and humidity were precisely controlled ($\emptyset$ = 10 –100%).

3.3 Measurement of moisture distribution (environmental stimuli)

The vertical humidity distribution was characterized by using a piece of plain

MXene membrane as a resistive humidity sensor. The measurement protocol consisted of two steps: calibration and spatial mapping. First, the humidity-resistance correlation was established by placing the sensor in a controlled environmental chamber while monitoring its electrical response across a range of relative humidity (RH) levels (**Figure 3.5 (a)**). Following calibration, the sensor was vertically positioned at incremental heights above a vapor source—either a 40 °C water bath or a human palm—while recording the real-time resistance (**Figure 3.5 (b)**).

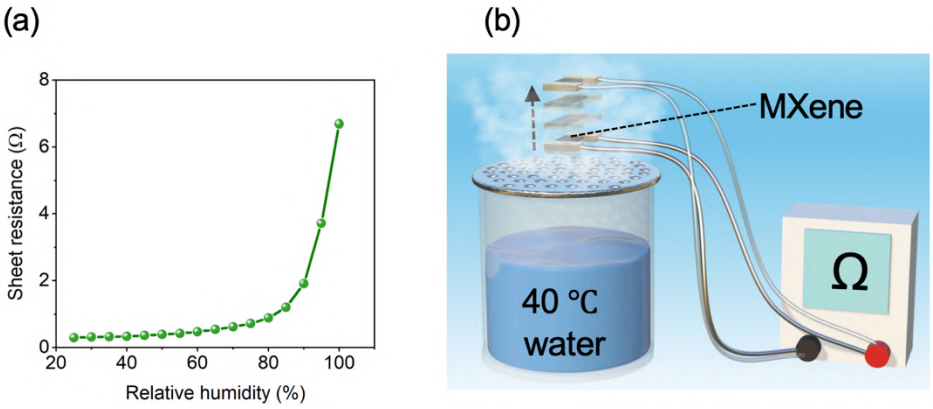

Figure 3.5 (a) Dependence of the sheet resistance of an MXene strip (as a humidity sensor) on the environmental relative humidity. (b) Schematic illustration of the measurement of the humidity gradient.

3.4 Finite element simulation

The moisture response of the bilayer hygroscopic membrane in different humidity fields was simulated in COMSOL using the Solid Mechanics and Hygroscopic Swelling modules. For the cantilever beam model, the left boundary of the membrane was fixed, with the inert layer and active layer having thicknesses of 50 μm and 10 μm, respectively. The moisture concentration in the active layer was defined as a function

of height $C(y)$ (**Figure 3.6 (a)**). For the free-standing membrane, the midpoint of the bottom edge of the active layer was fixed, and the moisture concentration in the active layer was also defined as $C(y)$ (**Figure 3.6 (b)**).

The oscillatory motion of SNA membranes under a gradient humidity field was simulated using the Solid Mechanics and Transport of Diluted Species modules in COMSOL Multiphysics. The SNA membrane was modeled as an elastic and continuous cantilever. A moisture gradient of $g_{\mathrm{C}} = 2.08\ \mathrm{mol/m^4}$ was implemented by specifying constant moisture concentrations at the bottom (1 mol/m^3) and top surfaces (0.75 mol/m^3) of the simulation box (20 cm wide $\times$ 12 cm high, as shown in **Figure 3.6 (c)**).

The mechanical and physical properties of the membranes used in all models were taken from the experimental results: the Young's modulus was set to 1.2 GPa for the MXene/NP membrane and 4.24 GPa for the GO/SA membrane. The hygroscopic expansion coefficient β was taken as 0.036 m^3/mol for MXene/NP, and 0.0116 m^3/mol for GO/SA. The diffusivity of water was taken as 0.091 mm^2/s for MXene/NP and 0.08 mm^2/s for GO/SA, and the diffusivity of water in air was taken as 1 mm^2/s based on the standard humidity-air data [150]. Poisson's ratios were assumed as 0.3 for both membranes.

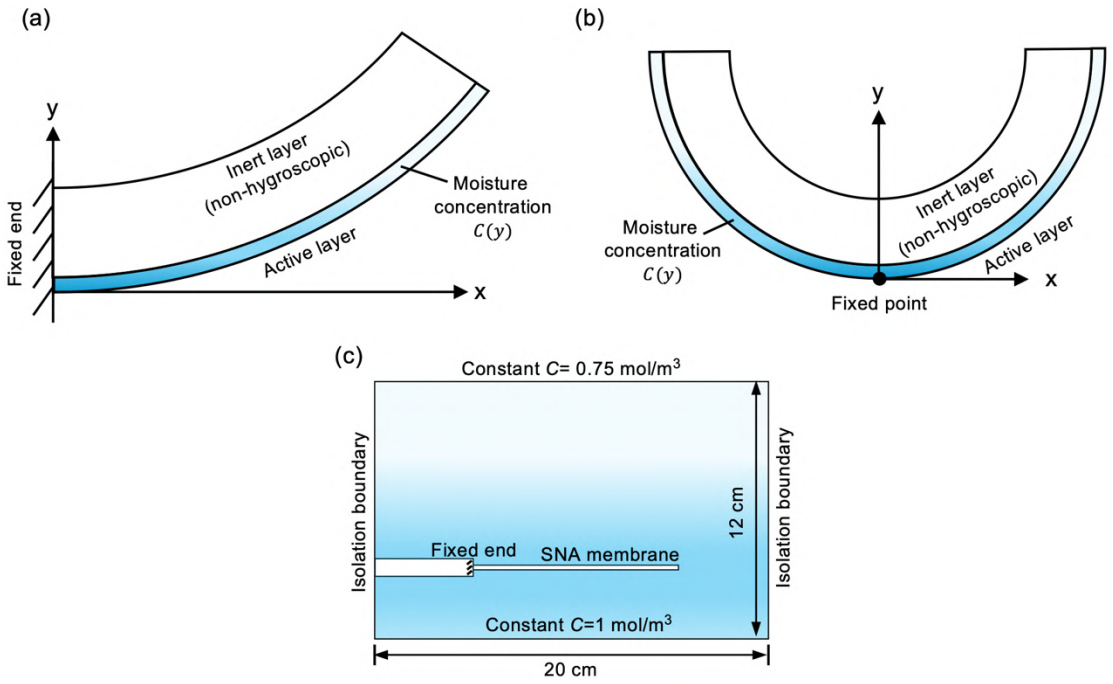

Figure 3.6 Schematic illustration of the boundary and initial condition of the (a) cantilevered membrane and (b) free-standing membrane in the FEM model. (c) Schematic illustration of the boundary and initial condition of the spatial gradient moisture distribution in the FEM model.

Chapter 4. Deformative response of bilayer membranes to moisture stimuli

Bilayer structures are the most common natural structures capable of deforming in response to humidity changes. They have been observed in the microstructural characterization of plants such as pinecones and oat awns. Moreover, as one of the most widely adopted designs in stimuli-responsive thin films, the bilayer structure is not only employed in hygroscopic membranes but also extensively applied in membranes responsive to thermal, electrical, optical, and chemical stimuli. For instance, a bilayer composed of graphene and polyethylene (PE) films exhibits bending deformation under thermal stimulation [42]. Furthermore, by introducing constrained heating to modulate the residual stress in the film's stress-free state, the direction of deformation in response to temperature changes can be tailored.

Given its broad utility, a systematic understanding of bilayer membrane deformation under arbitrary humidity stimuli is essential. Most existing studies attribute deformation behavior solely to strain mismatch between the active and inert layers upon stimulation, lacking in-depth theoretical analysis. In our earlier analysis of the fundamental mechanics of bilayer membranes, only on the deformation of freestanding membranes under uniform moisture stimuli was illustrated. Meanwhile, more complex boundary conditions—such as cantilevered membranes with one end fixed or membranes exposed to non-uniform humidity gradients—introduce additional mechanical investigations that demand thorough investigation.

In this chapter, a theoretical model to calculate the deformative response of bilayer hygroscopic membranes under spatially non-uniform humidity fields is developed, including the derivation of analytical solutions for their bending configurations. Subsequently, a finite element method is employed to simulate the deformation of cantilevered and free-standing membranes under humid environments generated by hot water baths and linearly distributed vapor fields. The reliability of the analytical solution will be validated by comparing it with numerical solutions and experimental results.

4.1 Theoretical modelling

Theoretical modeling is carried out to predict the bending curvature of the cantilevered bilayer membranes, as schematically shown in **Figure 4.1**. The bilayer membranes contain two layers: an ultra-thin active layer with thickness h_{ac} and the coefficient of hygroscopic expansion β and an inert layer with thickness h_{in} and zero hygroscopic expansion coefficient ($h_{\mathrm{ac}} \ll h_{\mathrm{in}}$). Here both layers are assumed elastic, and the corresponding Young's moduli and Poisson's ratios are: $E_{\mathrm{in}}, v_{\mathrm{in}}, E_{\mathrm{ac}}, v_{\mathrm{ac}}$, respectively.

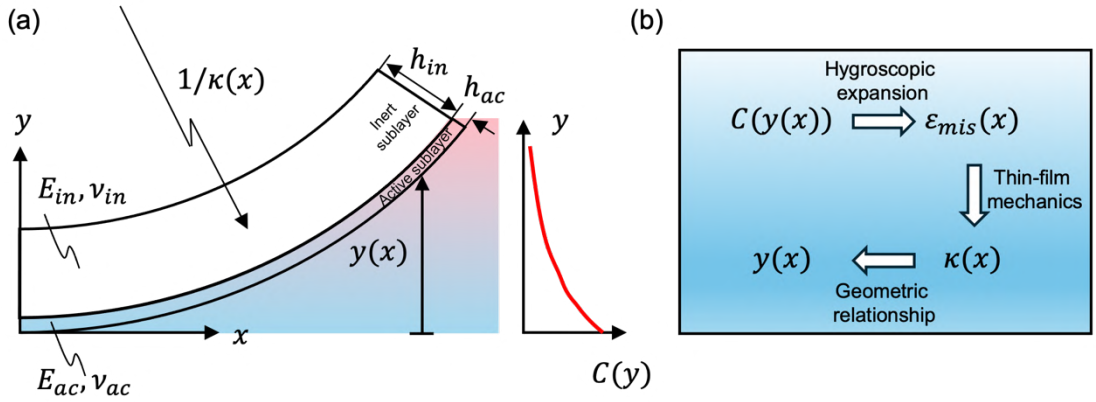

Figure 4.1 Schematic illustration of the (a) bilayer structure, (b) theoretical modelling.

The strain (x-direction) mismatch between the active layer and inert layer is (plane stress assumption):

$$\varepsilon_{\text{mis}} = \beta_{\text{h}}(C(y(x)) - C_{\text{ref}}) \tag{4.1}$$

where β_h is the coefficient of hygroscopic swelling of active layer with units of m^3/mol, M_m is the molar mass (0.018 kg/mol for water), $C(y(x))$ is the concentration of moisture in units of mol/m^3, which is related to the vertical height $y(x)$, C_{ref} is the strain-free reference concentration, ν_{ac} is the Poisson's ratio of the active layer.

The free-body diagram of a representative segment for both layers is shown in **Figure 4.2**. Due to the strain mismatch, there is a shear stress $\tau(x)$ distributed in the interface.

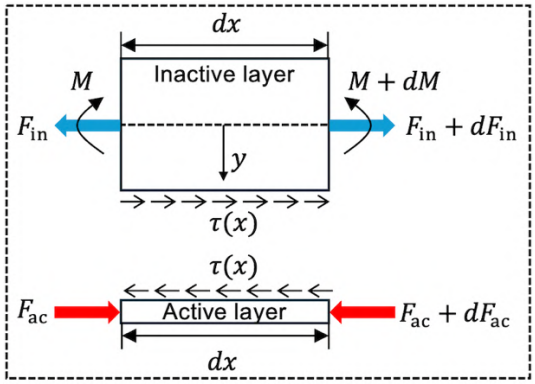

Figure 4.2 Free body diagram of the active and inert sublayer.

For the active layer,

$$dF_{\mathrm{ac}} = \tau(x) \cdot dx \tag{4.2}$$

According to Hooke's law (isotropic) [151], the tensile strain is:

$$\varepsilon_x^{\mathrm{ac}}(x) = \frac{1}{E_{\mathrm{ac}}}\left[\sigma_x^{\mathrm{ac}}(x) - v\left(\sigma_y^{\mathrm{ac}}(x) + \sigma_z^{\mathrm{ac}}(x)\right)\right]$$

The normal stress along the *y*-direction within the active sublayer is negligible compared with those along the *x* and *z* directions, i.e., $\sigma_y^{\mathrm{ac}}(x) \approx 0$. The plane strain assumption implies that $\sigma_z^{\mathrm{ac}}(x) = v\sigma_x^{\mathrm{ac}}(x)$. The in-plane strain in active layer therefore can be obtained by $\varepsilon_x^{\mathrm{ac}}(x) = \frac{1-v_{\mathrm{ac}}^2}{E_{\mathrm{ac}}}\sigma_x^{\mathrm{ac}}(x)$. Taking the derivative of both sides gives rise to

$$d[\varepsilon_x^{\mathrm{ac}}(x)] = \frac{1-v_{\mathrm{ac}}^2}{E_{\mathrm{ac}}} d[\sigma_x^{\mathrm{ac}}(x)]$$

$$d[\varepsilon_x^{\mathrm{ac}}(x)] = \frac{1-v_{\mathrm{ac}}^2}{E_{\mathrm{ac}}} \cdot \tau(x) \cdot \frac{dx}{h_{\mathrm{ac}}} \tag{4.3}$$

For the inert layer,

$$d(\sigma_{x-t}^{\mathrm{in}}) = -\tau(x) \cdot \frac{dx}{h_{\mathrm{in}}}, d(\sigma_{x-b}^{\mathrm{in}}) = \frac{12dM}{h_{\mathrm{in}}^3} y = -\frac{6\tau(x) \cdot dx}{h_{\mathrm{in}}^2} y$$

The incremental bending strain caused by $d(\sigma_{x-b}^{\text{in}})$ is:

$$d(\varepsilon_{x-b}^{in}) = \frac{1-v_{\text{in}}^2}{E_{\text{in}}} \cdot d(\sigma_{x-b}^{\text{in}}) = -\frac{1-v_{\text{in}}^2}{E_{\text{in}}} \cdot \frac{6\tau(x)\cdot dx}{h_{\text{in}}^2} y$$

$$d[\kappa(x)] = \frac{d(\varepsilon_{x-b}^{\text{in}})}{y} = -\frac{1-v_{\text{in}}^2}{E_{\text{in}}} \cdot \frac{6\tau(x)\cdot dx}{h_{\text{in}}^2} \quad (4.4)$$

The incremental stress in the inert layer is:

$$d\left[\sigma_x^{\text{in}}(x)\right] = d(\sigma_{x-t}^{\text{in}}) + d(\varepsilon_{x-b}^{\text{in}}) = -\tau(x) \cdot \frac{dx}{h_{\text{in}}} - \frac{6\tau(x)\cdot dx}{h_{\text{in}}^2} y \quad (4.5)$$

At the interface where $y = h_{\text{in}}/2$,

$$d\left[\sigma_x^{\text{in}}(x)\right]_{|y=\frac{h_{\text{in}}}{2}} = -\frac{4dx}{h_{\text{in}}}\tau(x) \quad (4.6)$$

$$d\left[\varepsilon_x^{\text{in}}(x)\right]_{|y=\frac{h_{\text{in}}}{2}} = -\frac{1-v_{\text{in}}^2}{E_{\text{in}}} \cdot \frac{4x}{h_{\text{in}}}\tau(x) \quad (4.7)$$

Since

$$d[\varepsilon_x^{ac}(x)] = \frac{1-v_{ac}^2}{E_{ac}} \cdot \frac{\tau(x)dx}{h_{ac}} \quad (4.8)$$

The continuity condition of strain at the interface is similar to the model above

$$d[\varepsilon_x^{\text{in}}(x)]_{|y=\frac{h_{\text{in}}}{2}} = d[\varepsilon_{\text{mis}}(x)] + d[\varepsilon_x^{\text{ac}}(x)] \quad (4.9)$$

Inserting Eq. (4.7), (4.8) into Eq. (4.9) yields

$$d[\varepsilon_{\text{mis}}(x)] = \left[-\frac{1-v_{\text{ac}}^2}{E_{\text{ac}}h_{\text{ac}}} - \frac{4(1-v_{\text{in}}^2)}{E_{\text{in}}h_{\text{in}}}\right] \cdot \tau(x)dx \quad (4.10)$$

Substitution of Eq. (4.4) into the above equation to eliminate $\tau(x)$ gives

$$d[\varepsilon_{\text{mis}}(x)] = \left[\frac{1-v_{\text{ac}}^2}{E_{\text{ac}}h_{\text{ac}}} + \frac{4\left(1-v_{\text{in}}^2\right)}{E_{\text{in}}h_{\text{in}}}\right] \cdot \frac{d[\kappa(x)]\cdot h_{\text{in}}^2 \cdot E_{\text{in}}}{6\left(1-v_{\text{in}}^2\right)} \quad (4.11)$$

Integrating Eq. (4.11) yields

$$\int_0^x d[\varepsilon_{\mathrm{mis}}(x)] = \left[\frac{1-v_{\mathrm{ac}}^2}{E_{\mathrm{ac}}h_{\mathrm{ac}}} + \frac{4(1-v_{\mathrm{in}}^2)}{E_{\mathrm{in}}h_{\mathrm{in}}}\right] \cdot \frac{h_{\mathrm{in}}^2 \cdot E_{\mathrm{in}}}{6(1-v_{\mathrm{in}}^2)} \int_0^x d[\kappa(x)]$$

$$\varepsilon_{\mathrm{mis}}(x) = \left[\frac{1-v_{\mathrm{ac}}^2}{E_{\mathrm{ac}}h_{\mathrm{ac}}} + \frac{4(1-v_{\mathrm{in}}^2)}{E_{\mathrm{in}}h_{\mathrm{in}}}\right] \cdot \frac{h_{\mathrm{in}}^2 \cdot E_{\mathrm{in}}}{6(1-v_{\mathrm{in}}^2)} \cdot [\kappa(x) - \kappa(0)] + \varepsilon_{\mathrm{mis}}(0) \quad (4.12)$$

For the relationship between $\kappa(0)$ and $\varepsilon_{\mathrm{mis}}(0)$, the free-body diagram of an infinitesimal segment at the beginning point of the bilayer structure is considered, as shown in **Figure 4.3**.

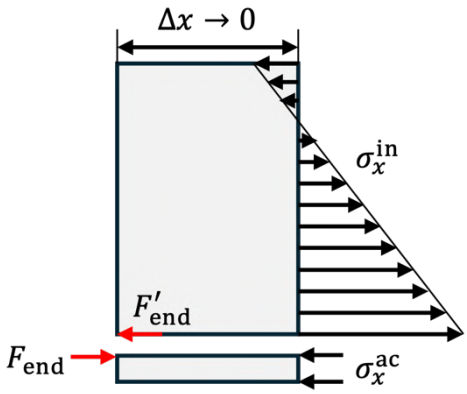

Figure 4.3 Stress diagram in the inert and active layer at $x \to 0$.

As the beginning point of the bilayer membranes is fixed, there is no shear stress at the interface. The relationship between $\kappa(0)$ and $\varepsilon_{\mathrm{mis}}(0)$ can be derived by

$$\varepsilon_{mis}(0) = \left[\frac{1-v_{ac}^2}{E_{ac}} + \frac{1-v_{in}^2}{E_{in}} \cdot \frac{4h_{ac}}{h_{in}}\right] \cdot \frac{h_{in}^2 E_{in}}{6(1-v_{in}^2)h_{ac}} \kappa(0)$$

Substitution the above equation into Eq. (4.12) gives

$$\varepsilon_{\mathrm{mis}}(x) = \left[\frac{1-v_{\mathrm{ac}}^2}{E_{\mathrm{ac}}h_{\mathrm{ac}}} + \frac{4(1-v_{\mathrm{in}}^2)}{E_{\mathrm{in}}h_{\mathrm{in}}}\right] \cdot \frac{h_{\mathrm{in}}^2 \cdot E_{\mathrm{in}}}{6(1-v_{\mathrm{in}}^2)} \cdot \kappa(x) \quad (4.13)$$

Inserting Eq. (4.1) into Eq. (4.13) yields

$$\kappa(x) = \frac{\beta_{\mathrm{h}}(C(y(x)) - C_{\mathrm{ref}})}{\left[\frac{1-v_{\mathrm{ac}}^2}{E_{\mathrm{ac}}h_{\mathrm{ac}}} + \frac{4(1-v_{\mathrm{in}}^2)}{E_{\mathrm{in}}h_{\mathrm{in}}}\right] \cdot \frac{h_{\mathrm{in}}^2 \cdot E_{\mathrm{in}}}{6(1-v_{\mathrm{in}}^2)}} \quad (4.14)$$

As indicated by Eq. (4.14), the deformation configuration of a cantilevered bilayer hygroscopic membrane can be analytically predicted, provided that the material properties of both the active and passive layers, along with the humidity gradient across the membrane thickness, are known.

The boundary condition for the bilayer membrane is: $y(0) = y'(0) = 0$, as the membrane is cantilevered with one end ($x = 0$) fixed. On the other hand, since $\kappa(x) = \frac{y''(x)}{[1+y'^2(x)]^{1.5}}$, it can be obtained that $y''(0) = \kappa(0)$.

The geometric relationship between the curvature $\kappa(x)$ and the bending deformation profile $y(x)$ of the membrane can be derived by analyzing a differential element of the bending membrane. As illustrated in the **Figure 4.4**, the endpoints of the element are denoted as $y(x_i)$ and $y(x_{i+1})$. Within this element, the arc length of the membrane is approximately equal to the element length Δx. The angles between the normals at the two endpoints and the y-axis are θ and θ_1, respectively. Accordingly, it follows that $\theta_1 = \theta + \frac{\Delta x}{\kappa(x)}$, and the displacement of the upper point can be expressed as $y(x_{i+1}) = y(x_i) + \frac{[\cos(\theta)-\cos(\theta_1)]}{\kappa(x)}$. Since the membrane may undergo large deformation during bending, it is necessary to recalculate the x-coordinate of the right endpoint $x_{i+1} = x_i + \frac{\sin(\theta_1)-\sin(\theta)}{\kappa(x)}$.

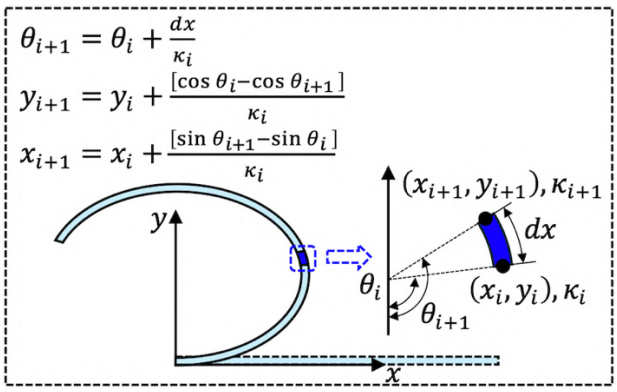

Figure 4.4 Schematic illustration of the geometric relationship between $\kappa(x)$ and $y(x)$.

4.2 Deformative response of cantilevered membranes

Since the theoretical model is based on a bilayer hygroscopic membrane with a cantilever beam configuration, the conclusions derived from the above analysis can be directly applied in this chapter. For experimental validation, a bilayer hygroscopic membrane composed of PVC (adhesive tape, serving as the inert layer) and MXene (active layer) will be used. The PVC layer has a Young's modulus of 5.37 GPa, a thickness of 50 μm, and a Poisson's ratio of 0.4. The mechanical properties of the MXene layer have been characterized in Chapter 3, with a Young's modulus of 1 GPa, a thickness of 10 μm, and an assumed Poisson's ratio of 0.3. As for the hygroscopic expansion coefficient (HEC), PVC is a non-hygroscopic material ($\beta_{\mathrm{PVC}} = 0$), and the HEC for MXene is 0.0358 m^3/mol. Meanwhile, the reference moisture concentration is 0.6 mol/m^3. In this chapter, the deformation response of the bilayer hygroscopic membrane with a cantilever structure will be investigated under uniform humidity and humidity gradients (including both linear gradients and those generated above a 40 °C

water surface).

4.2.1 Deformative response in uniform humidity

Experimental results

The aforementioned bilayer hygroscopic membrane with a total length of 2 cm was placed in an environmental chamber, where the temperature was maintained at room temperature (25 °C) and the reference relative humidity was set to 60%. Under these conditions, no noticeable bending deformation was observed. However, when the humidity was increased to 90%, the bilayer membrane exhibited significant bending deformation. Upon further increase in humidity, no additional deformation occurred, as the MXene layer had reached saturation and could no longer absorb additional moisture (**Figure 4.5**).

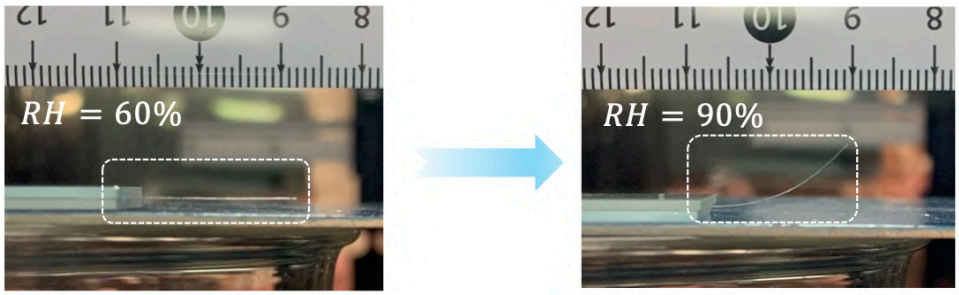

Figure 4.5 Deformative response of cantilevered bilayer hygroscopic membranes to uniform humidity.

Theoretical results

Based on the theoretical model and the geometric relationships described above, the deformation configuration $y(x)$ of the bilayer hygroscopic membrane can be

obtained by solving Eq. (4.14), giving a uniform moisture concentration $c\big(y(x)\big) = 0.3$ at any point (x, y). The resulting configuration $y(x)$ is shown in **Figure 4.6**.

FEM simulation

Numerical simulation based on the finite element method (FEM) was also conducted to validate the analytical solution. The physical parameters of the active and inert layers—such as Young's modulus and hygroscopic expansion coefficient—were obtained from experimental measurements (Chapter 3). The left end of the bilayer membrane was fixed, and the water concentration in the active layer was set to 0.9 mol/m^3. It is worth noting that geometric nonlinearity was introduced in the simulation to account for large deformations, and the result is shown in **Figure 4.6.**

Validation of the analytical solution

The experimental and numerical simulation results were used to validate the reliability of our theoretical model. As shown in **Figure 4.6**, the theoretical predictions exhibit excellent agreement with the numerical simulation and experimental results. The overall agreement confirms the reliability of the proposed theoretical model.

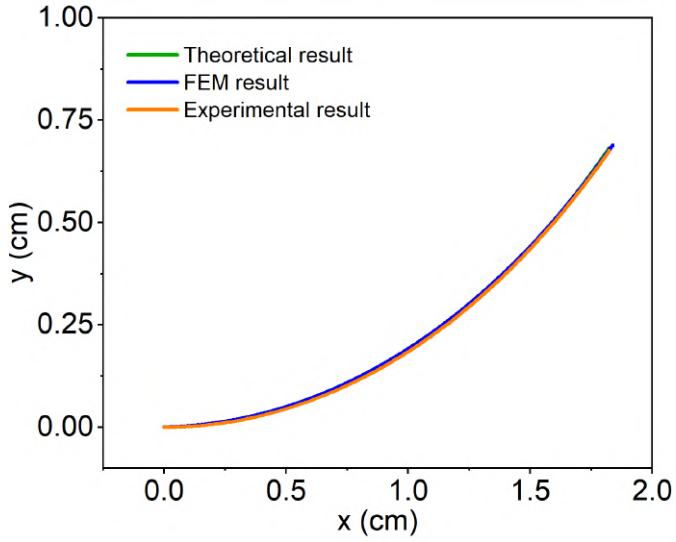

Figure 4.6 Comparison between the theoretical, numerical, and experimental results of the bending configuration of bilayer hygroscopic membrane in uniform humidity.

4.2.2 Deformative response in a humidity field above a hot water bath

The moisture gradient above the surface of a 40 °C water bath was measured using the method described in Chapter 3 (**Figure 4.7**). A piece of glass and a pre-bent hygroscopic membrane were placed above the water surface to enable accurate measurement of the humidity gradient during membrane deformation. The bilayer membrane used here also consists of PVC (inert layer) and MXene (active layer), with a length of 4 cm.

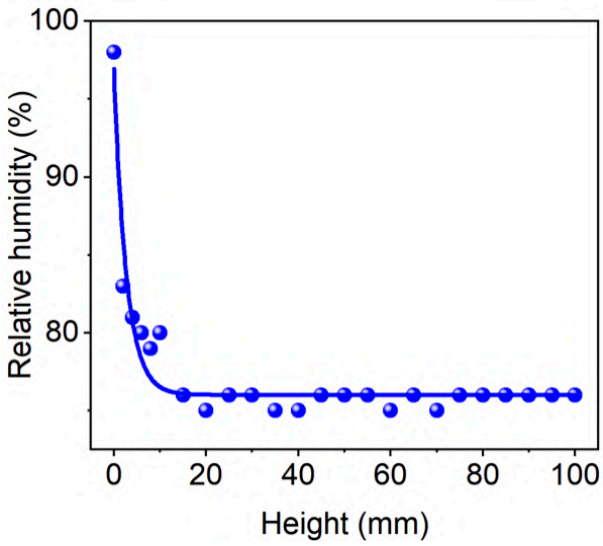

Figure 4.7 Moisture gradient above the surface of a 40 °C water bath with a cantilevered membrane.

Experimental results

The bilayer hygroscopic membrane was placed above the surface of the 40 °C water bath and exhibited significant bending deformation, as shown in **Figure 4.8**.

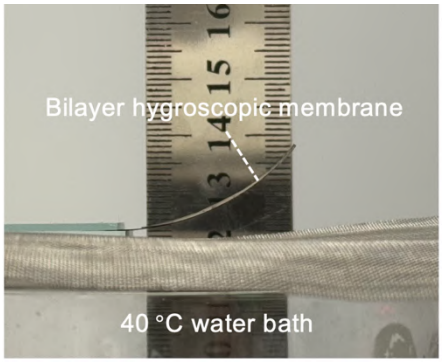

Figure 4.8 Bending deformation of bilayer hygroscopic membrane above the surface of the 40 °C water bath.

Theoretical results

The moisture gradient distribution $C(y)$ obtained in **Figure 4.7** was directly

incorporated into the theoretical model. By applying the corresponding geometric relationships, the theoretical deformation profile of the bilayer hygroscopic membrane under the gradient humidity field was determined, as shown in **Figure 4.9**.

FEM simulation

The finite element simulation results are presented in the **Figure 4.9**, using the same boundary conditions as previously defined.

Validation of the analytical solution

As shown in **Figure 4.9**, the deformation configurations derived from experimental observation, finite element simulation, and theoretical model are in close agreement. Nonetheless, the experimental profile is slightly lower, likely due to the influence of gravity, which was not considered in the theoretical or numerical models.

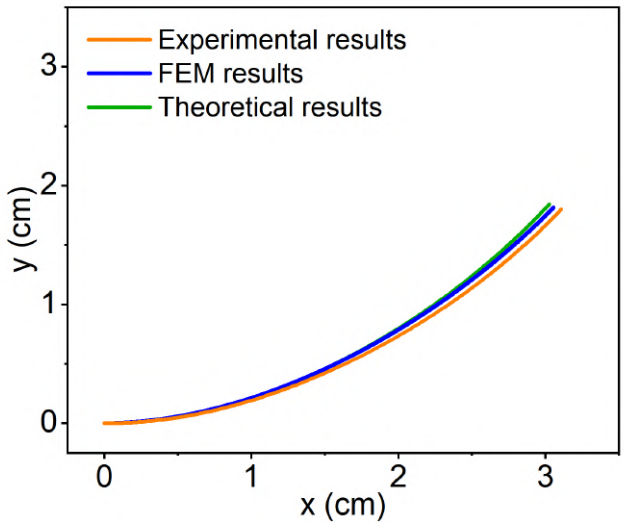

Figure 4.9 Comparison between the theoretical, numerical, and experimental results of the bending configuration of bilayer hygroscopic membrane in a gradient moisture generated by a 40 °C water bath.

4.2.3 Deformative response in a humidity field with a linear gradient

In this section, the deformation of a cantilevered bilayer membrane under a linear humidity gradient field is investigated. The linear distribution of humidity along the height is illustrated in **Figure 4.10**. It is assumed that the highest humidity is 90% at the base (height = 0), and it decreases linearly to 60%—matching ambient humidity—at the top, where the height equals the film length. Since such a linear humidity gradient is difficult to reproduce experimentally, only the results from the theoretical model and finite element simulations are discussed here.

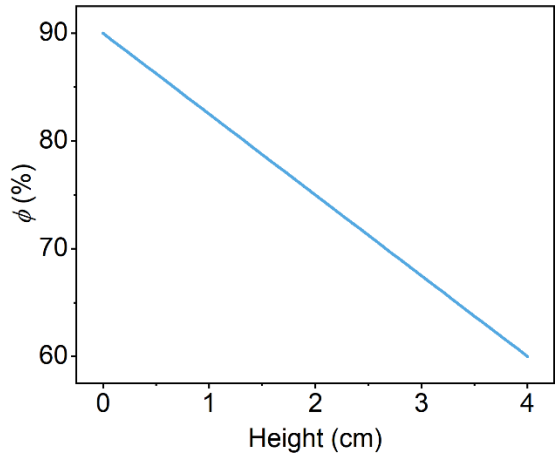

Figure 4.10 Linear moisture gradient distribution.

Under the linear humidity gradient, the results obtained from the theoretical model and finite element simulations also exhibit a high degree of consistency (**Figure 4.11**). However, a small discrepancy remains, which is likely attributed to the different methods adopted by the theoretical model and the finite element method in accounting for large deformations.

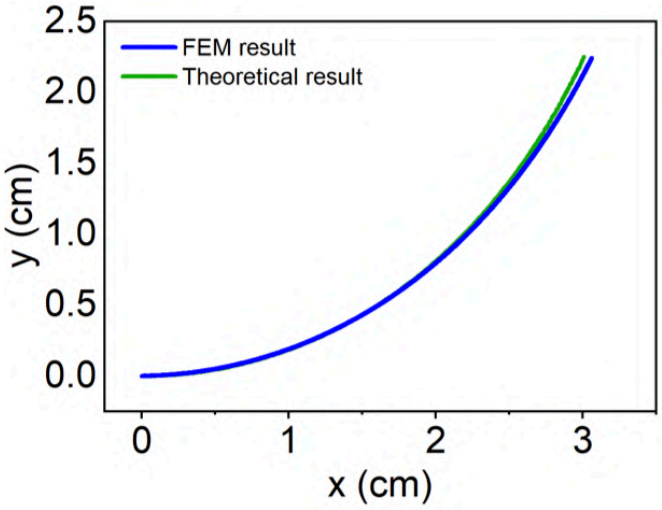

Figure 4.11 Comparison of FEM result and theoretical result of the bending configuration of bilayer hygroscopic membrane in a linear humidity gradient.

4.3 Deformative response of free-standing membranes

For the theoretical modeling of free-standing hygroscopic membranes, it is only necessary to modify the cantilever beam model to be symmetric about $x = 0$. In addition, since the free-standing membrane model adopts free boundary conditions, the stability of its deformed configuration is also of great importance. Therefore, the centroid of the deformed membrane will be calculated. Furthermore, the trajectory of the centroid when the deformed membrane rolls will be used to determine whether the membrane is in a stable state at that moment: as the membrane maintains point contact with the substrate after deformation, it is only in a stable state when the center of mass reaches its lowest position.

4.3.1 Deformative response in uniform humidity

The deformation of the free-stranding bilayer hygroscopic membrane in a uniform

humidity field (RH=90%) is shown in **Figure 4.12 (a)**. Its deformation configuration agrees well with both the theoretical model and the finite element results, further confirming their reliability (**Figure 4.12 (b)**). In the following, the stability of this deformation configuration will be analyzed.

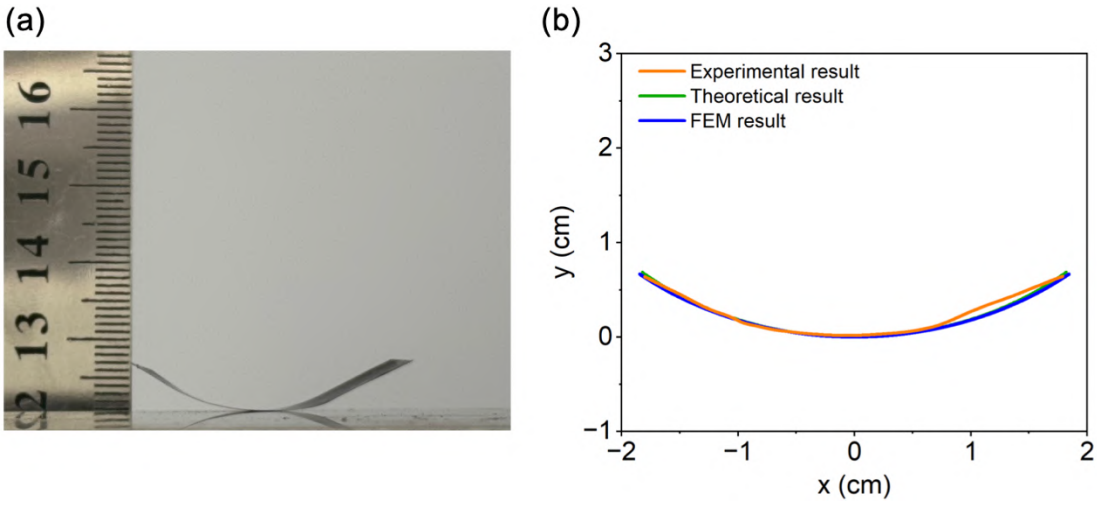

Figure 4.12 (a) Deformation configuration of bilayer hygroscopic membrane in a uniform humidity field. (b) Comparison between the experimental, theoretical, and FEM results of the deformation configuration.

Stability

As discussed above, for a free-standing bilayer hygroscopic membrane, the post-deformation stability can be evaluated by tracking the centroid trajectory during rolling. In the case of a uniform humidity field, the mismatch stress within the bilayer is constant. According to Eq. (4.14), this leads to a constant curvature of the deformed membrane, resulting in a configuration that forms an arc segment with a fixed radius. For such a standard arc, the initial configuration—symmetric about $x = 0$—is inherently stable. This is confirmed by the centroid trajectory during leftward rolling,

where the initial position always corresponds to the lowest point (**Figure 4.13**).

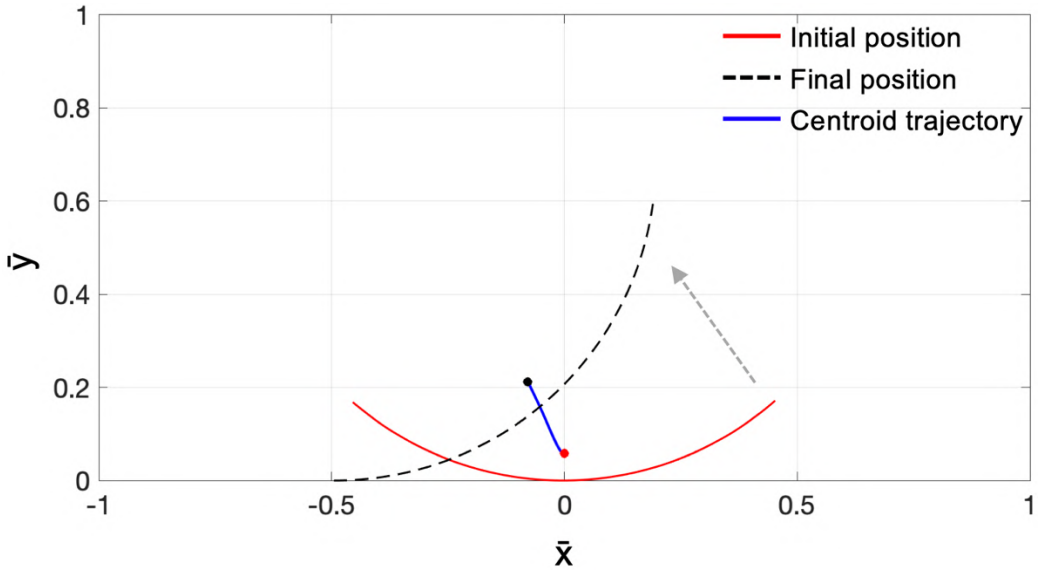

Figure 4.13 Theoretical modelling showing the rolling of the deformed bilayer membrane from the initial position to the final position in a uniform humidity field, and the centroid trajectory during this process.

4.3.2 Deformative response in humidity field above a hot water bath

For the humidity field above a water-bath surface, the deformation of the bilayer hygroscopic membrane can still be predicted using both the theoretical model and finite element simulations, as shown in **Figure 4.14**. The discrepancies among the experimental results, the theoretical model, and the finite element simulations may originate from errors in fitting the humidity gradient profile at the water bath surface.

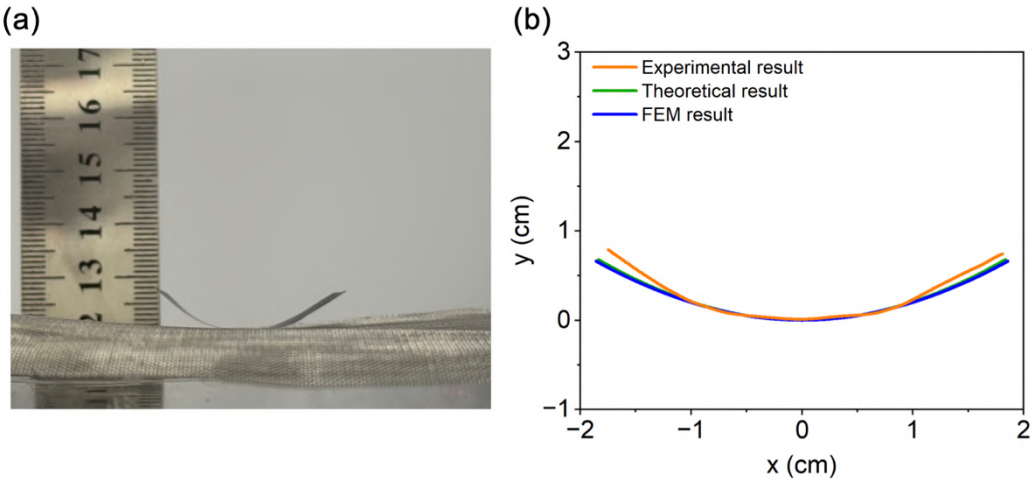

Figure 4.14 (a) Deformation configuration of bilayer hygroscopic membrane in a humidity field above a water-bath surface. (b) Comparison between the experimental, theoretical, and FEM results of the deformation configuration of the bilayer membrane in a humidity field above a hot water bath.

Stability

However, the stability analysis in this case differs from that under a uniform humidity field. This is because the humidity above the water-bath surface decreases with height, which implies that the mismatch strain in the bilayer also decreases. According to Eq. (4.14), this results in a reduced curvature along the height of the membrane. This non-uniform curvature makes the stability analysis more complex. For the PVC/MXene bilayer considered here, the overall variation in curvature is relatively small, and the membrane remains in a stable configuration under this humidity field (**Figure 4.15**).

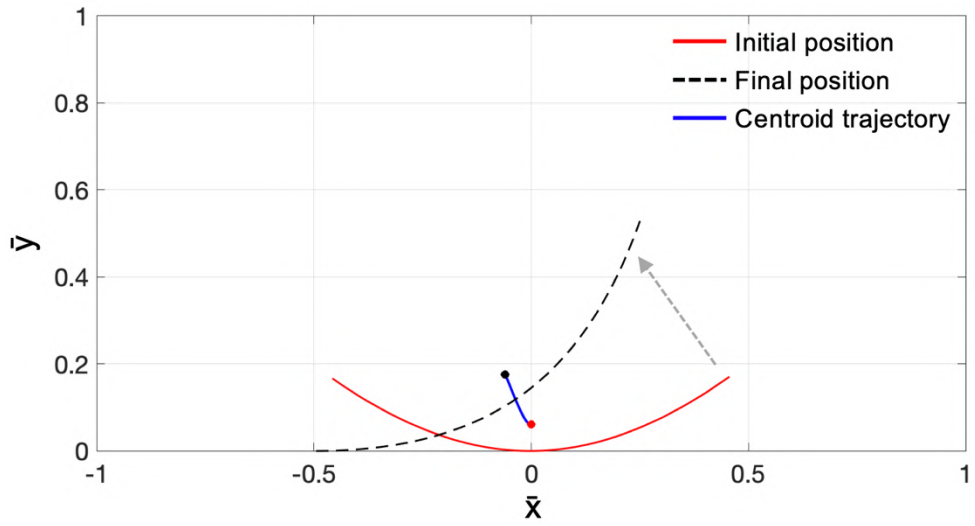

Figure 4.15 Theoretical modelling showing the rolling of the deformed bilayer membrane from initial position to final position in a humidity field above a water-bath surface, and the centroid trajectory during this process.

For the bilayer membrane, assuming that the thicknesses of the active and inert layers remain constant (10 μm and 50 μm, respectively) and that the physical properties of the active layer (Young's modulus and hygroscopic expansion coefficient) remain unchanged, Eq. (4.14) gives the relationship between the bending curvature of the membrane and the mismatch strain as:

$$\kappa(x) = \frac{\varepsilon_{\mathrm{mis}}(x)}{4.5\times10^{-5}\times\left(\frac{E_{\mathrm{in}}}{E_{\mathrm{ac}}}+0.74\right)} \tag{4.15}$$

According to Eq. (4.15), the coefficient relating curvature to mismatch strain increases with the reduction in stiffness of the inert layer. It can be anticipated that when E_{in} decreases below a certain threshold, the curvature of the membrane during bending will increase progressively with decreasing height, and the stability of the free-standing membrane under humidity stimulation will be reduced. For example, when the modulus

of the inert layer drops to 0.5 GPa, the lowest point of the centroid is no longer located at its initial state (**Figures 4.16 (a), (b)**), but rather at an intermediate configuration (**Figure 4.16 (c)**). In this case, the deformed membrane will spontaneously roll until its centroid reaches the lowest point.

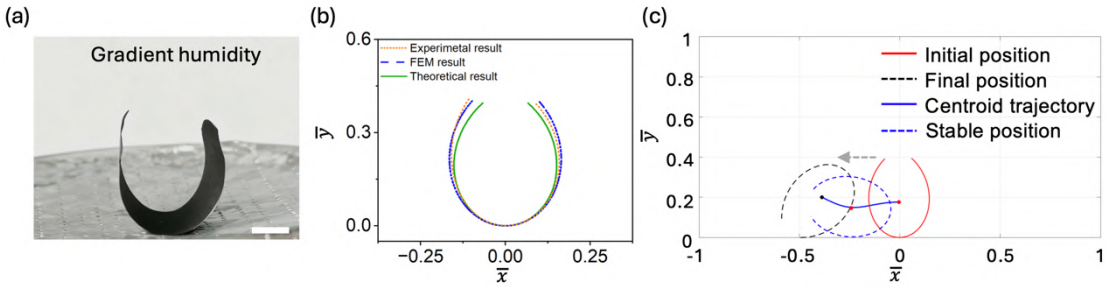

Figure 4.16 (a) Experimental observation of the bending configuration of free-standing membrane in gradient humidity. (b) Comparison between the experimental, theoretical, and FEM result of the deformation configuration of bilayer membrane in a humidity field above a water-bath surface. (c) Theoretical modelling showing the rolling of the deformed bilayer membrane from the initial position to the final position in a humidity field above a water-bath surface, and the centroid trajectory during this process.

4.3.3 Deformative response in a humidity field with a linear gradient

The distribution of the linear gradient humidity field is the same as **Figure. 4.10**. Since it is not feasible to reproduce such a humidity gradient in experiments, only the theoretical model and finite element model results are analyzed here. Similar to the humidity field above the water bath surface, the linear humidity gradient also decreases with height. Therefore, the deformation profile of the bilayer free-standing hygroscopic membrane in this humidity field is similar to that in the water bath surface humidity field, as shown in **Figure 4.17 (a)**. When the physical properties of the bilayer

membrane are the same as those of PVC and MXene, the initial position is the most stable state (**Figure 4.17 (b)**).

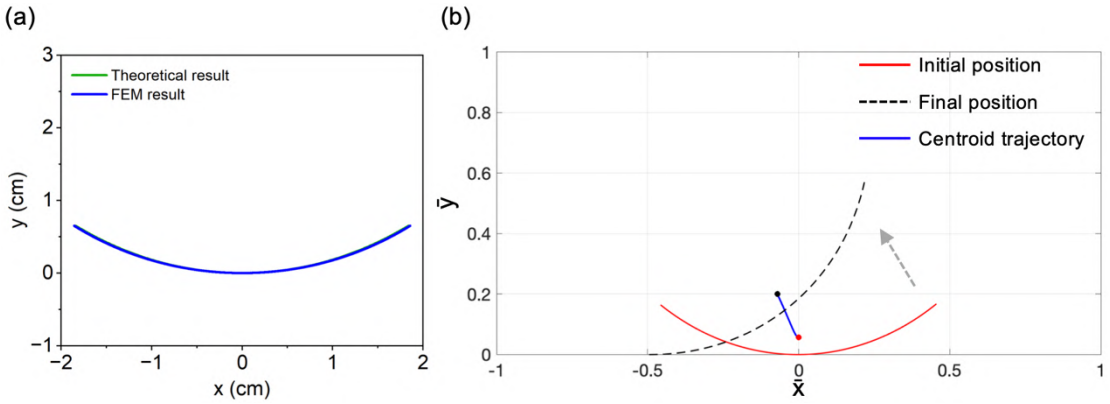

Figure 4.17 (a) Comparison between the theoretical and FEM result of the deformation configuration of bilayer membrane in a linear-gradient humidity field. (b) Theoretical modelling showing the rolling of the deformed bilayer membrane from the initial position to the final position in a linear-gradient humidity field, and the centroid trajectory during this process.

Similar to the case of the humidity field above the water bath surface, according to Eq. (4.15), the stability of the free-standing membrane in a linear gradient humidity field decreases as the stiffness of the inert layer decreases. For example, when the Young's modulus of the inert layer is reduced to 0.5 GPa, the initial state becomes unstable (**Figure 4.18**).

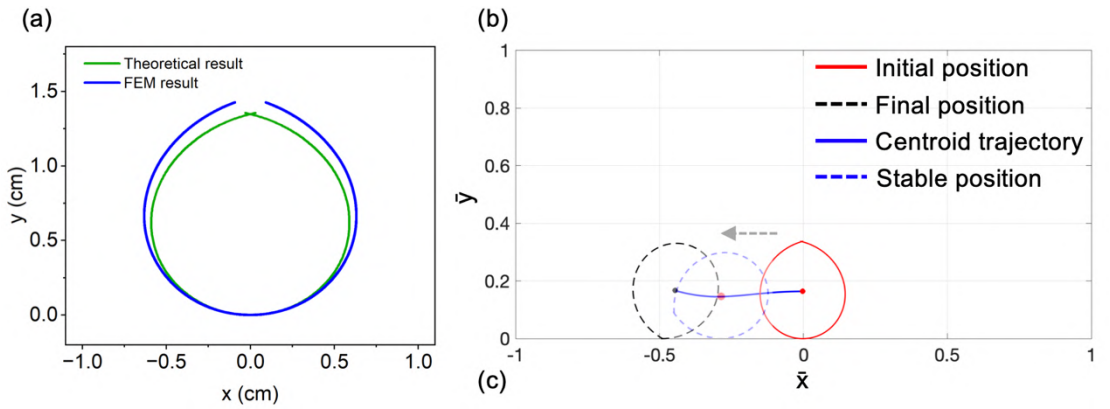

Figure 4.18 (a) Comparison between the theoretical and FEM result of the deformation configuration of bilayer membrane in a linear-gradient humidity field. (b) Theoretical modelling showing the rolling of the deformed bilayer membrane from the initial position to the final position in a linear-gradient humidity field, and the centroid trajectory during this process.

4.4 Summary

In this chapter, the deformative responses of bilayer hygroscopic membranes under different humidity fields were systematically investigated. The discussion focuses on bilayer hygroscopic membranes composed of PVC (inert layer) and MXene (active layer), whose deformation behaviors under uniform humidity and the humidity field at the surface of a 40°C water bath can be accurately predicted by theoretical models and finite element analysis.

For cantilever boundary conditions, since one end of the membrane is fixed, the resulting deformation response is always a steady-state configuration. In contrast, for free-standing membranes, the stability of the deformation response depends on the external humidity field and the modulus of the inert layer. Under uniform humidity, the

membrane adopts a standard circular arc shape with constant curvature, indicating a stable state. However, under the humidity gradient at the surface of the hot water bath, when the inert layer has a high stiffness, the deformed membrane remains stable; whereas with a lower stiffness of the inert layer, the membrane deforms to an unstable state and spontaneously moves toward a more stable configuration. These findings enable the prediction and control of the deformation responses of bilayer hygroscopic membranes under varying humidity fields, thereby enhancing their application potential in humidity sensors and soft actuators.

Nevertheless, the findings of this chapter have certain limitations. First, the theoretical model for bilayer hygroscopic membranes is applicable only when the thickness of the active layer is much smaller than that of the inert layer, assuming uniform stress distribution across the active layer's cross-section. When the two layers have comparable thicknesses, the stress within the active layer varies with thickness, rendering the model invalid. Second, although large deformations have been incorporated into the model, excessive membrane curvature can lead to significant errors in the geometric approximations used. Finally, the model assumes that both the active and inert layers behave as continuous media; it becomes inapplicable when excessive strain induces cracking in either layer or when interfacial strength is insufficient, as interfacial failure is not considered.

Chapter 5. Moisture-driven oscillation of monolayer hygroscopic membranes

The escalating environmental pollution and ecological deterioration driven by excessive fossil fuel consumption highlight the pressing demand for sustainable energy harvesting from ambient sources [110, 152]. Traditional technologies predominantly harness the motion of natural media—such as wind, flowing water, and tides—to actuate mechanical rotors [100, 117, 153], converting the kinetic energy into electricity via electromagnetic induction. Although efficient in large-scale power generation, these systems are inherently large, heavy, and designed for high output, which restricts their integration with distributed microelectronics, flexible devices, and Internet of Things (IoT) systems [154].

Stimuli-responsive materials have emerged as an attractive alternative, capable of transforming diverse environmental inputs—including light [155, 156], electric fields [157-159], thermal gradients [42, 160], and humidity [45, 161]—into mechanical deformation. Nevertheless, under constant stimuli, their actuation is generally unidirectional and irreversible, posing challenges for applications that require continuous reciprocating motion [128, 139]. This limitation has been a major barrier to realizing energy harvesters based on dynamic deformation in ambient environments. A significant advance has been achieved with membranes fabricated via stacked nanoflake assembly (SNA) of two-dimensional materials, such as titanium carbide (MXene) and graphene oxide (GO). These membranes can maintain persistent

oscillatory motion under steady water vapor flows [35, 94], enabling continuous propulsion and direct energy conversion from ambient humidity [39, 62, 162-164].

Despite this progress, the fundamental mechanism governing such autonomous oscillatory behavior remains insufficiently understood. Previous studies have attributed the bending deformation of SNA membranes to gradient strain induced by d-spacing expansion between nanoflakes during water absorption [62, 165], but this view underestimates the dominant role of in-plane expansion relative to the out-of-plane component in determining membrane bending [105]. Moreover, most research emphasizes moisture gradients as the primary driving force [166], while neglecting the significant influence of intrinsic structural and physical properties on oscillatory characteristics. This incomplete mechanistic framework has constrained the rational design and performance optimization of SNA membranes for advanced applications, including microscale propulsion and high-efficiency nanogenerators.

In this chapter, two representative hygroscopic SNA membranes (MXene- and GO-based) were systematically examined to elucidate the underlying mechanism of humidity-driven autonomous oscillation. The findings reveal that the oscillatory behavior originates from the synchronized coupling of two dynamic physical processes: (1) water transport across the membrane thickness driven by environmental humidity gradients, and (2) reversible in-plane expansion/contraction induced by water absorption/desorption. Through the integration of dimensional analysis and numerical simulations, three critical dimensionless parameters were identified, and their effects

on oscillation characteristics were quantitatively determined.

5.1 Experimental investigation of the oscillation

Three types of SNA membranes made of different material systems, including plain MXene, MXene doped with Fe_3O_4 nanoparticles (MXene/NP), and graphene oxide/sodium alginate (GO/SA) were prepared (as previously mentioned in Chapter 3.1) and cantilevered at the same altitude above a hot water bath (40°C). Both MXene/NP and GO/SA membranes exhibited sustained oscillatory motions with frequencies of approximately 0.5–0.6 Hz, whereas the plain MXene membrane displayed only a static bending configuration (**Figure 5.1**).

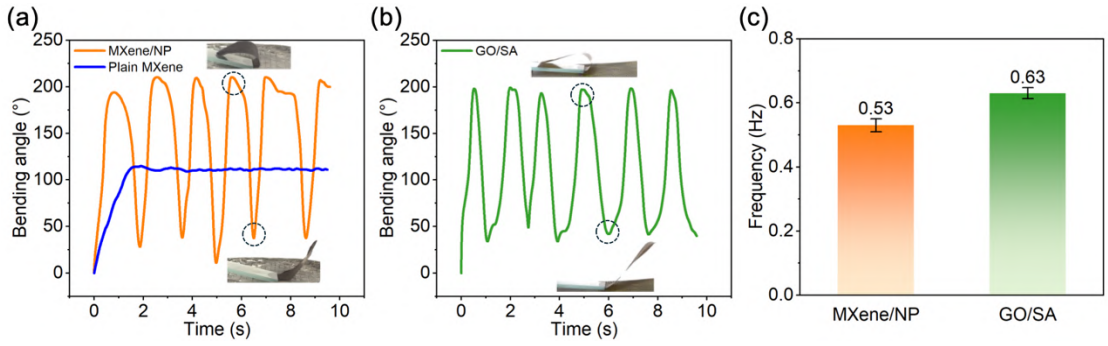

Figure 5.1 Moisture-driven oscillatory behavior of SNA membranes. (a) Bending angle-time curve of the MXene/NP and plain MXene membranes. (b) Bending angle-time curve of the GO/SA membrane. (c) Oscillating frequencies of MXene/NP and GO/SA membranes.

The distinct oscillation behaviors of the MXene/NP, GO/SA, and plain MXene membranes under the same humidity field arise from their differing physical properties, including water diffusivity, Young's modulus, and hygroscopic swelling coefficient (**Figures 5.2(a), (b),** and **(c)**). The distinct responses of MXene/NP and plain MXene

membranes under identical humidity stimuli are attributed to modifications in the physical properties induced by nanoparticle incorporation. Subsequent analyses confirmed that introducing nanoparticles into the MXene membrane retards through-thickness water transport while simultaneously altering the in-plane hygroscopic expansion (**Figures 5.2 (b), (c)**). A dopant concentration of 1.5 wt% was identified as producing the maximum hygroscopic expansion (**Figure 5.2 (d)**) and was therefore adopted in all subsequent MXene/NP membrane preparations.

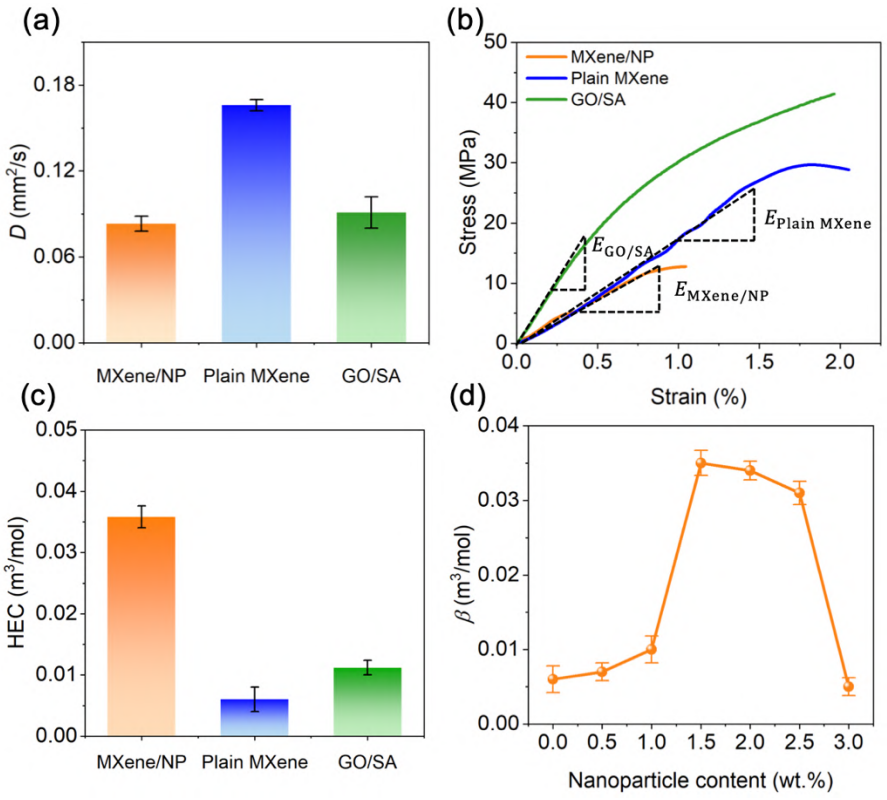

Figure 5.2 (a) The measured diffusivities of MXene/NP, plain MXene, and GO/SA membranes. (b) Stress-strain curve of MXene/NP, plain MXene, and GO/SA membranes. (c) The measured hygroscopic expansion coefficient (HEC) of MXene/NP, plain MXene, and GO/SA membranes. (d) Variation of the hygroscopic expansion coefficient (HEC) of MXene/NP membranes with the concentration of doped nanoparticle (Fe_3O_4).

To elucidate the key factors influencing oscillatory motion, the effect of membrane orientation was first examined by rotating the oscillating MXene/NP and GO/SA membranes from a horizontal to a vertical configuration (**Figure 5.3 (a)**). In both cases, oscillation ceased immediately, indicating that a through-thickness humidity gradient is essential for sustaining motion. The presence of such a gradient above the hot water bath was experimentally confirmed (**Figure 5.3 (b)**).

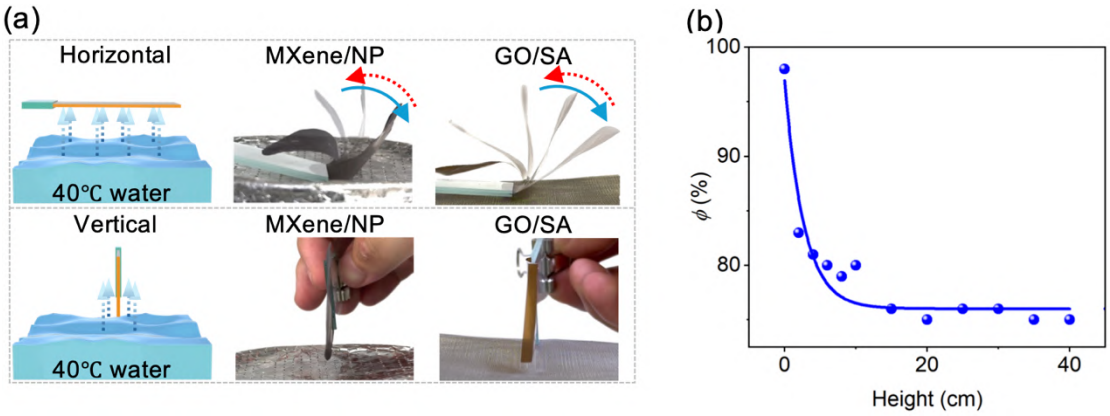

Figure 5.3 (a) Responses of SNA membranes at horizontal and vertical gestures to the same water vapor flow. (b) Humidity distribution along the height of a 40°C water-bath surface.

The robustness of the oscillatory behavior was further assessed by mechanically arresting the motion of the membranes through clamping. Upon release, both MXene/NP and GO/SA membranes resumed oscillations almost instantaneously (**Figure 5.4**), demonstrating that the moisture-driven excitation mechanism provides a persistent driving force capable of sustaining autonomous motion even after transient mechanical interruptions.

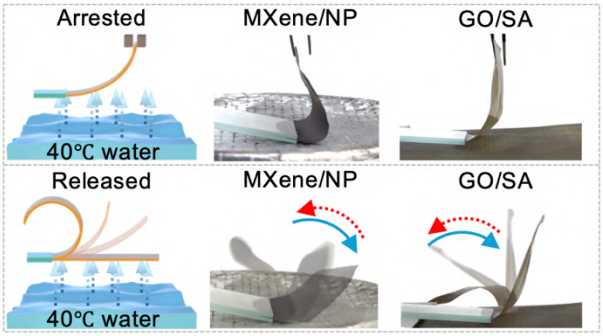

Figure 5.4 Responses of SNA membranes to a temporary arrest.

The observed oscillations are clearly distinct from thermally induced vibrations [167], as confirmed by the absence of measurable deformation when both membranes were placed on a hot plate at a temperature comparable to that of the water bath (**Figure 5.5**). Vapor flow momentum was also excluded as a possible driving force, since a non-hygroscopic polyethylene membrane—despite being lighter and more flexible than the oscillating SNA membranes—showed no oscillatory response under identical vapor flow conditions.

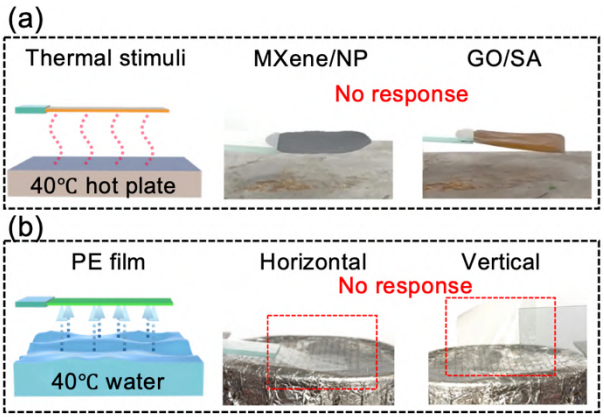

Figure 5.5 (a) Inertness of SNA membranes to thermal stimuli with the same temperature as the water bath. (b) Inertness of PE film (non-hygroscopic, flexible) to water flow momentum.

Collectively, these findings establish that the sustained oscillations of both SNA

membranes result from the synergistic coupling between dynamic, humidity-gradient-driven water transport across the membrane thickness and asymmetric hygroscopic expansion/contraction cycles within the nanoflake assemblies (**Figure 5.6**). This coupled chemo-mechanical mechanism enables the continuous conversion of ambient moisture gradients into persistent mechanical oscillations.

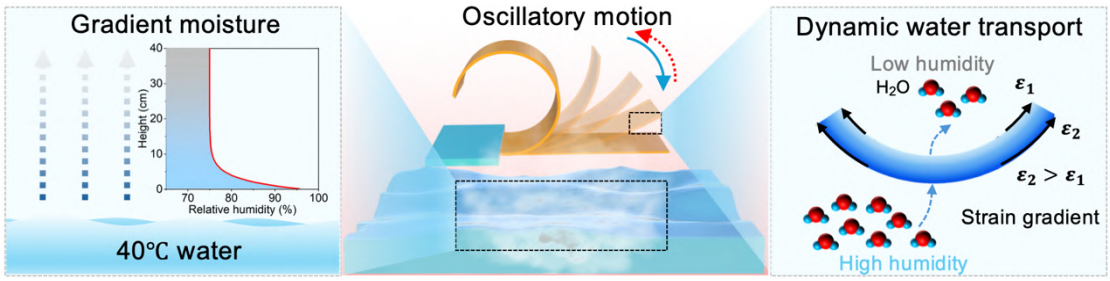

Figure 5.6 Schematic illustration of the synergy between water transport and hygroscopic expansion for the oscillatory behavior of SNA membranes in gradient moisture.

5.1.1 Mechanism of the reversible in-plane hygroscopic expansion

Fundamental principles of mechanics indicate that the bending deformation of a thin structure requires an asymmetric distribution of in-plane strain across its thickness [105]. The specific mechanisms underlying hygroscopic in-plane expansion, however, vary with the material system. For GO/SA membranes, it is well established that such expansion originates from chemical restructuring of the sodium alginate (SA) phase upon water absorption [39]. In contrast, the origin of hygroscopic in-plane expansion in MXene/NP membranes remains unresolved [39, 62]. While hydration-induced d-spacing expansion accounts for out-of-plane dimensional changes in MXene [62, 168],

it does not explain the substantial in-plane strain implied by the pronounced bending deformation of MXene-based membranes in water vapor. Given the pronounced influence of nanoparticle doping on the hygroscopic expansion of MXene/NP membranes, the in-plane expansion is attributed to the flattening of pre-existing nano-wrinkles formed during the stacking of flexible MXene nanoflakes. To examine this mechanism, the nano-wrinkle density in MXene/NP membranes was intentionally reduced via a confined dehydration process (**Figure 5.7 (a)**). Compared with the untreated control sample, the processed membranes displayed a markedly reduced nano-wrinkle density (**Figure 5.7 (b)**) and a diminished hygroscopic expansion under the same moisture stimulus (**Figure 5.7 (c)**), indicating that the macroscopic hygroscopic expansion is governed by the density of nano-wrinkles. This result explains why the hygroscopic expansion coefficient of MXene/NP membranes is related to the nanoparticle content: an appropriate amount of nanoparticles introduces more wrinkle structures into the MXene flakes, allowing the MXene/NP membrane to unfold more wrinkles and generate larger in-plane strain when absorbing the same amount of moisture. However, excessive nanoparticles lead to aggregation, which disrupts the layered structure of the MXene flakes, thereby reducing the hygroscopic expansion performance of the MXene/NP membrane.

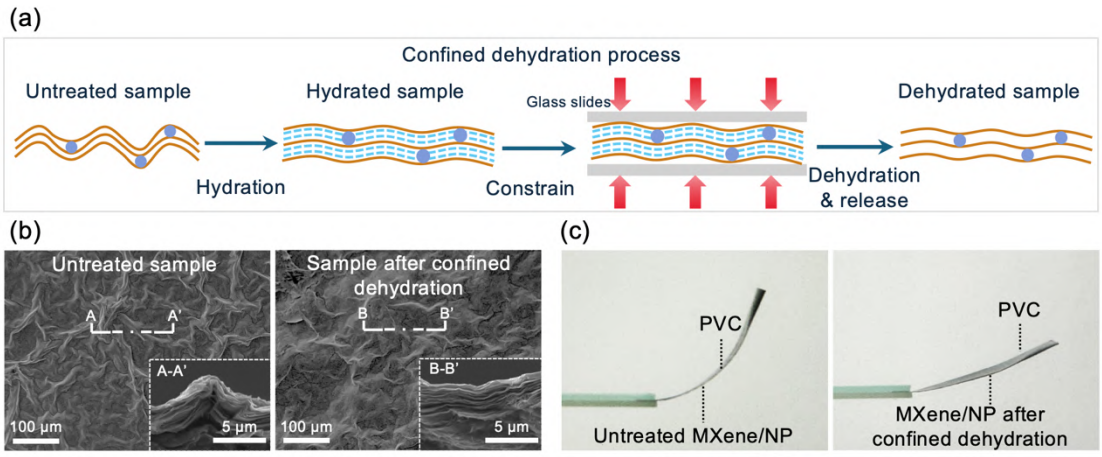

Figure 5.7 Wrinkle flattening mechanism of in-plane hygroscopic expansion. (a) Schematic illustration of the constrained dehydration process. (b) SEM images of cross-section and surface morphology of an untreated MXene/NP membrane and a MXene/NP membrane after a confined dehydration process. (c) Comparison of the bending deformation of two bilayer strips subjected to the same moisture stimulus. Both samples are composed of the same inert layer (PVC) but different active layers: an untreated MXene/NP membrane, and a MXene/NP membrane after confined dehydration.

5.2 Theoretical analysis of the oscillation

The sustained oscillation of SNA membranes in a steady water vapor flow arises from the coupling of two dynamic physical processes: through-thickness water transport and bending induced by hygroscopic expansion (**Figure 5.8**). To elucidate the fundamental physics governing these processes, the membrane is modeled as a two-dimensional beam with length l, thickness h, and density ρ. Disregarding the exact physical mechanism of the water transport, it is assumed that the tempo-spatial evolution of the water concentration (C) within the membrane complies with the one-dimensional Fick's law $\frac{\partial C}{\partial t} = D\frac{\partial^2 C}{\partial y^2}$, where D is a constant coefficient, also called

diffusivity, characterizing the rate of water transport along the thickness direction (y). An intrinsic time scale characterizing the speed of water transport across the membrane thickness is given by $t_{\mathrm{D}} \equiv \frac{h^2}{D}$.

On the other hand, the deflection of the beam (v) is described by the dynamic Euler–Bernoulli beam equation [169]

$$EI\left(\frac{\partial^4 v}{\partial x^4}\right) + \rho h \frac{\partial^2 v}{\partial t^2} = \frac{\partial^2 M_\beta}{\partial x^2} \tag{5.1}$$

where E is the Young's modulus, $I \equiv \frac{1}{12}h^3$ is the moment of inertia of the beam of unit width, and M_β is the equivalent bending moment produced by the hygroscopic expansion. It can be demonstrated that M_β is associated with the in-membrane water concentration C through $M_\beta(x,t) = E\beta \iint C(x,y,t) y dA$, where β is the hygroscopic expansion coefficient, implying the coupling between the water transport process and the dynamic deflection process. An intrinsic time scale characterizing the speed of dynamic deflection is defined as the structure's natural oscillation period: $t_{\mathrm{V}} \equiv \frac{l^2}{h}\sqrt{\frac{12\rho}{E}}$. Notably, the ratio between time scales t_{D} and t_{V} has been found to play an important role in determining the oscillation behaviours of the beams induced by other similar stimuli [167].

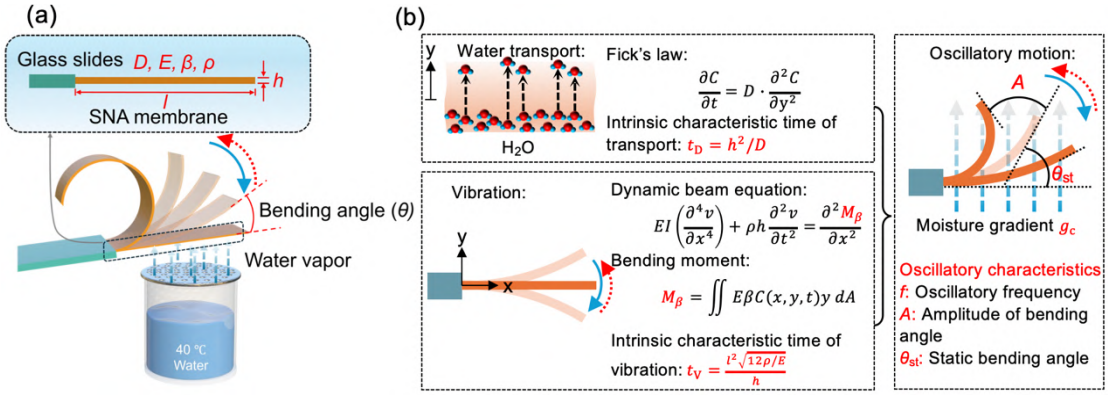

Figure 5.8 Theoretical modelling and numerical simulation of moisture-driven oscillation of SNA membranes (a) Mechanical model of the SNA membrane. (b) Schematic illustration of the coupling between water transferring and the dynamic beam vibration process.

Given the complex time-dependent boundary conditions and the large deformations of the membranes subjected to moisture gradients, obtaining an analytical solution to the coupled diffusion–vibration equations is highly challenging, if not infeasible. As an alternative, finite element (FEM) simulations were employed to predict the dynamic behavior of SNA membranes under moisture gradients replicating experimental conditions (**Figure 5.9**).

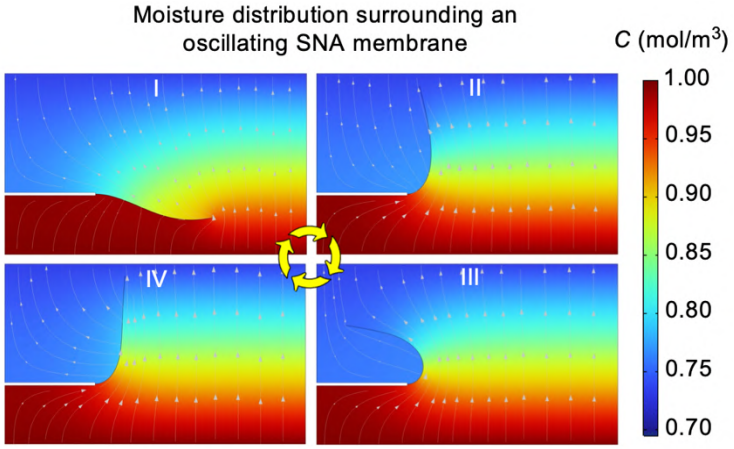

Figure 5.9 Snapshots of the oscillating behavior of SNA membranes in FEM simulation

The simulations successfully reproduced the cyclic oscillatory motions of both MXene/NP and GO/SA membranes, showing strong agreement with experimental observations in key oscillatory characteristics—including frequency, amplitude, and static bending angle (**Figure 5.10**)—thereby validating the FEM approach.

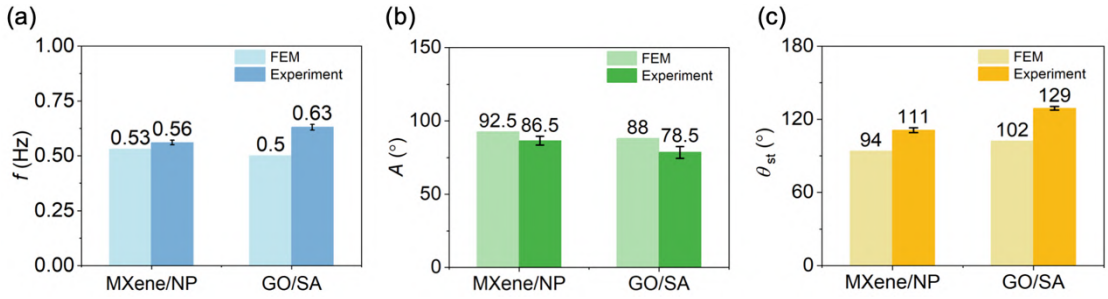

Figure 5.10 Comparison of FEM and experiment results of (a) frequency, (b) amplitude, and (c) static bending angle of MXene/NP and GO/SA membrane.

Further FEM analysis revealed that the mean moisture concentration within the SNA membranes oscillates periodically, exhibiting an opposite phase relative to the bending angle (**Figure 5.11**). When the membrane is fully flattened, its average water concentration reaches the maximum, whereas at the maximum bending angle, the average water concentration is at the minimum. This is clearly related to the membrane's position: in the external humidity field, the lower the height, the higher the concentration.

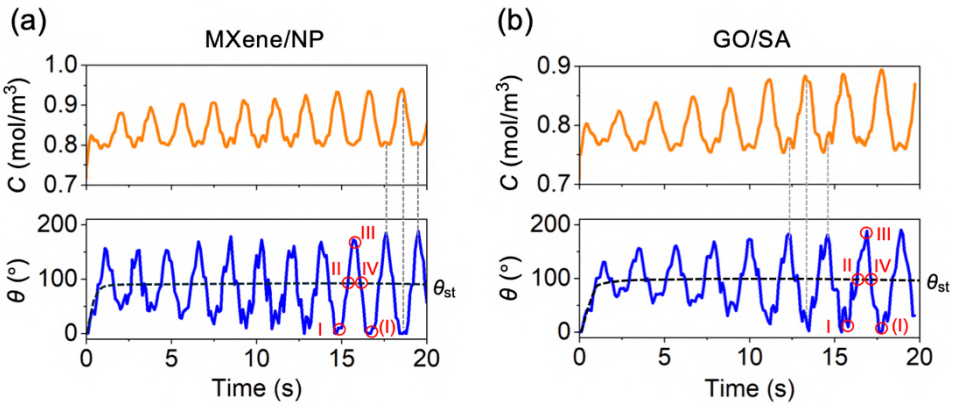

Figure 5.11 Calculated variations of average concentration of water (C) and bending angle (θ) with time in (a) MXene/NP membrane and (b) GO/SA membrane.

This observation suggests the presence of a negative feedback loop linking mechanical deformation and water transport. To investigate the dynamics of water movement during oscillation, the moisture flux across the top and bottom surfaces of the membranes was analyzed (**Figure 5.12**), revealing a periodic, breathing-like absorption–desorption cycle.

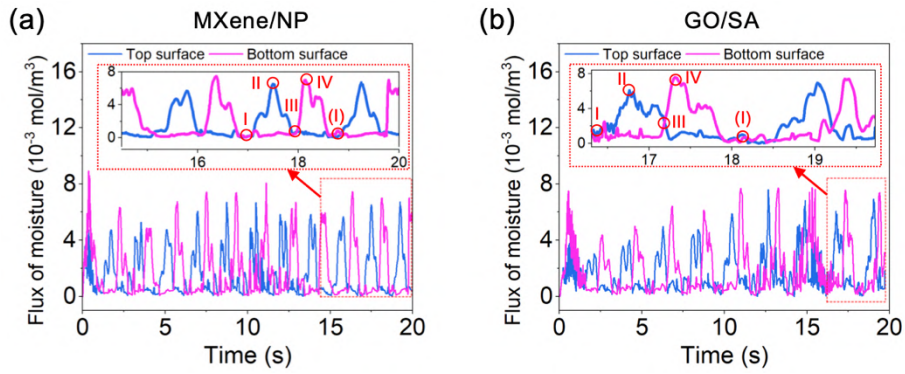

Figure 5.12 Calculated fluxes through the top and bottom surfaces of the (a) MXene/NP and (b) GO/SA membrane as functions of time.

A representative oscillation cycle, highlighting moments I–IV (**Figures 5.11** and **5.12**), illustrates the process in detail. During the first half cycle (I → II → III), as the

membrane bends upwards, water is expelled predominantly through the top surface while absorption at the bottom remains minimal. Conversely, during the second half cycle (III → IV → I), as the membrane rebounds downward, water is absorbed mainly through the bottom surface with negligible desorption at the top. Notably, the peaks of outflux and influx occur at moments II and IV, respectively, coinciding with the membrane's maximum swinging speed in opposite directions.

This dynamic exchange between the membrane and its environment induces fluctuations in internal moisture distribution, resulting in cyclic variations of the through-thickness moisture gradient (**Figure 5.13**). Specifically, during the first half cycle (I → II → III), the moisture gradient between the top and bottom surfaces increases, indicating that water outflux at the top exceeds the rate of diffusive homogenization. By moment III, the gradient reaches its maximum, corresponding to the peak bending deformation. In the second half cycle (III → IV → I), the gradient decreases as diffusion counterbalances the bottom-surface absorption. This recurrent variation of the moisture gradient sustains autonomous oscillations of the membrane. The resulting mechano-fluidic feedback—where bending modulates moisture influx, which in turn drives further deformation—establishes a self-sustained cyclic oscillation mechanism.

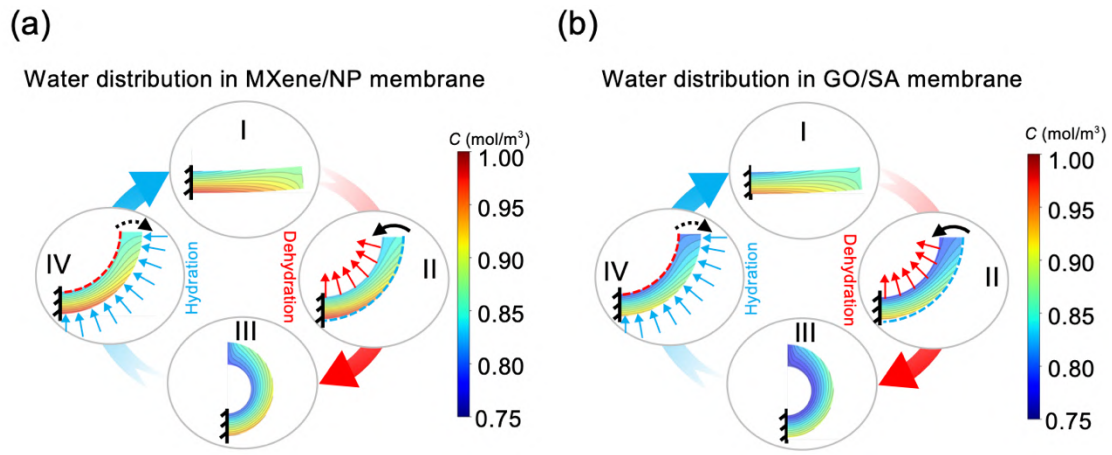

Figure 5.13 Calculated moisture distribution in the (a) MXene/NP and (b) GO/SA membranes at four feature moments in a representative cycle (dimensions and bending angles here are not to scale).

5.3 Rational regulation of the oscillation

5.3.1 Dimensional analysis of the oscillation

To gain more insights into the moisture-driven oscillation of the SNA membranes, a theoretical model was built up in which the SNA membrane is considered as a two-dimensional (plane-strain assumption) continuum cantilever with length l and thickness h, Young's modulus E, and density ρ. The water transport in the membrane is effectively considered as a diffusion process with diffusivity D, and the hygroscopic swelling behavior of the membrane is described by the hygroscopic expansion coefficient β, which represents the strain caused by a unit change of moisture concentration. The membrane is horizontally placed in an environment with a moisture concentration linearly decreasing with altitude at a constant gradient of g_C. Above 7 parameters (*i.e.*, l, h, E, ρ, D, β, g_C) fully define the model problem. In other words,

the dynamic response of the membrane to the stimulus is determined by the values of these parameters. To identify the dominant affecting parameters for a parametric study on the oscillatory motion, a dimensional analysis was carried out based on the Buckingham's π theorem.

Buckingham's π theorem [170] is a powerful tool for dimensional analysis. It offers a facile method for identifying a set of dimensionless parameters from given dimensional physical variables, or nondimensionalization, even if the form of the governing equation is unknown. Specifically, if there are n physical variables in a problem and these variables involve m basic physical dimensions such as M(mass), L(length), and T(time) et al., the governing equation can be rewritten in terms of $(n - m)$ dimensionless parameters. For the model problem defined above, there are 7 physically meaningful variables including l (length), h (thickness), E (Young's modulus), ρ (density), D (diffusion coefficient), β (hygroscopic expansion coefficient), g_C (gradient of moisture concentration in the environment). These variables involve 4 basic dimensions including L (length in units of m), M (mass in units of kg), T (time in units of s) and N (quantity in units of mol). According to the Buckingham's π theorem, solutions to the nondimensionalized governing equations of this problem depend only on 3 independent dimensionless parameters, or groups, denoted as $\Pi_i (i = 1,2,3)$.

By choosing h, D, E and β as 4 repeating variables, then the dimensionless parameters are expressed in terms of the repeating variables as

$$\begin{cases} \Pi_1 = l^{a_1} h^{a_2} D^{a_3} E^{a_4} \beta^{a_5} \\ \Pi_2 = \rho^{b_1} h^{b_2} D^{b_3} E^{b_4} \beta^{b_5} \\ \Pi_3 = g_C^{c_1} h^{c_2} D^{c_3} E^{c_4} \beta^{c_5} \end{cases} \tag{5.2}$$

where indices $a_i,\ b_i,\ c_i\ (i = 1,2,\dots,5)$ can be determined according to the fact that the dimensions on both sides of the above three equations should be identical.

For the dimensionless Π_1 parameter, the dimensional matrix, where the rows correspond to the basic dimensions *T*, *M*, *L*, and *N* and the columns to the dimensional variables $L,\ h,\ D,\ E$, and β, is given by

	L	h	D	E	β
T	0	0	-1	-2	0
M	0	0	0	1	0
L	1	1	2	-1	3
N	0	0	0	0	-1

or

$$\text{matrix} = \begin{bmatrix} 0 & 0 & -1 & -2 & 0 \\ 0 & 0 & 0 & 1 & 0 \\ 1 & 1 & 2 & -1 & 3 \\ 0 & 0 & 0 & 0 & -1 \end{bmatrix}$$

The matrix-vector multiplication is given by

$$\begin{bmatrix} 0 & 0 & -1 & -2 & 0 \\ 0 & 0 & 0 & 1 & 0 \\ 1 & 1 & 2 & -1 & 3 \\ 0 & 0 & 0 & 0 & -1 \end{bmatrix} \begin{bmatrix} a_1 \\ a_2 \\ a_3 \\ a_4 \\ a_5 \end{bmatrix} = [0 \quad 0 \quad 0 \quad 0]$$

The solution can be obtained by taking the index of a prime quantity $a_1 = 1$, then the vector *a* becomes

$$a = \begin{bmatrix} 1 \\ -1 \\ 0 \\ 0 \\ 0 \end{bmatrix}$$

Substituting the values of the vector $\boldsymbol{a}$ as exponents in Π_1, it can be determined by $\Pi_1 = \frac{L}{h}$.

Therefore, the variables are $\Pi_1 = lh^{-1}$, $\Pi_2 = hD^{-1}E^{1/2}\rho^{-1/2}$, $\Pi_3 = g_C\beta h$. The solutions to the governing equations (nondimensionalized) of the model problem depend on the values of three dimensionless parameters Π_1, Π_2, Π_3. Obviously, one can choose the other three dimensionless parameters derived from Π_1, Π_2, Π_3 as long as the independence between them is ensured. In our study, for example, three dimensionless parameters were chosen as follows:

$$S \equiv \Pi_1 = \frac{l}{h},\ B \equiv \frac{\Pi_2}{\Pi_1^2\sqrt{12}} = \frac{h^3}{l^2 D}\sqrt{\frac{E}{12\rho}},\ \varepsilon_\Delta \equiv \Pi_3 = g_C\beta h. \qquad (5.3)$$

Such a selection makes the resulting dimensionless parameters more meaningful in physics. In particular, S describes the slenderness of the membrane, B represents the competition between the intrinsic time scales of diffusion and vibration: $t_{\mathrm{D}} \equiv \frac{h^2}{D}$ and $t_{\mathrm{V}} \equiv \frac{l^2}{h}\sqrt{\frac{12\rho}{E}}$, and ε_Δ stands for the maximum mismatch strain that the stimulus can impose across the thickness of the membrane.

5.3.2 Dictating parameters of the oscillation

To quantitatively assess the influence of these dimensionless groups on oscillation behavior, a parametric study was performed using finite element analysis,

systematically varying the values of S and B while keeping ε_Δ constant. The dependence of oscillatory characteristics—frequency (f), amplitude (A), and static bending angle (θ_{st}) —on S and B is visualized in phase diagrams for both MXene/NP and GO/SA membranes at different ε_Δ values, which differ due to variations in membrane thickness h. These two phase diagrams reveal similar frequency responses between MXene/NP and GO/SA membranes at different ε_Δ values (**Figure 5.14 (a)**). Notably, oscillating frequency exhibits strong dependence on B and S but remains insensitive to ε_Δ, as the latter governs strain magnitude rather than dynamic coupling. The time-scale parameter B emerges as a critical frequency modulator: lower values (indicating faster moisture diffusion relative to mechanical response) accelerate system equilibration, suppressing oscillations. Consequently, frequency increases with B at fixed S, demonstrating tunability through material selection and geometric design.

Amplitude and static bending angle analysis (**Figures 5.14 (b), (c)**) identifies optimal performance regions combining lower B and higher S. This inverse correlation stems from thickness-dependent stiffness reduction – thinner membranes with elevated S exhibit diminished flexural rigidity ($EI \propto h^3$), amplifying deformation under equivalent hygroscopic moments. For instance, doubling S through length extension or thickness reduction enhances compliance, simultaneously boosting transient oscillation magnitude and steady-state curvature. The ε_Δ parameter further modulates deformation capacity, with higher values enabling greater maximum bending through intensified hygroscopic strain gradients.

Together, this parametric framework establishes systematic design principles for tailoring the dynamics of humidity-responsive oscillating membranes. Maximizing S and ε_Δ enhances deformation potential through geometric optimization and material hygroscopicity tuning, while strategic B adjustment balances frequency and amplitude requirements. Practical implementation involves tailoring membrane geometry to adjust S, modifying nanoflake compositions to regulate water diffusivity (D) and hygroscopic responsivity (β), and optimizing environmental conditions to enhance moisture gradients (g_c). Such multidimensional control provides a rational path for customizing oscillation dynamics of SAN membranes for diverse applications ranging from energy harvesting to biomimetic propulsion systems.

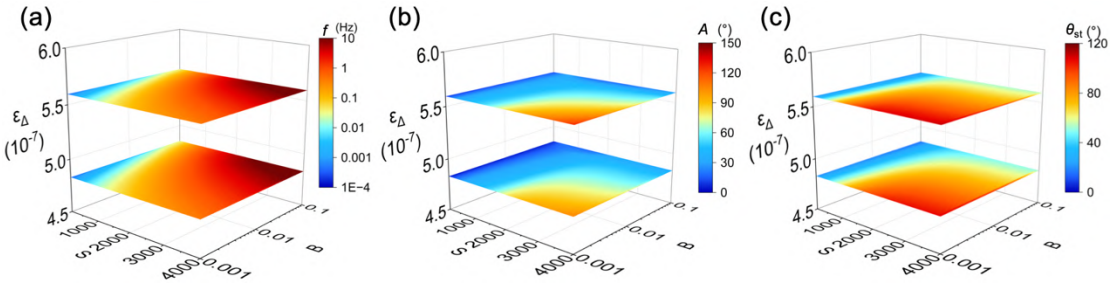

Figure 5.14 Phase maps showing the influences of the dimensionless parameters B, S, and ε_Δ on the oscillation behavior characterized by **(a)** frequency (f), **(b)** oscillation amplitude (A), **(c)** static bending angle (θ_{st}). Here, the strain mismatch ε_Δ, which can be determined from moisture gradient g_C, hygroscopic expansion coefficient β, and membrane thickness h, is taken as 5.61×10^{-7} for the MXene/NP sample and 4.86×10^{-7} for the GO/SA sample.

5.4 Summary

In this chapter, the oscillatory behavior of single-layer SNA membranes under

gradient humidity stimulation was systematically investigated. A series of control experiments confirmed that the oscillation is independent of heat and vapor flow momentum; rather, it arises from external humidity gradients coupled with reversible hygroscopic in-plane expansion. Furthermore, our explanation of the microscopic mechanism underlying the reversible in-plane expansion of MXene membranes provides new insights for the study of humidity-responsive applications of MXene-based membranes. Unlike most previous studies that primarily focus on the potential applications of oscillatory behavior, the mechanical model proposed in this chapter successfully predicts the oscillation of SNA membranes, enabling principle-based control and prediction of sustained periodic responses of single-layer membranes under similar conditions.

However, this work has certain limitations. For instance, MXene/NP and GO/SA membranes exhibit limited service lifespan in ambient humidity environments due to oxidation and hygroscopic saturation (to be discussed in the next chapter), which significantly restricts their practical applicability. Considerable efforts have been devoted to mitigating oxidation in two-dimensional materials, such as surface modification [171], reactive surface reformation [172], and modifying fabrication process including bottom-up growth for heterostructures [173], as well as liquid-solid phase self-assembly approach [174]. Yet, whether such modifications affect their humidity-induced oscillatory behavior remains unknown. In addition, it is still unclear whether our findings can be generalized to other hygroscopic membranes exhibiting

similar phenomena, for instance, a composite monolayer membrane made by spiropyran and agarose was also able to generate an oscillatory motion in the ambient humidity field [175]. Finally, the finite-element simulations conducted in this study approximate the humidity gradient above a 40 °C water bath; incorporating an explicit evaporation model in future simulations could further enhance their accuracy and credibility.

Chapter 6. Application of moisture-driven oscillation

Moisture plays a significant role in the fields of actuators and energy harvesting, with membrane materials consistently remaining at the forefront of research. In moisture-driven actuators, membrane materials have demonstrated functionalities such as crawling [123, 176], lifting [177], and gripping [178]. Moreover, owing to their high sensitivity to moisture, hygroscopic membrane actuators also hold great potential in applications such as health monitoring [179] and thermoregulation devices [95]. In the field of energy harvesting, in addition to electricity generation via proton diffusion and ion migration within moisture-driven membranes [180], and via piezoelectric effects induced by moisture-driven expansion/contraction of membranes [163, 181, 182], electromagnetic induction can also be achieved through the reciprocating motion of moisture-driven membranes. For example, moisture can drive a windmill composed of membrane materials to rotate, thereby cutting magnetic flux lines and generating induced currents [117]. However, most moisture-driven membrane actuators and generators rely on controlling the moisture source to induce continuous cyclic motion, which reduces energy conversion efficiency and increases device complexity. Moreover, although numerous studies have elucidated the degradation mechanisms of MXene and GO in considerable detail [183, 184], little attention has been paid to how these mechanisms influence their hygroscopic oscillatory behavior. For instance, MXene undergoes rapid oxidation in air—within a timescale of several hours to days—and this process is accelerated by water vapor and elevated temperatures [185]. Our

observations reveal that MXene/NP and GO/SA membranes cannot oscillate permanently in humid environments. Investigating the underlying mechanisms governing this limitation would therefore provide valuable insights for expanding the application potential of SNA membranes.

Therefore, membrane materials capable of generating sustained reciprocating motion under constant humidity conditions have tremendous potential in both actuator and energy-harvesting applications. The MXene/NP and GO/SA membranes described in the previous chapter exhibit precisely this characteristic. Although this phenomenon is not being reported here for the first time—many previous studies have documented similar observations—the underlying mechanical and rational mechanisms have not been systematically investigated. The mechanical model and parametric analysis presented in the previous chapter can serve as a guide for controlling and predicting the hygroscopic oscillation behavior of SNA membranes. Based on this finding, the potential applications of SNA membranes in actuator and energy-harvesting systems can be further explored. Additionally, this chapter will also state an in-depth comparison of the key parameters of SNA membranes before and after failure and interpret the associated mechanical failure mechanisms using the analytical framework established in the preceding chapter.

6.1 Application of moisture-driven oscillation in propulsion

Inspired by the resemblance of the oscillatory motions between the SNA

membranes and flukes, a fluke-inspired propeller with MXene/NP membrane was developed and used to drive a mini-boat of 3 g in weight (**Figure 6.1**). A prototype of a propeller was prepared by tailoring an MXene/NP-based membrane into a fluke-like shape.

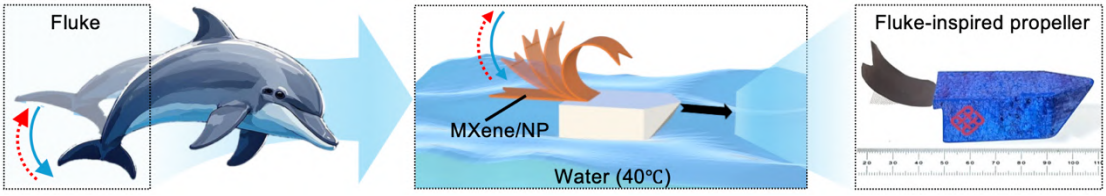

Figure 6.1 Schematic illustration of the working principle of a fluke-inspired propeller driven by moisture.

The slenderness ratio (S) of the propeller, a critical parameter governing oscillatory amplitude, was designed based on the concerned phase map (**Figure 6.2**). To maximize the oscillating amplitude for a better performance of propulsion, a design of the propeller was opted with $S = 3750$ and $B = 0.0015$ under the guidance of the theoretical phase diagrams.

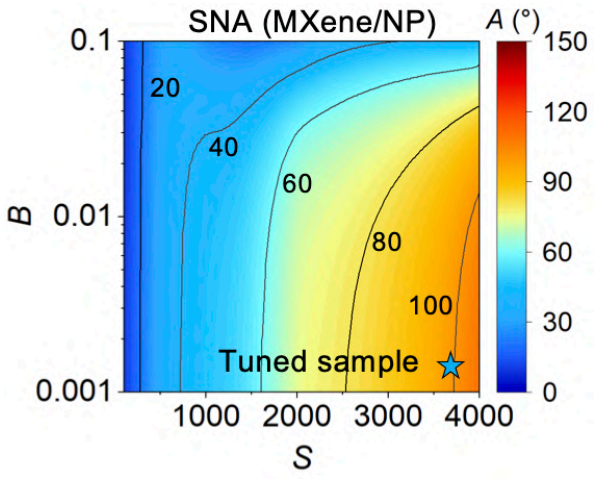

Figure 6.2 Theoretical phase map guiding the design of the propeller for higher amplitude. The construction of this map is based on $\varepsilon_{\Delta} = 5.6 \times 10^{-7}$.

The resulting propeller was affixed to the tail of a min-boat constructed from lightweight polystyrene foam. A piece of stainless-steel mesh was attached beneath the propeller to prevent direct contact with water. When the mini-boat is deployed in a water bath (~40°C), the propeller flaps in response to the moisture stimulus spontaneously, driving the mini-boat to move forward at an average velocity of 0.12 body length/s (**Figure 6.3**).

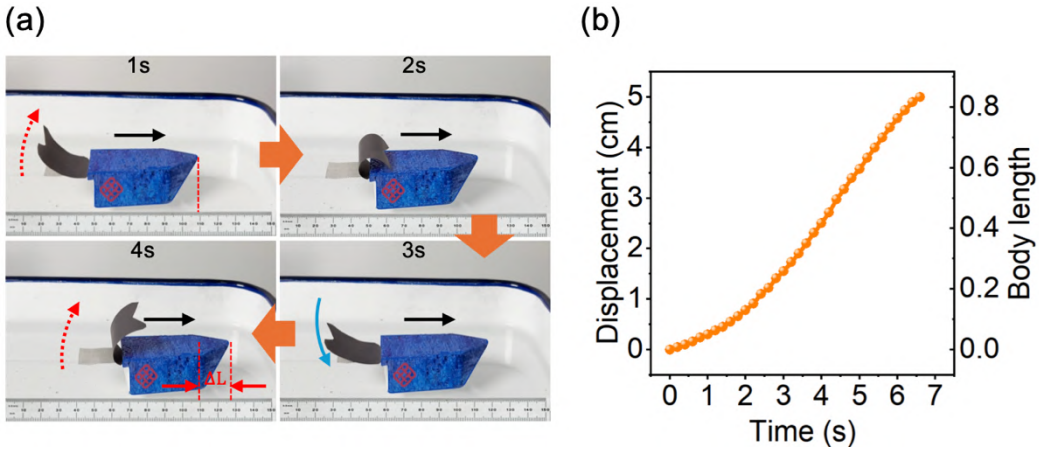

Figure 6.3 (a) Snapshots of the mini-boat driven by the fluke-inspired propeller. (b) Displacement-time curve of the mini-boat driven by the fluke-inspired propeller.

6.2 Application of moisture-driven oscillation in energy harvesting

To further demonstrate the application potential of the SNA membranes in energy conversion and generation, we developed a nanogenerator with a GO/SA membrane based on the principle of contact-separation triboelectric principle. To enable diffusion of moisture across both surfaces of the GO/SA membrane, through holes were introduce in the Nylon–copper foil bilayer. When exposed to the weak moisture emitted from a hand, the GO/SA membrane exhibits continuous oscillation, resulting in a periodic

contact–separation process with the Nylon-based positive triboelectric layer. It enables us to collect electrical energy from the weak moisture gradient above a human hand (**Figure 6.4**).

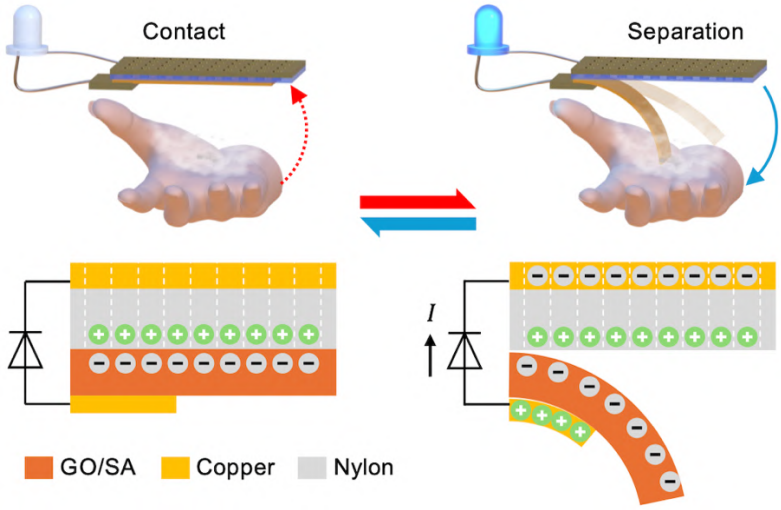

Figure 6.4 Schematic illustration of the working principle of the hand moisture nanogenerator.

The maximum strain ε_{Δ} that GO/SA membrane can generate in moisture gradient g_c of the human palm is determined by the humidity distribution along the height from the palm skin (**Figure 6.5**), which can be also measured by the sensor made by the MXene strip.

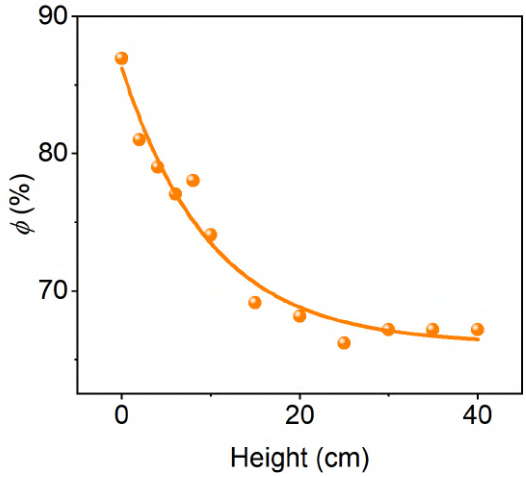

Figure 6.5 Relative humidity distribution along the height from the palm skin

Guided by the corresponding phase maps (**Figure. 6.6**), we reached a satisfactory design of the membrane with S = 1500, B = 0.043. When placed above a human hand, the membrane flaps at a frequency of 0.9 Hz and amplitude of 32°.

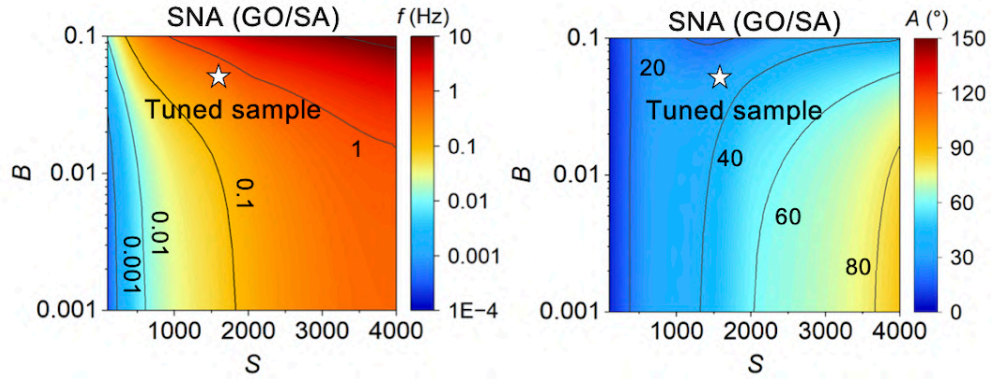

Figure 6.6 Theoretical phase maps guiding the design of the GO/SA membranes for considerable frequency and oscillation amplitude. The construction of these maps is based on $\varepsilon_{\Delta} = 2.68 \times 10^{-7}$ as determined from corresponding measurements.

As a result, a periodic contact–separation occurs between the two layers, generating a pulsing voltage output with a peak voltage of approximately 1.7 V (**Figure 6.7**), which is recorded by the voltmeter within a Digital Multimeter, with an impedance factor of 100MΩ (DM3068, RIGOL).

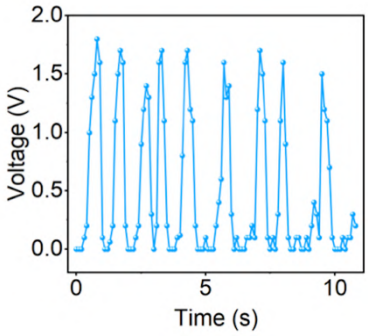

Figure 6.7 Induced voltage signal generated by the hand moisture-driven nanogenerator.

This voltage can be used directly to light up an LED lamp (**Figure 6.8**), or charge a second battery after rectification, demonstrating the high potential of hygroscopic SNA membranes in ambient energy harvesting.

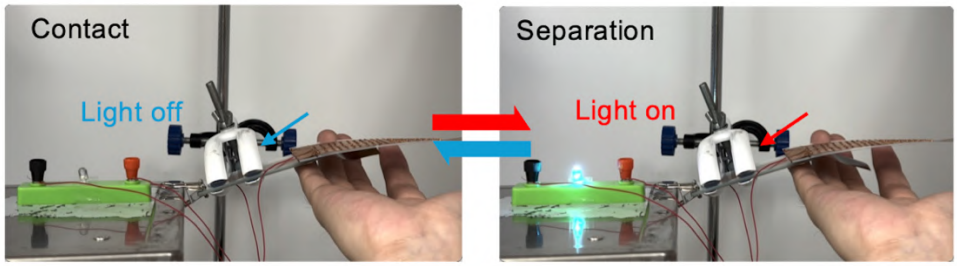

Figure 6.8 Snapshots of the hand moisture-driven nanogenerator lighting up an LED lamp.

6.3 Performance decay of SNA membranes

6.3.1 Performance decay of MXene/NP membranes

It is worth noting that the oscillatory behavior of MXene/NP and GO/SA membranes under humidity is not permanent. For the MXene/NP membrane, oscillations typically last for 2–3 hours, after which the behavior transitions into a static bending deformation. To determine whether this decay is caused by oxidation of MXene or by saturated moisture absorption, a series of verification experiments was

conducted. To verify whether it is due to saturation, MXene/NP membranes that could no longer oscillate were placed in a vacuum drying chamber ($\emptyset = 30\%$) for drying. Based on this procedure, the samples were classified into three states: the pristine state (oscillatory), the decayed state (non-oscillatory), and the re-dried state. It turned out that the oscillation did not recover in re-dried membranes (**Figure 6.9**), indicating that moisture saturation was not the underlying cause.

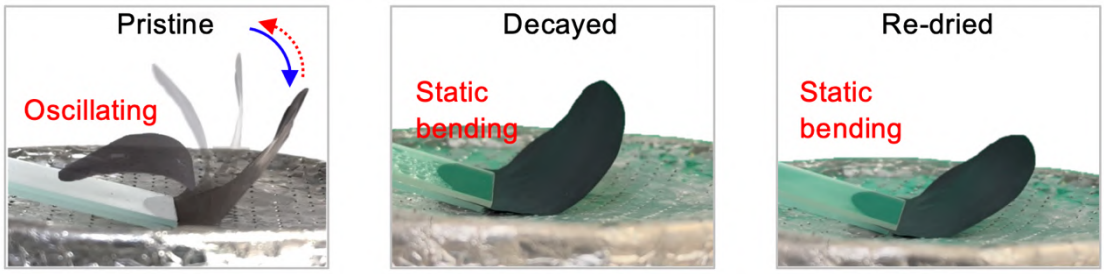

Figure 6.9 Humidity responses of pristine, decayed, and re-dried MXene/NP membrane

The physical properties of the three states were then re-measured. In terms of mechanical properties, uniaxial tensile tests showed that the Young's modulus of the membranes exhibited no significant changes; however, the tensile strength of the decayed and re-dried states was dramatically reduced (**Figure 6.10**). This suggests that prolonged exposure of MXene/NP membranes to water vapor and air might lead to oxidation.

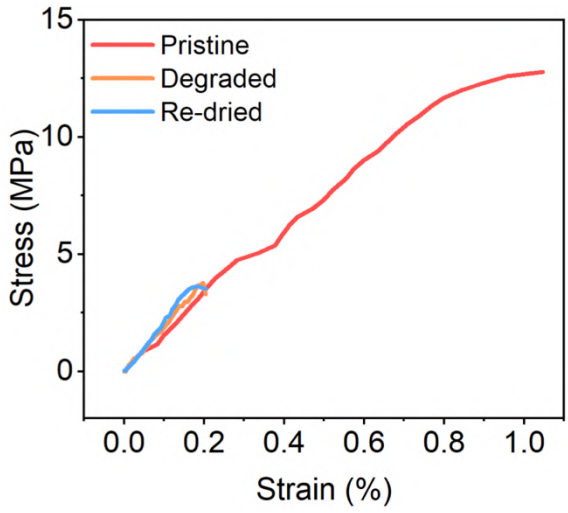

Figure 6.10 Stress-strain curve of pristine, decayed, and re-dried MXene/NP membranes.

To verify this hypothesis, X-ray diffraction (XRD) measurements were performed on the three membrane states. The results showed distinct changes in the 2-theta peaks for the decayed and re-dried samples, indicating an increased TiO_2 content within the MXene/NP membranes—strong evidence of MXene oxidation (**Figure 6.11**). Previous studies have reported that when Ti atoms in MXene flakes are oxidized to TiO_2, the mechanical properties are significantly decreased, which also explains the reduction in tensile strength observed in the latter two states.

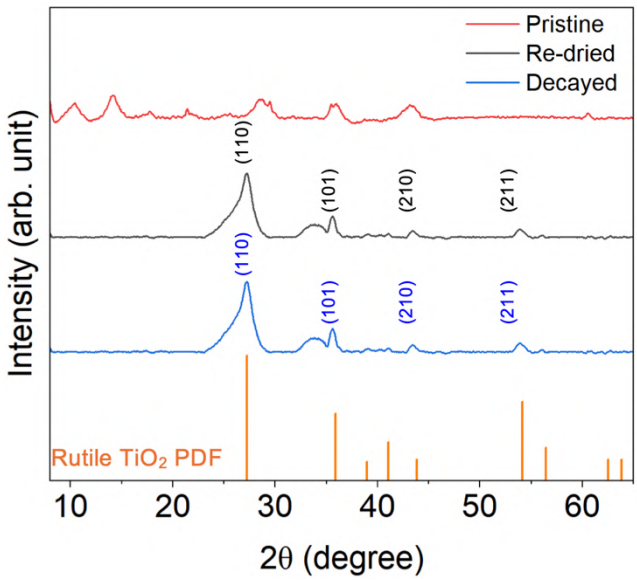

Figure 6.11 XRD curve of pristine, decayed, and re-dried MXene/NP membranes.

To reveal the reason why oxidized MXene/NP membranes are unable to oscillate, water diffusivity was compared across the three membrane states. As shown in **Figure 6.12**, oxidized membranes exhibited markedly higher diffusivity, implying that the characteristic diffusion time t_D was substantially reduced. This accelerates water transport through the membrane thickness, allowing the concentration gradient to stabilize more quickly. As a result, the dimensionless number *B* decreases, lowering the oscillation frequency.

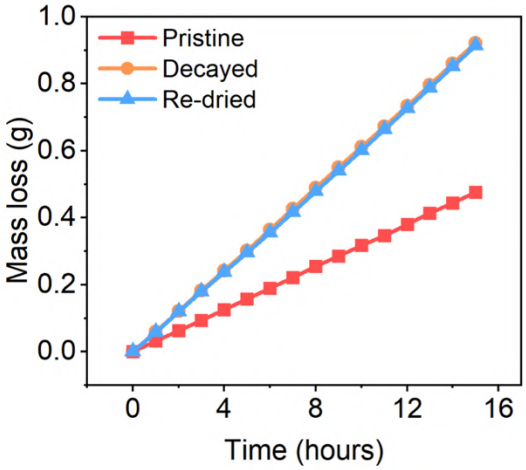

Figure 6.12 Weight loss of water as a function of time for pristine, decayed, and re-dried MXene/NP membrane.

The hygroscopic expansion coefficient (HEC) of the three MXene/NP membrane states was also measured, as shown in **Figure 6.13**. The results indicate a significant reduction in HEC for the oxidized states, implying a reduced bending deformation under humidity stimulus, which further attenuates the oscillatory behavior.

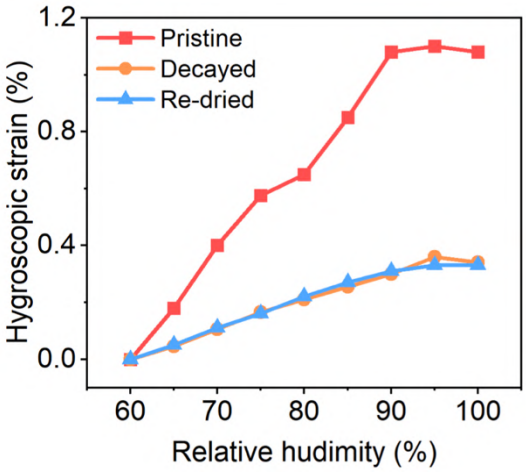

Figure 6.13 Hygroscopic strain generated by pristine, decayed, and re-dried MXene/NP membrane under different relative humidity.

To interpret the disappearance of oscillations using the phase diagram, the density of the membranes was measured in all three states (**Figure 6.14 (a)**). The oxidized

membranes exhibited higher densities. Meanwhile, the changes in water diffusivity and HEC are summarized in **Figure 6.14 (b)**.

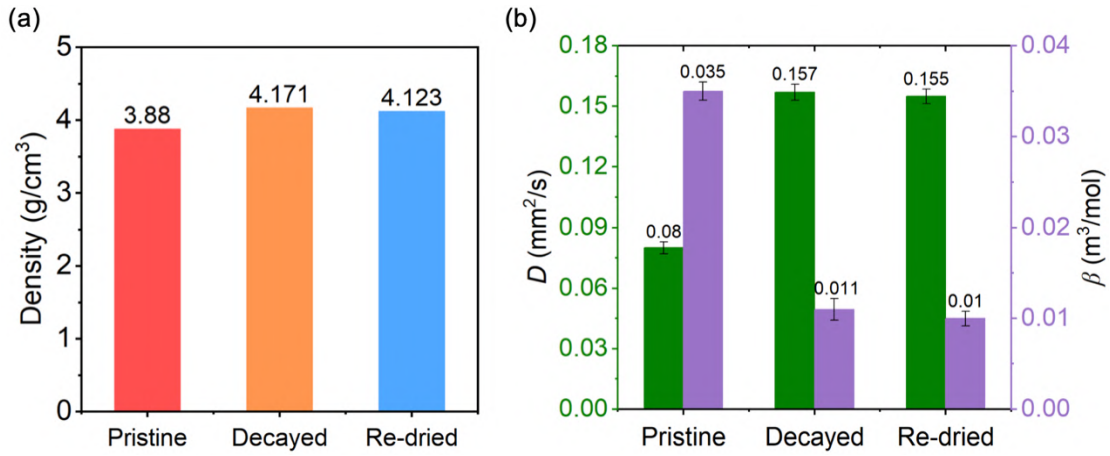

Figure 6.14 (a) Density changes of the MXene/NP membrane under three states. (b) Comparison of water diffusivity D and hygroscopic expansion coefficient β for different states of GO/SA membranes.

Since the previous chapter established that oscillation frequency is not dependent on maximum strain, only the phase diagram of oscillation amplitude after oxidation is shown in **Figure 6.15**. As illustrated, the combined effects of reduced HEC and increased D lead to a substantial decrease in oscillation amplitude. Together with the frequency reduction due to higher D, this phase diagram provides a mechanistic explanation for the transition from oscillation to static unidirectional bending in oxidized MXene/NP membranes.

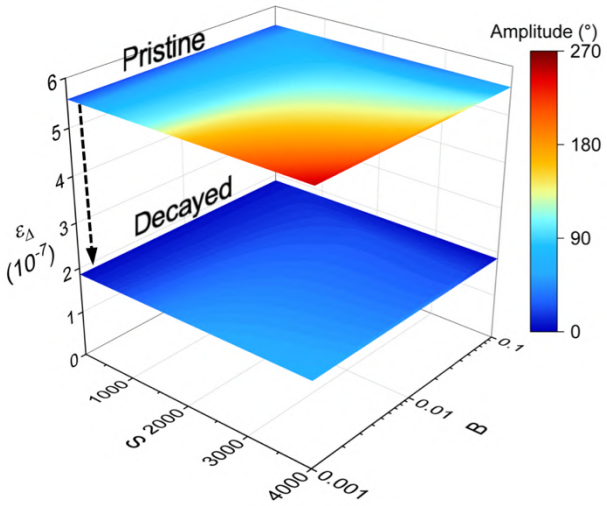

Figure 6.15 Phase map (amplitude) shift of MXene/NP membrane from pristine state to decayed state.

6.3.2 Performance decay of GO/SA membranes

For the GO/SA membrane, the oscillation behavior persisted for only about 10 minutes. Unlike the MXene/NP membrane, the GO/SA membrane gradually flattened and even sagged after oscillation ceased. To determine whether this decay was caused by irreversible oxidation or by hygroscopic saturation, a series of validation experiments was conducted. Non-oscillating GO/SA membranes were dried in a vacuum drying chamber under the same conditions as described before. Similarly, the membranes were categorized into three states: pristine, decayed, and re-dried. In contrast to the MXene/NP membrane, the dried GO/SA membrane recovered its oscillation behavior (**Figure 6.16**), indicating that oxidation was not responsible for the disappearance of oscillation.

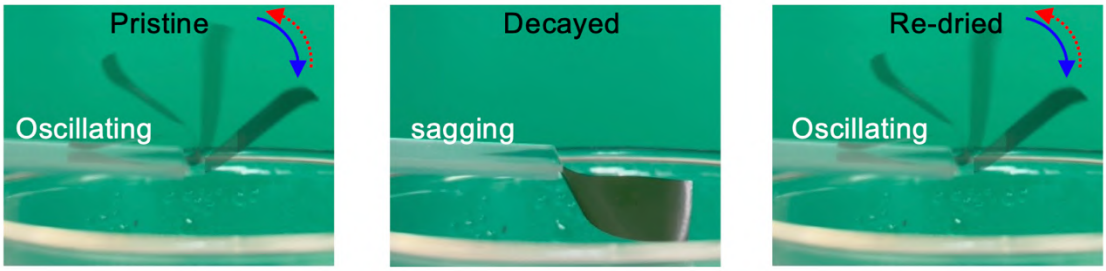

Figure 6.16 Humidity responses of pristine, decayed, and re-dried GO/SA membrane

To examine whether hygroscopic saturation was the cause, the physical properties of GO/SA membranes in the three states were measured. Uniaxial tensile tests revealed no significant change in Young's modulus between the pristine and re-dried samples, whereas the modulus of the decayed membranes was markedly reduced (**Figure 6.17**). This reduction in bending stiffness explains the sagging of the decayed membranes: the combined effects of gravity and the weight of absorbed water induced downward bending.

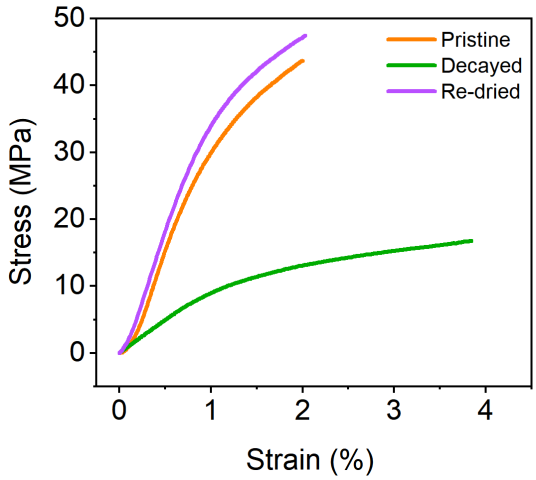

Figure 6.17 Stree-strain curve of pristine, decayed, and re-dried GO/SA membranes.

The water diffusivity of GO/SA membranes in the three states was also measured. The results showed no noticeable variation (**Figure 6.18**), suggesting that the

characteristic diffusion time t_D remained unchanged.

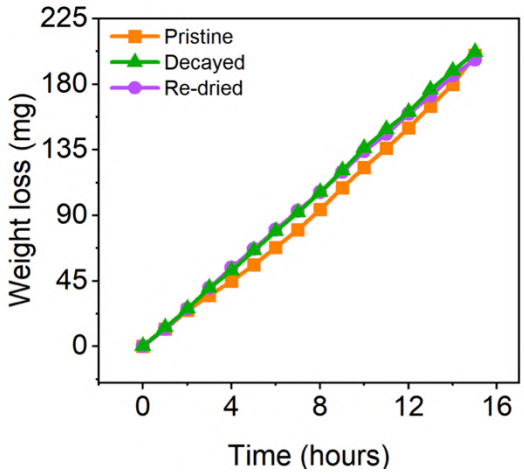

Figure 6.18 Weight loss of water as a function of time for pristine, decayed, and re-dried GO/SA membrane.

Conversely, the hygroscopic expansion coefficient (HEC) exhibited a significant decrease in the decayed membranes (**Figure 6.19**), which accounted for their flattening. A lower HEC reduced the humidity-induced expansion strain, thereby lowering the bending curvature.

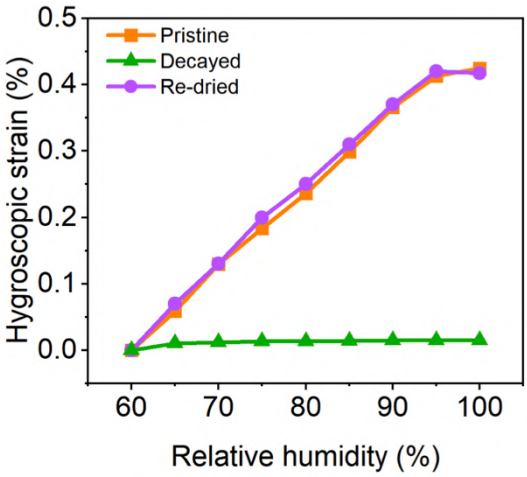

Figure 6.19 Hygroscopic strain generated by pristine, decayed, and re-dried GO/SA membrane under different relative humidity.

To further confirm that the decay effect was due to hygroscopic saturation, the

densities of the membranes in the three states were measured (**Figure 6.20 (a)**). The decayed membranes displayed a higher density due to moisture absorption, which returned to the initial value upon drying. Moreover, after drying, both the water diffusivity and the HEC recovered to their pristine values (**Figure 6.20 (b)**). These results confirm that the disappearance of oscillation in the decayed state was indeed caused by hygroscopic saturation.

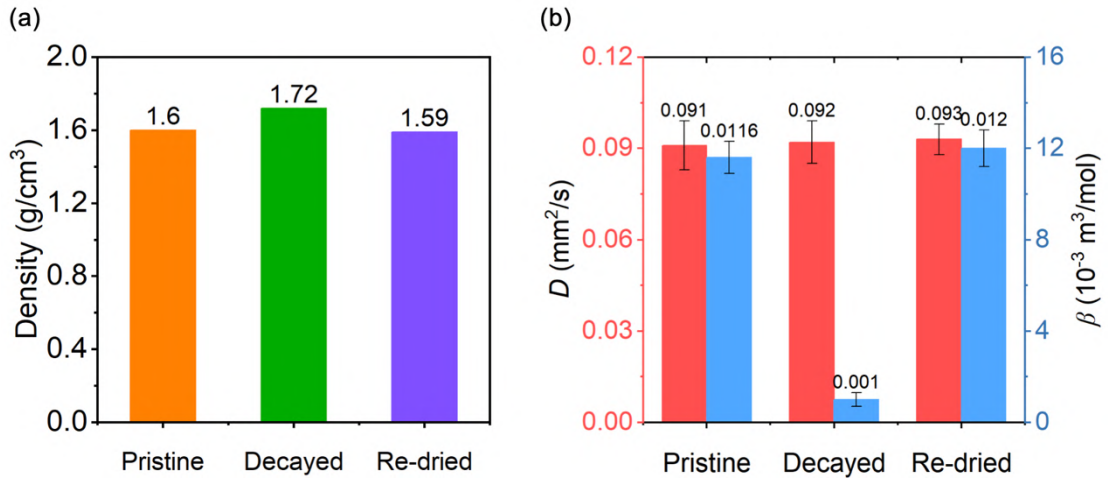

Figure 6.20 (a) Density changes of the GO/SA membrane under three states. (b) Comparison of water diffusivity D and hygroscopic expansion coefficient β for different states of GO/SA membranes.

Finally, the disappearance of oscillation can also be explained using the phase diagram. A substantial decrease in HEC significantly reduced the maximum hygroscopic strain ε_Δ of the membrane, which in turn diminished the oscillation amplitude. Although the frequency remained unaffected due to unchanged diffusivity, the phase diagram shows that regardless of variations in S and B, the amplitude tends toward zero, thereby explaining why the GO/SA membrane gradually flattened after reaching hygroscopic saturation.

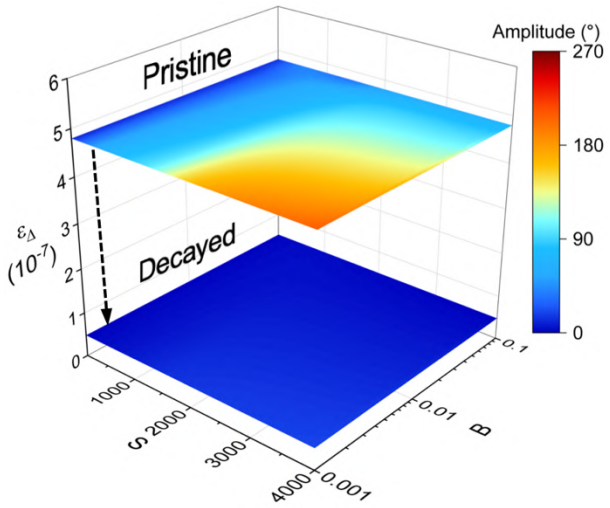

Figure 6.21 Phase map (amplitude) shift of GO/SA membrane from pristine state to decayed state.

6.4 Summary

In this chapter, the universal physical principles underlying the autonomous reciprocating motion of hygroscopic SNA membranes under a constant humidity gradient was elucidated. Three key dimensionless parameters were identified to characterize the structural and physical properties of the membranes and the external stimulus, and their coupled effects on oscillation dynamics were quantitatively established. These insights provide a theoretical basis for rationally tuning oscillation frequency and amplitude via material and structural design, thereby optimizing performance for applications in moisture-driven propulsion and ambient energy harvesting. The proposed framework is broadly applicable, extending beyond humidity-driven oscillations to analogous systems responsive to thermal, chemical, or optical stimuli, thus expanding the potential of responsive materials in energy harvesting and actuation technologies.

Furthermore, the failure mechanisms of SNA membranes in humid environments were effectively elucidated from a mechanical perspective, thereby further validating the universality of the proposed rational regulation strategy. In addition, these findings provide guidance for optimizing the hygroscopic oscillatory behavior of SNA membranes. Specifically, while enhancing the oxidation resistance of MXene and increasing the hygroscopic saturation capacity of GO/SA membranes, it is equally important to ensure a large hygroscopic expansion coefficient, maintain a stable Young's modulus, and preserve favorable water diffusivity.

Chapter 7. Conclusion and future work

Hygroscopic responsive materials play a pivotal role both in nature and in engineering applications. Among them, membrane-based materials demonstrate remarkable potential owing to their lightweight nature, high flexibility, rapid response, and strong programmability. The fundamental mechanism underlying their deformation lies in the non-uniform strain distribution across the membrane thickness, which naturally divides their basic structural design into bilayer and monolayer configurations. In this thesis, the deformative responses of both monolayer and bilayer membranes under humidity stimuli were analyzed and develop mechanical models to predict and rationally design such behaviors, thereby enhancing the application prospects of hygroscopic membranes in actuators and energy harvesting. In this chapter, the key conclusions distilled from this work are summarized, and the directions for future research are highlighted.

7.1 Conclusions

Although extensive research has been conducted on both bilayer and monolayer hygroscopic membranes, the majority of studies have primarily focused on their applications, while comparatively less attention has been given to the underlying mechanical mechanisms and regulation strategies. Notably, the deformation responses of these two structural configurations are different. Phenomenologically, bilayer membranes can only undergo static unidirectional bending, whereas monolayer

membranes are capable of generating sustained oscillatory motion in addition to bending. Mechanistically, bilayer membranes deform due to strain mismatch arising from the different hygroscopic expansion properties between the active and inert layers. In contrast, monolayer membranes rely on non-uniform stimuli or heterogeneous material properties (e.g., surface morphology, hygroscopic expansion coefficient) to induce non-uniform strain distributions within a single layer, thereby driving deformation.

In this work, the deformation mechanisms of both bilayer membranes and monolayer SNA membranes were systematically elucidated from a mechanics perspective. Furthermore, the performance of monolayer SNA membranes was optimized for practical applications, while the proposed framework also provides a mechanistic explanation for the decay of their oscillatory behavior. Several typical conclusions can be summarized as follows.

- The hygroscopic deformation responses of bilayer membranes under arbitrary humidity fields (uniform humidity, linear humidity gradient, and humidity above a 40 °C water bath surface) and different boundary conditions (cantilever and free-standing configurations) were systematically investigated. Based on thin-film mechanics, a simplified two-dimensional theoretical model was developed to calculate the deformation profiles of bilayer membranes. The reliability of this model was validated through cross-verification with experimental results and finite element simulations. Our results show that, for cantilever bilayer membranes, the

deformation response remains steady under all humidity fields due to the constraint of one fixed end. Moreover, the hygroscopic expansion coefficient of the active layer material can be quantitatively determined by measuring the curvature change in a uniform humidity field. In contrast, for free-standing bilayer membranes, the deformation behavior is more complex because, in the theoretical model, the membrane remains in point contact with the substrate (while in practice, line contact is observed). Thus, both the deformed morphology and the stability require further investigation. Through systematic analysis, it was revealed that, for fixed thicknesses of the active and inert layers, the post-deformation stability of the free-standing bilayer membranes depends strongly on the ratio of the Young's moduli of two layers $\frac{E_{\mathrm{in}}}{E_{\mathrm{ac}}}$: a smaller modulus ratio leads to lower stability. Specifically, when the modulus of the inert layer is too low, the deformed membrane's center of mass does not reside at its lowest potential energy state, causing the membrane to spontaneously roll until reaching the position corresponding to the lowest center of mass. These findings not only provide a fundamental insight for predicting the hygroscopic deformation responses of bilayer membranes and a new approach for measuring the hygroscopic expansion coefficient of membrane materials, but also offer practical guidelines for enhancing the structural stability of bilayer hygroscopic membranes.

- The autonomous oscillation of single-layer SNA membranes (MXene/NP and GO/SA membranes) under humidity stimulation was systematically investigated.

The results demonstrate that the sufficient conditions for oscillation are a humidity gradient along the height and the reversible hygroscopic strain within the membrane. Meanwhile, our experiments highlight the critical role of nano-wrinkle structures in enabling MXene/NP membranes to generate sufficient hygroscopic strain. By coupling a moisture diffusion model with the Euler–Bernoulli beam theory, the governing mechanical equation underlying the oscillation dynamics was established. Furthermore, three dimensionless parameters derived from the Buckingham Pi theorem provide a framework for solving this governing equation through finite element analysis. Parametric studies reveal that the oscillation behavior is primarily governed by the aspect ratio of the membrane, the ratio between the moisture diffusion timescale and the oscillation timescale, and the maximum non-uniform strain achievable under the humidity gradient. Despite their distinct chemical compositions, the oscillation behaviors of MXene/NP and GO/SA membranes are successfully predicted, underscoring both the validity and universality of our model. Importantly, because the governing equations for mass and heat transfer share the same mathematical form, our findings extend beyond hygroscopic oscillations to thermally driven oscillations. These insights not only establish a robust mechanics-based approach for predicting and controlling oscillatory behavior but also highlight the significant potential of SNA membranes in actuators and energy harvesting applications.

- The oscillatory behavior of SNA membranes was successfully applied to a fluke-

inspired propeller and a hand moisture-driven nanogenerator. Guided by the theoretical framework established in the previous section, device performance was optimized; notably, the improved membranes were still able to generate a detectable electromotive force under the weak humidity released from a human palm. However, it was also observed that the oscillation of SNA membranes could not be sustained permanently. This decaying phenomenon was attributed to different mechanisms: oxidation in MXene/NP membranes and hygroscopic saturation in GO/SA membranes. From a mechanical perspective, the theoretical model presented earlier further explains why membranes undergoing oxidation or saturation can no longer sustain oscillations. These findings not only provide practical guidelines for optimizing SNA membranes in propulsion and nanogenerator applications but also establish a theoretical basis for future strategies aimed at enhancing oxidation resistance and delaying hygroscopic saturation while maintaining or even improving the membranes' humidity-responsive capability.

7.2 Future work

7.2.1 Enhancement of the applicability of the bilayer theoretical model

The current theoretical model for predicting the deformation of bilayer membranes is derived under the assumption that the active layer is much thinner than the inert layer. In realistic applications, however, the active and inert layers may have comparable

thicknesses, which limits the applicability of the existing model. Future efforts should therefore focus on extending the model to account for a broader range of thickness ratios, thereby enhancing its predictive capability for practical systems. Furthermore, discrepancies observed between theoretical predictions and finite element simulations become more pronounced at higher curvatures. This deviation has been traced primarily to differences in the geometric treatment of large deformations within the two approaches. A systematic investigation is needed to determine the conditions under which either the theoretical or numerical results are more reliable. Another critical direction lies in incorporating fracture criteria into both the theoretical and finite element models. Neither framework currently considers failure under excessive deformation, which is highly relevant for practical applications where membrane integrity is crucial. Finally, Chapter 4 revealed that the stability of bilayer membranes decreases with the reduction of the inert layer modulus. This trend, while theoretically sound, still requires extensive experimental validation. Future studies should therefore aim to systematically test this prediction and quantify its implications for the design of robust bilayer actuators.

7.2.2 Validation of the wrinkle-induced hygroscopic in-plane expansion

In Chapter 5, the in-plane expansion of MXene/NP membranes upon moisture absorption was attributed to the flattening of nanowrinkles on MXene flakes. This mechanism has been partially supported by experimental evidence, where membranes

with reduced wrinkle density—achieved via a confined dehydration process—exhibited decreased swelling strains under the same humidity. In addition, molecular dynamics simulations conducted by our coworkers further corroborated this hypothesis. Nevertheless, the most direct validation of this mechanism is still lacking. Specifically, in situ characterization of the wrinkle-flattening process during moisture absorption is needed to provide conclusive evidence. Future work should therefore focus on developing and employing advanced in situ techniques to directly visualize this dynamic structural evolution. Once established, such evidence, combined with the existing experimental and simulation results, would provide a comprehensive and robust proof of the proposed wrinkle-flattening mechanism.

7.2.3 Performance enhancement of propeller and nanogenerator

In Chapter 6, MXene/NP and GO/SA membranes were successfully applied to moisture-driven propellers and nanogenerators, guided by the proposed theoretical models. However, the major limitation of both devices lies in their short operational lifetime: MXene/NP membranes are prone to oxidation, while GO/SA membranes suffer from moisture saturation. Therefore, future research should focus on improving the oxidation resistance and anti-saturation capability of these hygroscopic membranes without compromising their oscillation performance, in order to enhance their practical applicability. Moreover, the overall performance of these devices remains inferior to other reported prototypes. For instance, the prototype actuator exhibited significantly lower propulsion speed than state-of-the-art light-driven counterparts (with a typical

oscillation frequency of ~6 Hz [186]) and required water pre-heating to 40 °C, which undermines overall energy efficiency, and the actuation force and efficiency of the propeller should be recorded and improved. For the nanogenerator, two key issues must be addressed: (i) the oscillation speed of the membrane remains limited, resulting in a low induced voltage that is insufficient to power common electronic devices (e.g., LEDs); and (ii) the poor electrical conductivity of GO/SA membranes restricts the magnitude of the induced current. To overcome these challenges, future efforts should aim to optimize the geometry and physical properties of the membranes to accelerate oscillation and to incorporate conductive nanomaterials (such as graphene or carbon nanotubes) into the GO/SA membranes to enhance conductivity without impairing their hygroscopic actuation.

7.2.4 Influence of flake size and nanoparticle on MXene/NP membranes

Previous studies have demonstrated that the lateral size of MXene flakes strongly influences their mechanical and electrical properties, with larger flakes exhibiting enhanced Young's modulus, tensile strength, and conductivity [187]. This raises an intriguing question of whether flake size could also significantly affect the hygroscopic response of MXene/NP membranes. If the mechanical properties and the hygroscopic expansion coefficient can be simultaneously improved, larger deformations could be achieved under the same humidity conditions, while the increased tensile strength would mitigate fracture risks during large-strain actuation. In addition to flake size, the

type and size of nanoparticles also represent important research directions. In this work, Fe_3O_4 nanoparticles with an average diameter of 100 nm were employed. It is known that capillary forces between MXene flakes and nanoparticles tend to draw the flakes closer together, which appears to contradict our proposed mechanism that absorbed water flattens the wrinkles. To address this, our collaborators used molecular dynamics simulations to reveal that the apparent contradiction arises from nanoparticle size: small nanoparticles facilitate wrinkle flattening upon hydration, while large nanoparticles reinforce wrinkle formation. Experimental validation of this prediction remains essential. Furthermore, other widely used nanoparticles such as SiO_2 and Al_2O_3 will be surface functionalized for enhanced hydrophilicity and incorporated into MXene membranes to systematically examine the role of nanoparticle chemistry and composition on the hygroscopic response.

References

1. Dawson, C., Vincent, J.F.V., Rocca, A.-M. How pine cones open. *Nature*. 1997;390(6661):668-668. https://doi.org/10.1038/37745

2. Elbaum, R., Zaltzman, L., Burgert, I., Fratzl, P. The role of wheat awns in the seed dispersal unit. *Science*. 2007;316(5826):884-886. https://doi.org/10.1126/science.1140097

3. Reyssat, E., Mahadevan, L. Hygromorphs: From pine cones to biomimetic bilayers. *Journal of The Royal Society Interface*. 2009;6(39):951-957. https://doi.org/10.1098/rsif.2009.0184

4. Armon, S., Efrati, E., Kupferman, R., Sharon, E. Geometry and mechanics in the opening of chiral seed pods. *Science*. 2011;333(6050):1726-1730. https://doi.org/10.1126/science.1203874

5. Yanez, A., Desta, I., Commins, P., Magzoub, M., Naumov, P. Morphokinematics of the hygroactuation of feather grass awns. *Adv. Biosyst.* 2018;2(7):1800007. https://doi.org/https://doi.org/10.1002/adbi.201800007

6. Lin, S., Zhu, J., Li, X., Guo, Y., Fang, Y., Cheng, H., et al. Water-driven actuation of ornithoctonus huwena spider silk fibers. *Appl. Phys. Lett.* 2017;110(5):053103. https://doi.org/10.1063/1.4974350

7. Manikandan, G., Murali, A., Kumar, R., Satapathy, D.K. Rapid moisture-responsive silk fibroin actuators. *ACS Appl. Mater. Interfaces*. 2021;13(7):8880-8888. https://doi.org/10.1021/acsami.0c17525

8. Ha, J., Choi, S.M., Shin, B., Lee, M., Jung, W., Kim, H.-Y. Hygroresponsive coiling of seed awns and soft actuators. *Extreme Mech. Lett.* 2020;38:100746. https://doi.org/https://doi.org/10.1016/j.eml.2020.100746

9. Lindtner, T., Uzan, A.Y., Eder, M., Bar-On, B., Elbaum, R. Repetitive hygroscopic snapping movements in awns of wild oats. *Acta Biomater.* 2021;135:483-492. https://doi.org/https://doi.org/10.1016/j.actbio.2021.08.048

10. Marmottant, P., Ponomarenko, A., Bienaimé, D. The walk and jump of equisetum spores. *Proceedings of the Royal Society B: Biological Sciences*. 2013;280(1770):20131465. https://doi.org/10.1098/rspb.2013.1465

11. Noblin, X., Rojas, N.O., Westbrook, J., Llorens, C., Argentina, M., Dumais, J. The fern sporangium: A unique catapult. *Science*. 2012;335(6074):1322-1322. https://doi.org/10.1126/science.1215985

12. Raven, P.H., Evert, R.F., Eichhorn, S.E. Biology of plants. 7 ed. New York: Macmillan; 2005.

13. Bertinetti, L., Fischer, F.D., Fratzl, P. Physicochemical basis for water-actuated movement and stress generation in nonliving plant tissues. *Phys. Rev. Lett.* 2013;111(23):238001. https://doi.org/10.1103/PhysRevLett.111.238001

14. Abraham, Y., Tamburu, C., Klein, E., Dunlop, J.W.C., Fratzl, P., Raviv, U., et al. Tilted cellulose arrangement as a novel mechanism for hygroscopic coiling in the stork's bill awn. *Journal of The Royal Society Interface*. 2011;9(69):640-647. https://doi.org/10.1098/rsif.2011.0395

15. Aharoni, H., Abraham, Y., Elbaum, R., Sharon, E., Kupferman, R. Emergence of spontaneous twist and curvature in non-euclidean rods: Application to erodium plant cells. *Phys. Rev. Lett.* 2012;108(23):238106. https://doi.org/10.1103/PhysRevLett.108.238106

16.Chen, Z., Majidi, C., Srolovitz, D.J., Haataja, M. Tunable helical ribbons. *Appl. Phys. Lett.* 2011;98(1):011906. https://doi.org/10.1063/1.3530441

17. Bonghi, C., Rascio, N., Ramina, A., Casadoro, G. Cellulase and polygalacturonase involvement in the abscission of leaf and fruit explants of peach. *Plant Mol. Biol.* 1992;20(5):839-848. https://doi.org/10.1007/BF00027155

18. Petersen, M., Sander, L., Child, R., van Onckelen, H., Ulvskov, P., Borkhardt, B. Isolation and characterisation of a pod dehiscence zone-specific polygalacturonase frombrassica napus. *Plant Mol. Biol.* 1996;31(3):517-527. https://doi.org/10.1007/BF00042225

19. Zhang, Z., Liang, Z., Yao, H. Thin-film actuators (tfas): A review. *npj Rob.* 2025;3(1):23. https://doi.org/10.1038/s44182-025-00040-5

20. Lin, S., Wang, Z., Chen, X., Ren, J., Ling, S. Ultrastrong and highly sensitive fiber microactuators constructed by force-reeled silks. *Adv. Sci.* 2020;7(6):1902743. https://doi.org/https://doi.org/10.1002/advs.201902743

21. Boudot, M., Elettro, H., Grosso, D. Converting water adsorption and capillary condensation in usable forces with simple porous inorganic thin films. *ACS Nano*. 2016;10(11):10031-10040. https://doi.org/10.1021/acsnano.6b04648

22. He, Y., Kong, K., Guo, Z., Fang, W., Ma, Z., Pan, H., et al. A highly sensitive, reversible, and bidirectional humidity actuator by calcium carbonate ionic oligomers incorporated poly(vinylidene fluoride). *Adv. Funct. Mater.* 2021;31(26):2101291. https://doi.org/https://doi.org/10.1002/adfm.202101291

23. Chen, W., Yu, H., Lee, S.-Y., Wei, T., Li, J., Fan, Z. Nanocellulose: A promising nanomaterial for advanced electrochemical energy storage. *Chem. Soc. Rev.* 2018;47(8):2837-2872. https://doi.org/10.1039/C7CS00790F

24. Liu, W., Liu, K., Du, H., Zheng, T., Zhang, N., Xu, T., et al. Cellulose nanopaper: Fabrication, functionalization, and applications. *Nano Micro Lett.*

2022;14(1):104. https://doi.org/10.1007/s40820-022-00849-x

25. Odabas, N., Henniges, U., Potthast, A., Rosenau, T. Cellulosic fines: Properties and effects. *Prog. Mater Sci.* 2016;83:574-594. https://doi.org/https://doi.org/10.1016/j.pmatsci.2016.07.006

26. Wang, M., Tian, X., Ras, R.H.A., Ikkala, O. Sensitive humidity-driven reversible and bidirectional bending of nanocellulose thin films as bio-inspired actuation. *Adv. Mater. Interfaces*. 2015;2(7):1500080. https://doi.org/https://doi.org/10.1002/admi.201500080

27. Li, Y., Wang, J., Li, H., Huang, L., Chen, L., Ni, Y., et al. Highly transparent rcf/ptfe humidity and ir light dual-driven actuator with high force density, sensitivity and stability. *Appl. Surf. Sci.* 2022;572:151502. https://doi.org/https://doi.org/10.1016/j.apsusc.2021.151502

28. Zhou, P., Chen, L., Yao, L., Weng, M., Zhang, W. Humidity- and light-driven actuators based on carbon nanotube-coated paper and polymer composite. *Nanoscale*. 2018;10(18):8422-8427. https://doi.org/10.1039/C7NR09580E

29. Wang, S., Yan, S., Zhang, L., Zhao, H., Yang, T., Li, F., et al. Bioinspired poly(vinyl alcohol) film actuator powered by water evaporation under ambient conditions. *Macromol. Mater. Eng.* 2020;305(6):2000145. https://doi.org/https://doi.org/10.1002/mame.202000145

30. Lv, C., Xia, H., Shi, Q., Wang, G., Wang, Y.-S., Chen, Q.-D., et al. Sensitively humidity-driven actuator based on photopolymerizable peg-da films. *Adv. Mater. Interfaces*. 2017;4(9):1601002. https://doi.org/https://doi.org/10.1002/admi.201601002

31. Zheng, Q., Jiang, Z., Xu, X., Xu, C., Zhu, M., Chen, C., et al. Bio-inspired bicomponent fiber with multistimuli response to infrared light and humidity for smart actuators. *ACS Appl. Polym. Mater.* 2021;3(6):3131-3141. https://doi.org/10.1021/acsapm.1c00335

32. VahidMohammadi, A., Rosen, J., Gogotsi, Y. The world of two-dimensional carbides and nitrides (MXenes). *Science*. 2021;372(6547):eabf1581. https://doi.org/10.1126/science.abf1581

33. Liu, B., Xie, J., Ma, H., Zhang, X., Pan, Y., Lv, J., et al. From graphite to graphene oxide and graphene oxide quantum dots. *Small*. 2017;13(18):1601001. https://doi.org/https://doi.org/10.1002/smll.201601001

34. Cheng, H., Zhao, F., Xue, J., Shi, G., Jiang, L., Qu, L. One single graphene oxide film for responsive actuation. *ACS Nano*. 2016;10(10):9529-9535. https://doi.org/10.1021/acsnano.6b04769

35. Cai, G., Ciou, J.-H., Liu, Y., Jiang, Y., Lee, P.S. Leaf-inspired multiresponsive

MXene-based actuator for programmable smart devices. *Sci. Adv.* 2019;5(7):eaaw7956. https://doi.org/10.1126/sciadv.aaw7956

36. Wei, Y., Zhang, P., Soomro, R.A., Zhu, Q., Xu, B. Advances in the synthesis of 2D MXenes. *Adv. Mater.* 2021;33(39):2103148. https://doi.org/https://doi.org/10.1002/adma.202103148

37. Wyatt, B.C., Rosenkranz, A., Anasori, B. 2D MXenes: Tunable mechanical and tribological properties. *Adv. Mater.* 2021;33(17):2007973. https://doi.org/https://doi.org/10.1002/adma.202007973

38. Fennimore, A.M., Yuzvinsky, T.D., Han, W.-Q., Fuhrer, M.S., Cumings, J., Zettl, A. Rotational actuators based on carbon nanotubes. *Nature*. 2003;424(6947):408-410. https://doi.org/10.1038/nature01823

39. Zhang, L., Zhang, Y., Li, F., Yan, S., Wang, Z., Fan, L., et al. Water-evaporation-powered fast actuators with multimodal motion based on robust nacre-mimetic composite film. *ACS Appl. Mater. Interfaces*. 2019;11(13):12890-12897. https://doi.org/10.1021/acsami.9b01912

40. Castaldo, R., Lama, G.C., Aprea, P., Gentile, G., Ambrogi, V., Lavorgna, M., et al. Humidity-driven mechanical and electrical response of graphene/cloisite hybrid films. *Adv. Funct. Mater.* 2019;29(14):1807744. https://doi.org/https://doi.org/10.1002/adfm.201807744

41. Gao, X., Zhang, L., Wang, S., Yang, T., Li, H. Soft untethered robots and grippers based on humidity-gated magnetic-responsive film actuators. *ACS Appl. Polym. Mater.* 2021;3(9):4726-4734. https://doi.org/10.1021/acsapm.1c00978

42. Wang, S., Gao, Y., Wei, A., Xiao, P., Liang, Y., Lu, W., et al. Asymmetric elastoplasticity of stacked graphene assembly actualizes programmable untethered soft robotics. *Nat. Commun.* 2020;11(1):4359. https://doi.org/10.1038/s41467-020-18214-0

43. Lin, J., Zhou, P., Wen, Z., Zhang, W., Luo, Z., Chen, L. Chinese ink: A programmable, dual-responsive and self-sensing actuator using a healing–assembling method. *Nanoscale*. 2021;13(47):20134-20143. https://doi.org/10.1039/D1NR06111A

44. Zhou, J., Zhang, Y., Zhang, J., Zhang, D., Zhou, X., Xiong, J. Breathable metal–organic framework enhanced humidity-responsive nanofiber actuator with autonomous triboelectric perceptivity. *ACS Nano*. 2023;17(18):17920-17930. https://doi.org/10.1021/acsnano.3c04022

45. He, J., Xiao, P., Zhang, J., Liu, Z., Wang, W., Qu, L., et al. Highly efficient actuator of graphene/polydopamine uniform composite thin film driven by moisture gradients. *Adv. Mater. Interfaces*. 2016;3(14):1600169. https://doi.org/https://doi.org/10.1002/admi.201600169

46. Weng, X., Weng, Z., Qin, M., Zhang, J., Wu, Y., Jiang, H. Bioinspired moisture-driven soft actuators based on MXene/aramid nanofiber nanocomposite films. *ACS Appl. Nano Mater.* 2024;7(5):5587-5597. https://doi.org/10.1021/acsanm.4c00420

47. Li, L., Jia, G., Huang, W., Zhou, J., Li, C., Han, J., et al. Multi-responsive soft actuator with integrated ultrasensitive sensing performances for human motion detection and soft robots. *Sens. Actuators, A.* 2023;351:114149. https://doi.org/https://doi.org/10.1016/j.sna.2022.114149

48. Tan, Y., Liu, Z., Liu, Z., Jiang, J., Li, G. Shape-memory-effect-enabled programmable moisture- and acetone-responsive actuation of an janus polymer film. *Chem. Eng. J.* 2023;454:140270. https://doi.org/https://doi.org/10.1016/j.cej.2022.140270

49. Li, B., Duan, X., Cheng, D., Chen, X., Gao, Z., Ren, W., et al. Controllable transition metal-directed assembly of $[Mo_2O_2S_2]^{2+}$ building blocks into smart molecular humidity-responsive actuators. *Journal of the American Chemical Society*. 2023;145(4):2243-2251. https://doi.org/10.1021/jacs.2c10225

50. Ge, F., Lu, X., Xiang, J., Tong, X., Zhao, Y. An optical actuator based on gold-nanoparticle-containing temperature-memory semicrystalline polymers. *Angew. Chem. Int. Ed.* 2017;56(22):6126-6130. https://doi.org/10.1002/anie.201612164

51. Tang, X.-Y., Liu, Z., Xie, R., Ju, X.-J., Wang, W., Chu, L.-Y. Humidity-responsive actuators based on firm heterojunction of glycerol-cross-linked polyvinyl alcohol and porous polyvinylidene fluoride as smart gates for anti-condensation. *Industrial & Engineering Chemistry Research*. 2022;61(23):8101-8111. https://doi.org/10.1021/acs.iecr.2c01289

52. Xuan, J., Wang, Z., Chen, Y., Liang, D., Cheng, L., Yang, X., et al. Organic-base-driven intercalation and delamination for the production of functionalized titanium carbide nanosheets with superior photothermal therapeutic performance. *Angew. Chem. Int. Ed.* 2016;55(47):14569-14574. https://doi.org/10.1002/anie.201606643

53. Wang, Q., Liu, Y., Guo, Y., Zhang, L., Zhong, Y., Sui, X., et al. Super-deformed asymmetric actuators: Balance of photothermal and humidity response effects through structural regulation. *ACS Appl. Polym. Mater.* 2023;5(8):6151-6160. https://doi.org/10.1021/acsapm.3c00809

54. Sun, L., Zhao, Q., Che, L., Li, M., Leng, X., Long, Y., et al. Multi-stimuli-responsive weldable bilayer actuator with programmable patterns and 3D shapes. *Adv. Funct. Mater.* 2024;34(8):2311398. https://doi.org/https://doi.org/10.1002/adfm.202311398

55. Umrao, S., Tabassian, R., Kim, J., Nguyen, V.H., Zhou, Q., Nam, S., et al. MXene artificial muscles based on ionically cross-linked $Ti_3C_2T_x$ electrode for kinetic

soft robotics. *Sci. Rob.* 2019;4(33):eaaw7797. https://doi.org/10.1126/scirobotics.aaw7797

56. Gao, Y., Guo, Z., Song, Z., Yao, H. Spiral interface: A reinforcing mechanism for laminated composite materials learned from nature. *J. Mech. Phys. Solids*. 2017;109:252-263. https://doi.org/https://doi.org/10.1016/j.jmps.2017.09.002

57. Chen, Q., Qian, X., Xu, Y., Yang, Y., Wei, Y., Ji, Y. Harnessing the day–night rhythm of humidity and sunlight into mechanical work using recyclable and reprogrammable soft actuators. *ACS Appl. Mater. Interfaces*. 2019;11(32):29290-29297. https://doi.org/10.1021/acsami.9b09324

58. Gao, Y.-Y., Zhang, Y.-L., Han, B., Zhu, L., Dong, B., Sun, H.-B. Gradient assembly of polymer nanospheres and graphene oxide sheets for dual-responsive soft actuators. *ACS Appl. Mater. Interfaces*. 2019;11(40):37130-37138. https://doi.org/10.1021/acsami.9b13412

59. Le Duigou, A., Chabaud, G., Scarpa, F., Castro, M. Bioinspired electro-thermo-hygro reversible shape-changing materials by 4D printing. *Adv. Funct. Mater.* 2019;29(40):1903280. https://doi.org/https://doi.org/10.1002/adfm.201903280

60. Chen, Z., Gao, B., Li, P., Zhao, X., Yan, Q., Liu, Z., et al. Multistimuli-responsive actuators derived from natural materials for entirely biodegradable and programmable untethered soft robots. *ACS Nano*. 2023;17(22):23032-23045. https://doi.org/10.1021/acsnano.3c08665

61. Han, D.-D., Zhang, Y.-L., Liu, Y., Liu, Y.-Q., Jiang, H.-B., Han, B., et al. Bioinspired graphene actuators prepared by unilateral UV irradiation of graphene oxide papers. *Adv. Funct. Mater.* 2015;25(28):4548-4557. https://doi.org/https://doi.org/10.1002/adfm.201501511

62. Wang, J., Liu, Y., Cheng, Z., Xie, Z., Yin, L., Wang, W., et al. Highly conductive MXene film actuator based on moisture gradients. *Angew. Chem. Int. Ed.* 2020;59(33):14029-14033. https://doi.org/10.1002/anie.202003737

63. Pang, X., Lv, J.-a., Zhu, C., Qin, L., Yu, Y. Photodeformable azobenzene-containing liquid crystal polymers and soft actuators. *Adv. Mater.* 2019;31(52):1904224. https://doi.org/https://doi.org/10.1002/adma.201904224

64. Dong, Y., Wang, J., Guo, X., Yang, S., Ozen, M.O., Chen, P., et al. Multi-stimuli-responsive programmable biomimetic actuator. *Nat. Commun.* 2019;10(1):4087. https://doi.org/10.1038/s41467-019-12044-5

65. Song, Y., Qin, S., Gerringer, J., Grunlan, J.C. Unusually fast and large actuation from multilayer polyelectrolyte thin films. *Soft Matter*. 2019;15(11):2311-2314. https://doi.org/10.1039/C8SM02465K

66. Kim, B.K., Kim, Y. Structural robustness and actuation performance of

multilayered thin-film actuators based on ni-co flexible substrate. *Sens. Actuators, A*. 2024;371:115230. https://doi.org/https://doi.org/10.1016/j.sna.2024.115230

67. Wei, S., Ghosh, T.K. Moisture-driven cellulose actuators with directional motion and programmable shapes. *Adv. Intell. Syst.* 2024;6(5):2300638. https://doi.org/https://doi.org/10.1002/aisy.202300638

68. Jiang, X., Chen, K., Long, Y., Liu, S., Chi, Z., Xu, J., et al. Design and synthesis of vertical gradient of expansion structure based on polyimide humidity sensing layer with ultra-fast response, high sensitivity, and large deformation driven by humidity. *Chem. Eng. J.* 2023;468:143805. https://doi.org/https://doi.org/10.1016/j.cej.2023.143805

69. Han, M., Shen, W., Corriou, J.-P. Polydopamine-modified MXene/cellulose nanofibers composite film for self-powered humidity sensing and humidity actuating. *Nano Energy*. 2024;123:109445. https://doi.org/https://doi.org/10.1016/j.nanoen.2024.109445

70. Wei, J., Jia, S., Ma, C., Guan, J., Yan, C., Zhao, L., et al. Nacre-inspired composite film with mechanical robustness for highly efficient actuator powered by humidity gradients. *Chem. Eng. J.* 2023;451:138565. https://doi.org/https://doi.org/10.1016/j.cej.2022.138565

71. Huang, Y., Liu, L., Zhu, X., Wang, H.M., Zhang, L., Wang, S., et al. Nanofiber-based flexible actuator with high transparency and large-scale deformation for biomimetic and intelligent control. *Sens. Actuators, B*. 2024;402:135061. https://doi.org/https://doi.org/10.1016/j.snb.2023.135061

72. Jiang, Y., Hu, C., Cheng, H., Li, C., Xu, T., Zhao, Y., et al. Spontaneous, straightforward fabrication of partially reduced graphene oxide–polypyrrole composite films for versatile actuators. *ACS Nano*. 2016;10(4):4735-4741. https://doi.org/10.1021/acsnano.6b01233

73. Yang, J., Zhang, J., Li, X., Zhou, J., Li, Y., Wang, Z., et al. Single janus iodine-doped rGO/rGO film with multi-responsive actuation and high capacitance for smart integrated electronics. *Nano Energy*. 2018;53:916-925. https://doi.org/https://doi.org/10.1016/j.nanoen.2018.09.044

74. Ma, J.-N., Ma, B., Wang, Z.-X., Song, P., Han, D.-D., Zhang, Y.-L. Multiresponsive MXene actuators with asymmetric quantum-confined superfluidic structures. *Adv. Funct. Mater.* 2024;34(8):2308317. https://doi.org/https://doi.org/10.1002/adfm.202308317

75. Qiu, Y., Wang, M., Zhang, W., Liu, Y., Li, Y.V., Pan, K. An asymmetric graphene oxide film for developing moisture actuators. *Nanoscale*. 2018;10(29):14060-14066. https://doi.org/10.1039/C8NR01785A

76. Zhang, B., Cui, X., He, W., Shao, L., Wang, T., Meng, F., et al. Asymmetric metal–organic framework-based mixed matrix membrane for reversible self-assembling 3D architecture. *ACS Appl. Polym. Mater.* 2023;5(9):7090-7097. https://doi.org/10.1021/acsapm.3c01132

77. Aksu, Z., Şahin, C.H., Alanyalıoğlu, M. Fabrication of janus GO/rGO humidity actuator by one-step electrochemical reduction route. *Sens. Actuators, B*. 2022;354:131198. https://doi.org/https://doi.org/10.1016/j.snb.2021.131198

78. Zhu, X., Yang, C., Jian, Y., Deng, H., Du, Y., Shi, X. Ion-responsive chitosan hydrogel actuator inspired by carrotwood seed pod. *Carbohydr. Polym.* 2022;276:118759. https://doi.org/https://doi.org/10.1016/j.carbpol.2021.118759

79. Cheng, Z., Hua, Y., Zhang, D., Wang, M., Ge, X., Shen, Y., et al. Bilayer oriented nanofiber membrane for enhancing response deformation and stability of humidity-responsive actuator. *Chem. Eng. J.* 2025;506:160260. https://doi.org/https://doi.org/10.1016/j.cej.2025.160260

80. He, S., He, C., Liu, X., Du, C., Jin, X., Chen, Q., et al. Smart bionic applications based on a multiple stimulus response GO-PDANP/PDMS bilayer flexible actuator. *New J. Chem.* 2023;47(48):22205-22214. https://doi.org/10.1039/D3NJ04471H

81. Zhao, T., Dou, W., Hu, Z., Hou, W., Sun, Y., Lv, J.-a. Reconfigurable soft actuators with multiple-stimuli responses. *Macromol. Rapid Commun.* 2020;41(17):2000313. https://doi.org/https://doi.org/10.1002/marc.202000313

82. Lee, S., Lee, M., Lee, J. Highly sensitive humidity-responsive actuator comprising aligned electrospun fibers containing metal–organic framework nanoparticles. *Sens. Actuators, B*. 2021;332:129520. https://doi.org/https://doi.org/10.1016/j.snb.2021.129520

83. Zhao, T., Liu, H., Yuan, L., Tian, X., Xue, X., Li, T., et al. A multi-responsive MXene-based actuator with integrated sensing function. *Adv. Mater. Interfaces*. 2022;9(10):2101948. https://doi.org/https://doi.org/10.1002/admi.202101948

84. Liu, W., Kong, D., Zhao, W., Leng, J. Multi-stimulus responsive shape memory polyurea incorporating stress-mismatching structure for soft actuators and reversible deployable structures. *Compos. Struct.* 2024;334:117966. https://doi.org/https://doi.org/10.1016/j.compstruct.2024.117966

85. Yu, J., Xu, Z., Wan, Q., Shuai, Y., Wang, J., Mao, C., et al. Ultrafast bi-directional bending moisture-responsive soft actuators through superfine silk rod modified bio-mimicking hierarchical layered structure. *Small*. 2024;20(25):2309364. https://doi.org/https://doi.org/10.1002/smll.202309364

86. Yang, Z., An, Y., He, Y., Lian, X., Wang, Y. A programmable actuator as

synthetic earthworm. *Adv. Mater.* 2023;35(36):2303805. https://doi.org/https://doi.org/10.1002/adma.202303805

87. Chang, E.-J., Lin, M.-F. Enhanced actuation performance of multiple stimuli responsive PDMS-based bilayer actuators by adding ionic liquid. *Sens. Actuators, B*. 2024;404:135300. https://doi.org/https://doi.org/10.1016/j.snb.2024.135300

88. Tabassian, R., Kim, J., Nguyen, V.H., Kotal, M., Oh, I.-K. Functionally antagonistic hybrid electrode with hollow tubular graphene mesh and nitrogen-doped crumpled graphene for high-performance ionic soft actuators. *Adv. Funct. Mater.* 2018;28(5):1705714. https://doi.org/https://doi.org/10.1002/adfm.201705714

89. Yang, Z., Wang, Y., Lan, L., Wang, Y., Zhang, X. Bioinspired h-bonding connected gradient nanostructure actuators based on cellulose nanofibrils and graphene. *Small*. 2024;20(36):2401580. https://doi.org/https://doi.org/10.1002/smll.202401580

90. Cai, G., Ciou, J.-H., Liu, Y., Jiang, Y., Lee, P.S. Leaf-inspired multiresponsive MXene-based actuator for programmable smart devices. *Sci. Adv.*;5(7):eaaw7956. https://doi.org/10.1126/sciadv.aaw7956

91. Wang, W., Yao, L., Cheng, C.-Y., Zhang, T., Atsumi, H., Wang, L., et al. Harnessing the hygroscopic and biofluorescent behaviors of genetically tractable microbial cells to design biohybrid wearables. *Sci. Adv.*;3(5):e1601984. https://doi.org/10.1126/sciadv.1601984

92. Li, D., Wang, S., He, J., Zeng, H., Yao, K., Gao, Z., et al. Bioinspired ultrathin piecewise controllable soft robots. *Adv. Mater. Technol.* 2021;6(5):2001095. https://doi.org/https://doi.org/10.1002/admt.202001095

93. Zhang, Y.-L., Li, J.-C., Zhou, H., Liu, Y.-Q., Han, D.-D., Sun, H.-B. Electro-responsive actuators based on graphene. *The Innovation*. 2021;2(4). https://doi.org/10.1016/j.xinn.2021.100168

94. Nguyen, V.H., Tabassian, R., Oh, S., Nam, S., Mahato, M., Thangasamy, P., et al. Stimuli-responsive MXene-based actuators. *Adv. Funct. Mater.* 2020;30(47):1909504. https://doi.org/10.1002/adfm.201909504

95. Feng, X.-F., Sheng, S.-Z., Chen, C., Li, X.-L., Xian, Z.-Y., Liu, J.-W. A multi-stimuli-responsive actuator for efficient thermal management and various biomimetic locomotion. *Cell Rep. Phys. Sci.* 2023;4(10). https://doi.org/10.1016/j.xcrp.2023.101588

96. Yang, L., Cui, J., Zhang, L., Xu, X., Chen, X., Sun, D. A moisture-driven actuator based on polydopamine-modified MXene/bacterial cellulose nanofiber composite film. *Adv. Funct. Mater.* 2021;31(27):2101378. https://doi.org/10.1002/adfm.202101378

97. Li, Z., Gao, C., Fan, S., Zou, J., Gu, G., Dong, M., et al. Cell nanomechanics

based on dielectric elastomer actuator device. *Nano Micro Lett.* 2019;11(1):98. https://doi.org/10.1007/s40820-019-0331-8

98. Ling, Y., Fan, H., Wang, K., Lu, Z., Wang, L., Hou, C., et al. Electrochemical actuators with multicolor changes and multidirectional actuation. *Small*. 2022;18(15):2107778. https://doi.org/https://doi.org/10.1002/smll.202107778

99. Yin, Q., Wang, L., Jiang, J., Dai, C., Weng, G., He, J. Three-dimensional shape transformation of eu^{3+}-containing polymer films through modulating dynamic eu^{3+}-iminodiacetate coordination. *Chem. Mater.* 2022;34(5):2176-2186. https://doi.org/10.1021/acs.chemmater.1c03722

100. Zhang, Y.-L., Liu, Y.-Q., Han, D.-D., Ma, J.-N., Wang, D., Li, X.-B., et al. Quantum-confined-superfluidics-enabled moisture actuation based on unilaterally structured graphene oxide papers. *Adv. Mater.* 2019;31(32):1901585. https://doi.org/10.1002/adma.201901585

101. Truong, T.-A., Nguyen, T.-K., Zhao, H., Nguyen, N.-K., Dinh, T., Park, Y., et al. Engineering stress in thin films: An innovative pathway toward 3D micro and nanosystems. *Small*. 2022;18(4):2105748. https://doi.org/https://doi.org/10.1002/smll.202105748

102. Xu, L., Shyu, T.C., Kotov, N.A. Origami and kirigami nanocomposites. *ACS Nano*. 2017;11(8):7587-7599. https://doi.org/10.1021/acsnano.7b03287

103. Chen, X., Li, Y., Wang, X., Yu, H. Origami paper-based stretchable humidity sensor for textile-attachable wearable electronics. *ACS Appl. Mater. Interfaces*. 2022;14(31):36227-36237. https://doi.org/10.1021/acsami.2c08245

104. Matonis, S.J., Zhuang, B., Bishop, A.F., Naik, D.A., Temel, Z., Bettinger, C.J. Edible origami actuators using gelatin-based bioplastics. *ACS Appl. Polym. Mater.* 2023;5(8):6288-6295. https://doi.org/10.1021/acsapm.3c00919

105. Freund, L.B., Suresh, S. Thin film materials: Stress, defect formation and surface evolution: Cambridge university press; 2004.

106. Wang, M., Li, Q., Shi, J., Cao, X., Min, L., Li, X., et al. Bio-inspired high sensitivity of moisture-mechanical GO films with period-gradient structures. *ACS Appl. Mater. Interfaces*. 2020;12(29):33104-33112. https://doi.org/10.1021/acsami.0c07956

107. Tang, G., Zhao, X., Liu, S., Mei, D., Zhao, C., Li, L., et al. Moisture-driven actuators. *Adv. Funct. Mater.* 2024;35:2412254. https://doi.org/https://doi.org/10.1002/adfm.202412254

108. Nguyen, V.Q., Ahmed, A.S., Ramanujan, R.V. Morphing soft magnetic composites. *Adv. Mater.* 2012;24(30):4041-4054. https://doi.org/https://doi.org/10.1002/adma.201104994

109. Zou, M., Li, S., Hu, X., Leng, X., Wang, R., Zhou, X., et al. Progresses in tensile, torsional, and multifunctional soft actuators. *Adv. Funct. Mater.* 2021;31(39):2007437. https://doi.org/https://doi.org/10.1002/adfm.202007437

110. Cavusoglu, A.-H., Chen, X., Gentine, P., Sahin, O. Potential for natural evaporation as a reliable renewable energy resource. *Nat. Commun.* 2017;8(1):617. https://doi.org/10.1038/s41467-017-00581-w

111. Liu, D., Tarakanova, A., Hsu, C.C., Yu, M., Zheng, S., Yu, L., et al. Spider dragline silk as torsional actuator driven by humidity. *Sci. Adv.*;5(3):eaau9183. https://doi.org/10.1126/sciadv.aau9183

112. Guo, X., Wang, Y., Qin, Y., Shen, P., Peng, Q. Structures, properties and application of alginic acid: A review. *Int. J. Biol. Macromol.* 2020;162:618-628. https://doi.org/https://doi.org/10.1016/j.ijbiomac.2020.06.180

113. Tan, H., Yu, X., Tu, Y., Zhang, L. Humidity-driven soft actuator built up layer-by-layer and theoretical insight into its mechanism of energy conversion. *The Journal of Physical Chemistry Letters*. 2019;10(18):5542-5551. https://doi.org/10.1021/acs.jpclett.9b02249

114. Yuan, R., Lu, G., Yang, N., You, D., Wang, J., Zhang, Q., et al. Self-healing lbl dual ambiences-driven molecular gating-based unidirectional actuators for multi-mode personal protection. *Chem. Eng. J.* 2022;434:134212. https://doi.org/https://doi.org/10.1016/j.cej.2021.134212

115. Chen, Q., Sochor, B., Chumakov, A., Betker, M., Ulrich, N.M., Toimil-Molares, M.E., et al. Cellulose-reinforced programmable and stretch-healable actuators for smart packaging. *Adv. Funct. Mater.* 2022;32(49):2208074. https://doi.org/https://doi.org/10.1002/adfm.202208074

116. Bai, L., Zhang, Y., Guo, S., Qu, H., Yu, Z., Yu, H., et al. Hygrothermic wood actuated robotic hand. *Adv. Mater.* 2023;35(22):2211437. https://doi.org/https://doi.org/10.1002/adma.202211437

117. Chen, X., Goodnight, D., Gao, Z., Cavusoglu, A.H., Sabharwal, N., DeLay, M., et al. Scaling up nanoscale water-driven energy conversion into evaporation-driven engines and generators. *Nat. Commun.* 2015;6(1):7346. https://doi.org/10.1038/ncomms8346

118. Ge, Y., Zeng, J., Hu, B., Yang, D.-Y., Shao, Y., Lu, H. Bioinspired flexible film as intelligent moisture-responsive actuators and noncontact sensors. *Giant*. 2022;11:100107. https://doi.org/https://doi.org/10.1016/j.giant.2022.100107

119. Ma, B., Ma, J.-N., Song, P., Wang, K., Zhang, D.-M., Li, Q., et al. Quantum-confined-superfluidics-enabled multiresponsive MXene-based actuators. *ACS Appl. Mater. Interfaces*. 2024;16(12):15215-15226.

https://doi.org/10.1021/acsami.4c00864

120. Chathuranga, H., Marriam, I., Chen, S., Zhang, Z., MacLeod, J., Liu, Y., et al. Multistimulus-responsive graphene oxide/Fe_3O_4/starch soft actuators. *ACS Appl. Mater. Interfaces*. 2022;14(14):16772-16779. https://doi.org/10.1021/acsami.2c03486

121. Lan, R., Gao, Y., Shen, C., Huang, R., Bao, J., Zhang, Z., et al. Humidity-responsive liquid crystalline network actuator showing synergistic fluorescence color change enabled by aggregation induced emission luminogen. *Adv. Funct. Mater.* 2021;31(17):2010578. https://doi.org/https://doi.org/10.1002/adfm.202010578

122. Yang, X., Lan, L., Pan, X., Di, Q., Liu, X., Li, L., et al. Bioinspired soft robots based on organic polymer-crystal hybrid materials with response to temperature and humidity. *Nat. Commun.* 2023;14(1):2287. https://doi.org/10.1038/s41467-023-37964-1

123. Dong, Y., Wang, L., Xia, N., Wang, Y., Wang, S., Yang, Z., et al. Multi-stimuli-response programmable soft actuators with site-specific and anisotropic deformation behavior. *Nano Energy*. 2021;88:106254. https://doi.org/https://doi.org/10.1016/j.nanoen.2021.106254

124. Chen, Z., Peng, Q., Hu, Y., Liu, Z., Zhao, X., Li, P., et al. Dried bonito flakes-inspired moisture-responsive actuator with a gradient structure for smart devices. *J. Mater. Sci. Technol.* 2023;167:152-160. https://doi.org/10.1016/j.jmst.2023.05.050

125. Zheng, X., Guan, S., Zhang, C., Qu, T., Wen, W., Zhao, Y., et al. A cut-and-weld process to 3D architectures from multiresponsive crosslinked liquid crystalline polymers. *Small*. 2019;15(16):1900110. https://doi.org/https://doi.org/10.1002/smll.201900110

126. Li, J., Wang, M., Cui, Z., Liu, S., Feng, D., Mei, G., et al. Dual-responsive jumping actuators by light and humidity. *J. Mater. Chem. A*. 2022;10(47):25337-25346. https://doi.org/10.1039/D2TA07339K

127. Xue, E., Tian, B., Wu, Y., Liu, Q., Guo, P., Zheng, K., et al. Photothermal and humidity stimulus-responsive self-sensing soft actuators for smart packaging. *ACS Appl. Polym. Mater.* 2023;5(6):4525-4535. https://doi.org/10.1021/acsapm.3c00627

128. Yang, L., Zhang, L., Cui, J., Sun, D. Tailoring MXene-based films as moisture-responsive actuators for continuous energy conversion. *J. Mater. Chem. A*. 2022;10(29):15785-15793. https://doi.org/10.1039/D2TA03756D

129. Chen, X., Mahadevan, L., Driks, A., Sahin, O. Bacillus spores as building blocks for stimuli-responsive materials and nanogenerators. *Nat. Nanotechnol.* 2014;9(2):137-141. https://doi.org/10.1038/nnano.2013.290

130. Chen, J., Oh, S.K., Zou, H., Shervin, S., Wang, W., Pouladi, S., et al. High-output lead-free flexible piezoelectric generator using single-crystalline GaN thin film.

ACS Appl. Mater. Interfaces. 2018;10(15):12839-12846. https://doi.org/10.1021/acsami.8b01281

131. Wang, G., Xia, H., Sun, X.-C., Lv, C., Li, S.-X., Han, B., et al. Actuator and generator based on moisture-responsive PEDOT: PSS/PVDF composite film. *Sens. Actuators, B*. 2018;255:1415-1421. https://doi.org/https://doi.org/10.1016/j.snb.2017.08.125

132. Li, P., Su, N., Wang, Z., Qiu, J. A $Ti_3C_2T_x$ MXene-based energy-harvesting soft actuator with self-powered humidity sensing and real-time motion tracking capability. *ACS Nano*. 2021;15(10):16811-16818. https://doi.org/10.1021/acsnano.1c07186

133. Wang, H., Cheng, H., Huang, Y., Yang, C., Wang, D., Li, C., et al. Transparent, self-healing, arbitrary tailorable moist-electric film generator. *Nano Energy*. 2020;67:104238. https://doi.org/https://doi.org/10.1016/j.nanoen.2019.104238

134. Liu, Q., Xue, Y., He, J., Li, J., Mu, L., Zhao, Y., et al. Highly moisture-resistant flexible thin-film-based triboelectric nanogenerator for environmental energy harvesting and self-powered tactile sensing. *ACS Appl. Mater. Interfaces*. 2024;16(29):38269-38282. https://doi.org/10.1021/acsami.4c08188

135. Shen, D., Duley, W.W., Peng, P., Xiao, M., Feng, J., Liu, L., et al. Moisture-enabled electricity generation: From physics and materials to self-powered applications. *Adv. Mater.* 2020;32(52):2003722. https://doi.org/https://doi.org/10.1002/adma.202003722

136. Liu, D., Liu, J., Yang, M., Cui, N., Wang, H., Gu, L., et al. Performance enhanced triboelectric nanogenerator by taking advantage of water in humid environments. *Nano Energy*. 2021;88:106303. https://doi.org/https://doi.org/10.1016/j.nanoen.2021.106303

137. Feng, J.-C., Li, S.-X., Zhang, Z.-P., An, Y., Gao, Q.-S., Sun, Z., et al. High output power moist-electric generator based on synergistic nanoarchitectonics for effective ion regulation. *Nano Energy*. 2024;119:109103. https://doi.org/https://doi.org/10.1016/j.nanoen.2023.109103

138. Maity, D., Fussenegger, M. An efficient ambient-moisture–driven wearable electrical power generator. *Adv. Sci.* 2023;10(22):2300750. https://doi.org/https://doi.org/10.1002/advs.202300750

139. Zhan, L., Lv, J., Chen, S., Gupta, A., Xin, Y., Jiang, F., et al. Moisture-triggered hybrid soft actuator and electric generator for self-sensing wearables and adaptive human-environment interaction. *Nano Energy*. 2024;132:110410. https://doi.org/10.1016/j.nanoen.2024.110410

140. Suzuki, D., Oda, S., Kawano, Y. A flexible and wearable terahertz scanner.

Nat. Photonics. 2016;10(12):809-813. https://doi.org/10.1038/nphoton.2016.209

141. Li, J., Yang, P., Li, X., Jiang, C., Yun, J., Yan, W., et al. Ultrathin smart energy-storage devices for skin-interfaced wearable electronics. *ACS Energy Lett.* 2023;8(1):1-8. https://doi.org/10.1021/acsenergylett.2c02029

142. Wei, J., Jia, S., Wei, J., Ma, C., Shao, Z. Tough and multifunctional composite film actuators based on cellulose nanofibers toward smart wearables. *ACS Appl. Mater. Interfaces*. 2021;13(32):38700-38711. https://doi.org/10.1021/acsami.1c09653

143. Jia, T., Wang, Y., Dou, Y., Li, Y., Jung de Andrade, M., Wang, R., et al. Moisture sensitive smart yarns and textiles from self-balanced silk fiber muscles. *Adv. Funct. Mater.* 2019;29(18):1808241. https://doi.org/https://doi.org/10.1002/adfm.201808241

144. Wang, J., Liu, Y., Cheng, Z., Xie, Z., Yin, L., Wang, W., et al. Highly conductive MXene film actuator based on moisture gradients. *Angew. Chem. Int. Ed.* 2020;59(33):14029-14033. https://doi.org/https://doi.org/10.1002/anie.202003737

145. VahidMohammadi, A., Rosen, J., Gogotsi, Y. The world of two-dimensional carbides and nitrides (MXenes). *Science*. 2021;372(6547). https://doi.org/10.1126/science.abf1581

146. Alhabeb, M., Maleski, K., Anasori, B., Lelyukh, P., Clark, L., Sin, S., et al. Guidelines for synthesis and processing of two-dimensional titanium carbide ($Ti_3C_2T_x$ MXene). *Chem. Mater.* 2017;29(18):7633-7644. https://doi.org/10.1021/acs.chemmater.7b02847

147. Hu, H., Wang, Z., Pan, L., Zhao, S., Zhu, S. Ag-coated Fe_3O_4@SiO_2 three-ply composite microspheres: Synthesis, characterization, and application in detecting melamine with their surface-enhanced raman scattering. *J. Phys. Chem. C*. 2010;114(17):7738-7742. https://doi.org/10.1021/jp100141c

148. Gao, Y., Xie, Y., Wei, A., Wei, Y., Chen, T., Yao, H. Tension-compression asymmetry of the stress-strain behavior of the stacked graphene assembly: Experimental measurement and theoretical interpretation. *J. Mech. Phys. Solids*. 2021;157:104642. https://doi.org/10.1016/j.jmps.2021.104642

149. Stöber, W., Fink, A., Bohn, E. Controlled growth of monodisperse silica spheres in the micron size range. *J. Colloid Interface Sci.* 1968;26(1):62-69. https://doi.org/https://doi.org/10.1016/0021-9797(68)90272-5

150. Carmeliet, J., Hens, H., Roels, S., Adan, O., Brocken, H., Cerny, R., et al. Determination of the liquid water diffusivity from transient moisture transfer experiments. *J. Therm. Envelope Build. Sci.* 2004;27(4):277-305. https://doi.org/10.1177/1097196304042324

151. Thompson, J.O. Hooke's law. *Science*. 1926;64(1656):298-299. https://doi.org/10.1126/science.64.1656.298

152. Zhang, Z., Li, X., Yin, J., Xu, Y., Fei, W., Xue, M., et al. Emerging hydrovoltaic technology. *Nat. Nanotechnol.* 2018;13(12):1109-1119. https://doi.org/10.1038/s41565-018-0228-6

153. Lee, S.-W., Prosser, J.H., Purohit, P.K., Lee, D. Bioinspired hygromorphic actuator exhibiting controlled locomotion. *ACS Macro Lett.* 2013;2(11):960-965. https://doi.org/10.1021/mz400439a

154. Qi, L., Kong, L., Wang, Y., Song, J., Azam, A., Zhang, Z., et al. Recent progress in application-oriented self-powered microelectronics. *Adv. Energy Mater.* 2023;13(47):2302699. https://doi.org/10.1002/aenm.202302699

155. Yang, Y., Shen, Y. Light-driven carbon-based soft materials: Principle, robotization, and application. *Adv. Opt. Mater.* 2021;9(12):2100035. https://doi.org/10.1002/adom.202100035

156. Yang, Y., Zhang, M., Li, D., Shen, Y. Graphene-based light-driven soft robot with snake-inspired concertina and serpentine locomotion. *Adv. Mater. Technol.* 2019;4(1):1800366. https://doi.org/10.1002/admt.201800366

157. Sang, W., Zhao, L., Tang, R., Wu, Y., Zhu, C., Liu, J. Electrothermal actuator on graphene bilayer film. *Macromol. Mater. Eng.* 2017;302(12):1700239. https://doi.org/10.1002/mame.201700239

158. Taseer, A.K., Oh, S., Kim, J.-S., Garai, M., Yoo, H., Nguyen, V.H., et al. Cobalt MOF-based porous carbonaceous spheres for multimodal soft actuator exhibiting intricate biomimetic motions. *Adv. Mater.* 2024;36(26):2312340. https://doi.org/10.1002/adma.202312340

159. Acome, E., Mitchell, S.K., Morrissey, T.G., Emmett, M.B., Benjamin, C., King, M., et al. Hydraulically amplified self-healing electrostatic actuators with muscle-like performance. *Science*. 2018;359(6371):61-65. https://doi.org/10.1126/science.aao6139

160. Zhao, L., Fu, X., Xu, H., Zheng, Y., Han, W., Wang, L. Tissue-like sodium alginate-coated 2D MXene-based flexible temperature sensors for full-range temperature monitoring. *Adv. Mater. Technol.* 2022;7(10):2101740. https://doi.org/10.1002/admt.202101740

161. Luo, D., Maheshwari, A., Danielescu, A., Li, J., Yang, Y., Tao, Y., et al. Autonomous self-burying seed carriers for aerial seeding. *Nature*. 2023;614(7948):463-470. https://doi.org/10.1038/s41586-022-05656-3

162. Li, J., Guo, W., Zhao, W., Zhu, Y., Bai, J., Xia, Z., et al. Recent advances in flexible self-oscillating actuators. *eScience*. 2024;4(5):100250.

https://doi.org/10.1016/j.esci.2024.100250

163. Ma, M., Guo, L., Anderson, D.G., Langer, R. Bio-inspired polymer composite actuator and generator driven by water gradients. *Science*. 2013;339(6116):186-189. https://doi.org/10.1126/science.1230262

164. Tan, J., Fang, S., Zhang, Z., Yin, J., Li, L., Wang, X., et al. Self-sustained electricity generator driven by the compatible integration of ambient moisture adsorption and evaporation. *Nat. Commun.* 2022;13(1):3643. https://doi.org/10.1038/s41467-022-31221-7

165. Yu, M., Zhou, S., Wang, Z., Zhao, J., Qiu, J. Boosting electrocatalytic oxygen evolution by synergistically coupling layered double hydroxide with MXene. *Nano Energy*. 2018;44:181-190. https://doi.org/10.1016/j.nanoen.2017.12.003

166. Pang, W., Xu, S., Liu, L., Bo, R., Zhang, Y. Thin-film-shaped flexible actuators. *Adv. Intell. Syst.* 2023;5(8):2300060. https://doi.org/doi.org/10.1002/aisy.202300060

167. Boley, B.A. Thermally induced vibrations of beams. *J. Astronaut. Sci.* 1956;23(2):179-181. https://doi.org/10.2514/8.3527

168. Ghidiu, M., Kota, S., Drozd, V., Barsoum, M.W. Pressure-induced shear and interlayer expansion in Ti_3C_2 MXene in the presence of water. *Sci. Adv.* 2018;4(1):eaao6850. https://doi.org/10.1126/sciadv.aao6850

169. Bauchau, O.A., Craig, J.I. Euler-bernoulli beam theory. In: Bauchau OA, Craig JI, editors. Structural analysis. Dordrecht: Springer Netherlands; 2009. p. 173-221.

170. Evans, J.H. Dimensional analysis and the buckingham pi theorem. *Am. J. Phys.* 1972;40(12):1815-1822. https://doi.org/10.1119/1.1987069

171. Han, M., Yin, X., Wu, H., Hou, Z., Song, C., Li, X., et al. Ti_3C_2 MXenes with modified surface for high-performance electromagnetic absorption and shielding in the x-band. *ACS Appl. Mater. Interfaces*. 2016;8(32):21011-21019. https://doi.org/10.1021/acsami.6b06455

172. Anasori, B., Xie, Y., Beidaghi, M., Lu, J., Hosler, B.C., Hultman, L., et al. Two-dimensional, ordered, double transition metals carbides (MXenes). *ACS Nano*. 2015;9(10):9507-9516. https://doi.org/10.1021/acsnano.5b03591

173. Zou, G., Zhang, Z., Guo, J., Liu, B., Zhang, Q., Fernandez, C., et al. Synthesis of MXene/ag composites for extraordinary long cycle lifetime lithium storage at high rates. *ACS Appl. Mater. Interfaces*. 2016;8(34):22280-22286. https://doi.org/10.1021/acsami.6b08089

174. Meng, R., Huang, J., Feng, Y., Zu, L., Peng, C., Zheng, L., et al. Black

phosphorus quantum dot/Ti3C2 MXene nanosheet composites for efficient electrochemical lithium/sodium-ion storage. *Adv. Energy Mater.* 2018;8(26):1801514. https://doi.org/https://doi.org/10.1002/aenm.201801514

175. Wang, Q., Wu, Z., Li, J., Wei, J., Guo, J., Yin, M. Spontaneous and continuous actuators driven by fluctuations in ambient humidity for energy-harvesting applications. *ACS Appl. Mater. Interfaces*. 2022;14(34):38972-38980. https://doi.org/10.1021/acsami.2c11944

176. Sun, L., Che, L., Li, M., Chen, K., Leng, X., Long, Y., et al. Reinforced nacre-like MXene/sodium alginate composite films for bioinspired actuators driven by moisture and sunlight. *Small*. 2024;20(51):2406832. https://doi.org/https://doi.org/10.1002/smll.202406832

177. Tang, G., Zhao, C., Zhao, X., Mei, D., Pan, Y., Li, B., et al. Nafion/polyimide based programmable moisture-driven actuators for functional structures and robots. *Sens. Actuators, B*. 2023;393:134152. https://doi.org/https://doi.org/10.1016/j.snb.2023.134152

178. Yao, Y., Yin, C., Hong, S., Chen, H., Shi, Q., Wang, J., et al. Lanthanide-ion-coordinated supramolecular hydrogel inks for 3D printed full-color luminescence and opacity-tuning soft actuators. *Chem. Mater.* 2020;32(20):8868-8876. https://doi.org/10.1021/acs.chemmater.0c02448

179. Ma, C.-B., Shang, X., Sun, M., Bo, X., Bai, J., Du, Y., et al. Emerging multifunctional wearable sensors: Integrating multimodal sweat analysis and advanced material technologies for next-generation health monitoring. *ACS Sens.* 2025;10(4):2388-2408. https://doi.org/10.1021/acssensors.4c03396

180. Xu, T., Ding, X., Shao, C., Song, L., Lin, T., Gao, X., et al. Electric power generation through the direct interaction of pristine graphene-oxide with water molecules. *Small*. 2018;14(14):1704473. https://doi.org/https://doi.org/10.1002/smll.201704473

181. Kim, H., Kwon, S. Water-responsive polymer composites on the move. *Science*. 2013;339(6116):150-151. https://doi.org/10.1126/science.1232733

182. Arazoe, H., Miyajima, D., Akaike, K., Araoka, F., Sato, E., Hikima, T., et al. An autonomous actuator driven by fluctuations in ambient humidity. *Nat. Mater.* 2016;15(10):1084-1089. https://doi.org/10.1038/nmat4693

183. Handoko, A.D., Fredrickson, K.D., Anasori, B., Convey, K.W., Johnson, L.R., Gogotsi, Y., et al. Tuning the basal plane functionalization of two-dimensional metal carbides (MXenes) to control hydrogen evolution activity. *ACS Appl. Energy Mater.* 2018;1(1):173-180. https://doi.org/10.1021/acsaem.7b00054

184. Seh, Z.W., Fredrickson, K.D., Anasori, B., Kibsgaard, J., Strickler, A.L.,

Lukatskaya, M.R., et al. Two-dimensional molybdenum carbide (MXene) as an efficient electrocatalyst for hydrogen evolution. *ACS Energy Lett.* 2016;1(3):589-594. https://doi.org/10.1021/acsenergylett.6b00247

185. Gao, G., O'Mullane, A.P., Du, A. 2D MXenes: A new family of promising catalysts for the hydrogen evolution reaction. *ACS Catal.* 2017;7(1):494-500. https://doi.org/10.1021/acscatal.6b02754

186. Zhao, Y., Liu, Z., Shi, P., Chen, C., Alsaid, Y., Yan, Y., et al. Antagonistic-contracting high-power photo-oscillators for multifunctional actuations. *Nat. Mater.* 2025;24(1):116-124. https://doi.org/10.1038/s41563-024-02035-3

187. Wan, S., Li, X., Chen, Y., Liu, N., Wang, S., Du, Y., et al. Ultrastrong MXene films via the synergy of intercalating small flakes and interfacial bridging. *Nat. Commun.* 2022;13(1):7340. https://doi.org/10.1038/s41467-022-35226-0